2007

Properties of Silica-Polypeptide Composite Particles

Jianhong Qiu
Louisiana State University and Agricultural and Mechanical College, jqiu1@lsu.edu

PROPERTIES OF SILICA-POLYPEPTIDE COMPOSITE PARTICLES

A Dissertation

Submitted to the Graduate Faculty of
Louisiana State University and
Agricultural and Mechanical College
in partial fulfillment of the
requirements for the degree of
Doctor of Philosophy
in
The Department of Chemistry

by
Jianhong Qiu
B.E., Tianjing University, 1994
M.S., Louisiana Tech University, 2002
August, 2007

ACKNOWLEDGEMENTS

First of all, I would like to thank Dr. Paul Russo, my major professor, for his guidance, support, and confidence on me throughout the project. I would never have finished my Ph.D. without his wide perspective and suggestions on many aspects of the research. I would also like to acknowledge Dr. Spivak, Dr. Garno, and Dr. Chen for their invaluable comments on the thesis and other presentations that I have given about my projects in the last few years. I should also thank Dr. Cueto for his expert help with characterization techniques and instruments. I can never forget to thank Dr. Russo's research group ─ Erick, Sibel, Amanda, Nadia, Derek, Jirun, and Garret. I couldn't have done my project without their help and support. Finally, I want to thank my husband, Yanlong Xu, who has been continuously encouraging me through the study even when he was thousands of miles away last year. This dissertation is for him.

TABLE OF CONTENTS

LIST OF TABLES

LIST OF FIGURES

LIST OF ABBREVIATIONS

AOM	Acousto-optic modulator
APS	3- Aminopropyltrimethoxy silane
CGS	Centimeter-gram-second
DA	Data acquisition
DCA	Dichloroacetic acid
DCE	Dichloroethylene
DFT	Density functional theory
DLS	Dynamic light scattering
DMF	*N, N'*-Dimethylformamide
DOSY	Diffusion-ordered spectroscopy
DSP	Digital signal processing
EM	Electron microscopy
EOM	Electro-optic modulator
FC	Field cooling
FCS	Fluorescence correlation spectroscopy
FITC	Fluorescein isothiocyanate
FRAP	Fluorescence recovery after photo bleaching
FPR	Fluorescence photobleaching recovery

FRS	Forced rayleigh scattering
GPC-LS	Gel permeation chromatography light scattering
HPC	Hydroxypropylcellulose
LB	Langmuir Blodgett
L-B-L	Layer-by-layer
LC	Liquid crystal
NCA	N-carboxy anhydrides
*o*FT	*o*-fluorotoluene
OR	Optical rotation
ORD	Optical rotation dispersion
PBLG	Poly (γ-benzyl-*L*-glutamate)
PCBL	Poly (ε-carbobenzoxy-*L*-lysine)
PDI	Polydispersity index
PEO	Polyethylene oxide
PFGNMR	Pulsed-field-gradient nuclear magnetic resonance
PLGA	Poly (*L*-glutamic acid)
PLL	Poly (*L*-lysine)
PM	Photosensor modules
PMT	Photomultiplier tube
PMVE	Poly(methyl vinyl ether)

PCS	Photon correlation spectroscopy
PS	Polystyrene
PSL	Polystyrene latex
QELSS	Quasi-elastic light scattering spectroscopy
RR	Ronchi ruling
SANS	Small angle neutron scattering
SiPCPs	Polypeptide-grated SiO_2 composite particles
SLS	Static light scattering
SPT	Scaled particle theory
TEM	Transmission electron microscopy
TEOS	Tetraethylorthosilicate
TFA	Trifluoro acetic acid
TGA	Thermogravimetric analysis
THF	Tetrahydrofuran
TMV	Tobacco mosaic virus
ZFC	Zero field cooling

ABSTRACT

Studies of grafting polymer on surfaces with chemical bonds started in the 1970's, but few projects have focused on grafting polypeptide on spherical particles. In this research, polypeptides poly(ε-carbobenzyloxy-*L*-lysine) (PCBL) or poly(γ-benzyl-*L*-glutamate) (PBLG) were grafted on silica sphere surfaces by using the "grafting from" method. The polypeptide-grafted silica spheres are called SiPCPs. The growth of polypeptide chains as a function of monomer amount and reaction time was explored. The properties of a mixture of PBLG rod-like polymer and PBLG SiPCPs were investigated. At high concentrations of these two components, the phase behavior was studied. At low concentrations of PBLG, the fluorescein isothiocyanate (FITC) labeled PBLG SiPCPs were used as probes to measure the probe diffusion through the PBLG matrix in pyridine. Because of the depletion-attraction effect, the mixture becomes very viscous even at low concentrations; consequently the diffusion of probe is very slow. A holographic fluorescence photobleaching recovery (FPR) instrument, which creates the grating from the interference of two crossed beams, was developed to satisfy such a specific condition. The polypeptides were grafted on silica spheres with a cobalt core inside, and Co-SiPCPs were formed. Preliminary results demonstrate that these particles can respond to an external magnetic field and the solvent can affect the magnetic behaviors of these particles.

CHAPTER 1 GENERAL INTRODUCTION

Uniform particles have been used in many applications such as probe diffusion,[1-6] fundamental colloid characterization,[7-10] surface modification,[9-14] and particle physical chemistry.[10-17] Functionalization of these particles by modifying the particle's surface[18-31] or the structure inside the particle[32] is a new challenge in polymer science. In this study, properties of polypeptide-grated SiO_2 composite particles (SiPCPs) such as polypeptide growth, probe diffusion, phase behavior, and Co-SiO_2-polypeptide magnetic particles are explored.

1.1 Introduction of Polypeptides

A polypeptide is a chain of amino acids that contains carboxyl and amino groups. In figure 1.1, "R" presents the alkyl chain attached at the α-carbon position. About 20 common amino acids are found in natural polypeptide.

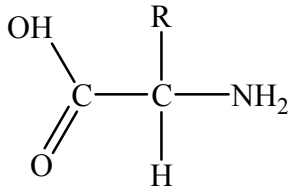

Figure 1.1 Structure of an amino acid.

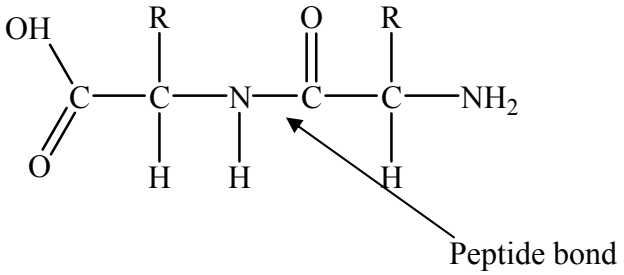

Figure 1.2 Scheme of polypeptide bond.

Amino acids are joined together through a peptide bond (Figure 1.2) to form a polypeptide or protein. Pauling and Corey studied the geometrical and dimensional information, including the interatomic distance, bond angle, and other parameters of a polypeptide chain by analyzing the crystal structure of amino acid, peptide, and other protein-related materials.[33] Figure 1.3 gives the dimensions of a polypeptide chain and shows interatomic distance and bond angles. It is assumed that all hydrogen bonds in a single polypeptide chain have the same length; the asymmetric amino acid residue can rotate 180^{o} along an axis, and the two opposite directions are equally favored.[33]

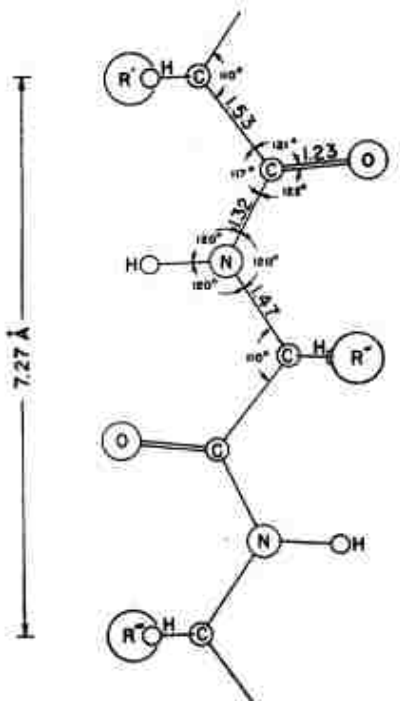

Figure 1.3 Dimension of polypeptide chain. (Copied from Ref. 33)

Pauling, *et al.,* believed that the four atoms of the group H-N-C=O are on one plane called the peptide plane, and the rotation of the plane may cause instability. The N-C peptide bond (1.32Å) is shorter than the normal N-bond (1.47 Å) because it has 50% of the character of a double bond.

1.1.1 Polypeptide Secondary Structures

Ungrafted (free) polypeptides have three basic common secondary structures: α helix, β sheet, and random coil. The three common secondary structures are given in Figure 1.4. There are several other structures including γ-helix, π-helices, ω-helices, β-turns, loops, etc.

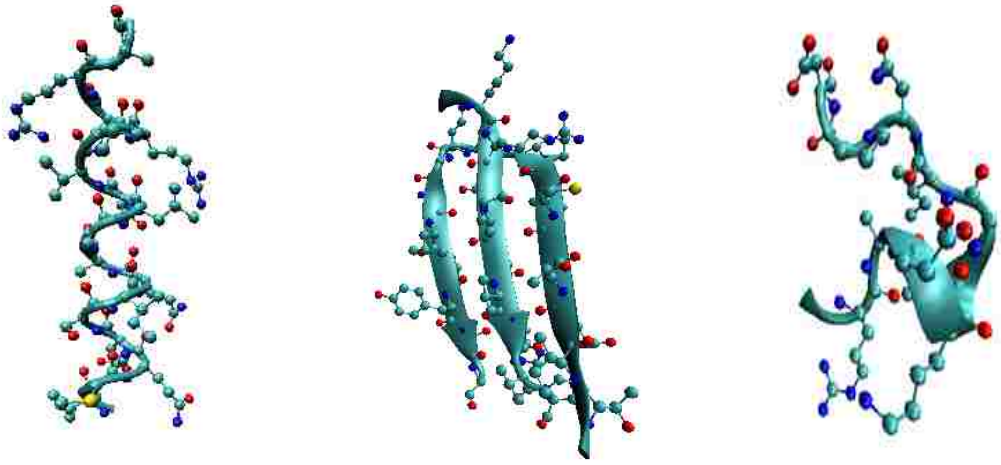

α helix β sheet random coil

Figure 1.4 Three common secondary structures of polypeptide. (The structures were generated with VMD software and PDB 1RR9)

Corey's group confirmed that the γ- and α- helices are the only two helical conformations that are stereochemically stable. The helical structure comes from hydrogen bonding: N—H•••O=C, and their structures have been described in detail.[33] Figures 1.5a and 1.5b are the figures of two helices configuration of the polypeptide chain.

The number of residues per turn is not necessarily integral.[33] The γ- helix has a 5.1-residue/ turn. The rise (per residue) changes slightly with the varied distance of N-H•••O bond. If the distance of N-H•••O is 2.72Å, the rise per residue is 0.97Å; if the distance is 2.78Å, the rise increases to 0.98Å, while for α-helix, the hydrogen bond distance is 2.75Å, and the rise/turn is

1.47Å. Poly-γ-methyl-*L*-glutamate and poly-γ-benzyl-*L*-glutamate are two typical synthetic helical polypeptides.[33-35]

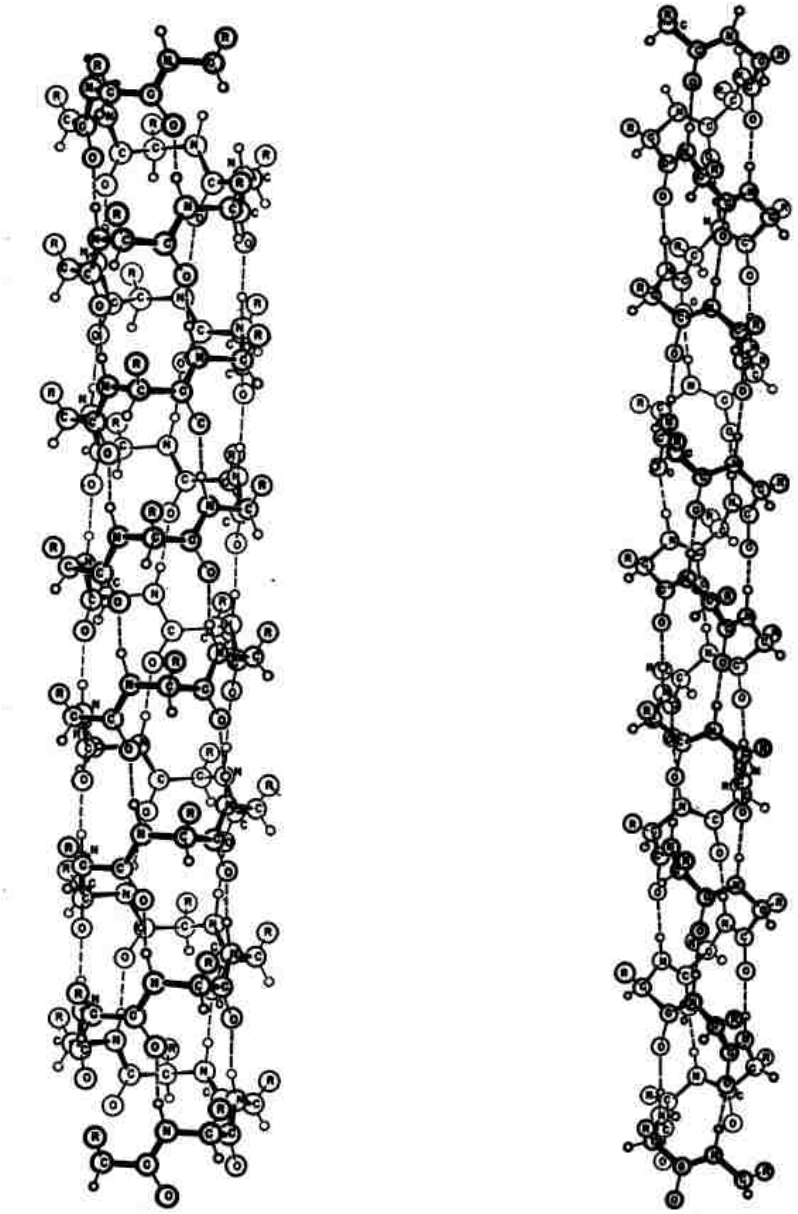

a b

Figure 1.5 The two helical structures of polypeptide. a): The helix with 5.1 residues per turn; b): The helix with 3.7 residues per turn. (Both copied from Ref. 33)

1.1.2 Poly-γ-benzyl-*L*-glutamate and Poly (ε-carbobenzoxy-*L*-lysine)

Figure 1.6 is the structure of poly (α-amino acids). Two polypeptides Poly (γ-benzyl-L-glutamate) (PBLG) and Poly (ε-carbobenzoxy-*L*-lysine) (PCBL) are studied in this dissertation.

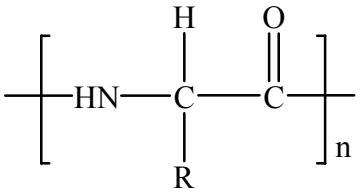

For PBLG: R= $CH_2CH_2CO_2CH_2C_6H_5$; For PCBL: R= $(CH_2)_4NHCO_2CH_2C_6H_5$

Figure 1.6 General structure of poly (α-amino acids).

Introduced by Leuchs in 1906,[36] synthetic polyglutamates can be synthesized by ring-opening polymerization using *N*-carboxy anhydrides (NCA) as monomer. Figure 1.7 gives the general structure of NCA.

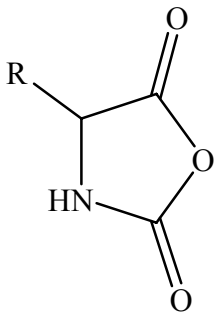

For BLG-NCA: R= $CH_2CH_2CO_2CH_2C_6H_5$ For CBL-NCA: R= $(CH_2)_4NHCO_2CH_2C_6H_5$

Figure 1.7 General structure of amino acid NCA.

Phosgene gas[37] or phosgene derivatives[38,39] have been used to synthesize NCA; however, the byproduct HCl may lead to side reactions. In 1998, Daly, *et al*,[40] reported a triphosgene substitute for phosgene. Since triphosgene provides a triple equivalent of phosgene *in situ*, less HCl is produced, decreasing side reactions. Several mechanisms were reported for "amine-initiated"

polymerization of NCA, such as the "amine mechanism" (also called the "protic mechanism" [Figure 1.8]). It was first reported by Wessely[41] and Waston, [42] and the process is as follows: 1) primary amine (1) attacks C-5 NCA monomer (2) and opens the ring; 2) carbon dioxide is eliminated from the intermediate (3) and the new attacking molecules with primary amine end group (4) is formed; 3) the intermediate (4) reacts with another NCA monomer for further polymerization. The reaction has a living character since highly nucleophilic alkylamine (including *n*- butylamine and *n*- hexylamine) initiates the reaction much faster than the chain-end amine group, consequently, the initiation is faster than propagation. Unfortunately, it is difficult to get a high molecular weight by using this type of initiator because of the termination reaction, such as cyclization of chain ends.[43]

Another mechanism called the "carbamate mechanism" (Figure 1.9) was reported by Idelson and Blout.[44] The first step is the same as in the amine mechanism: the primary amine (1) attacks the NCA monomer (2), then the intermediate (3) is formed. In the next steps, the primary amine is strong enough to deprotonate the intermediate carbamic acid (3) and the intermediate (3') is formed; then 3' reacts with the NCA monomer (2) to produce intermediate anhydride 6. A new polypeptide bond is formed and the polymerization proceeds after decarboxylation.

In 1956, Blout and Carslon polymerized high molecular weight PBLG by using BLG-NCA as the monomer and tertiary amine as the initiator.[44] In 1961, Bamford[45] first reported the "activated monomer mechanism" which used strongly basic amine, e.g., the tertiary amine, in Blout's experiment as an initiator. The "activated monomer mechanism" is described in Figure 1.8. The strongly basic amine (1), here it is tertiary amine, deprotonates the NCA monomer (2) and the "activated monomer" 2' is formed. Then 2'attacks another NCA monomer to form intermediate 8. There are 3 possibilities for intermediate 8 to continue the polymerization. 1)

Reacts with NCA monomer. 2) Forms intermediate 9 after decarboxylation and protonation, and then intermediate (9) reacts with monomer. 3) Intermediate (9) reacts with electrophilic N-acyl-NCA (2'). The three opportunities result in a broad molecular-weigh-distribution polypeptide product.

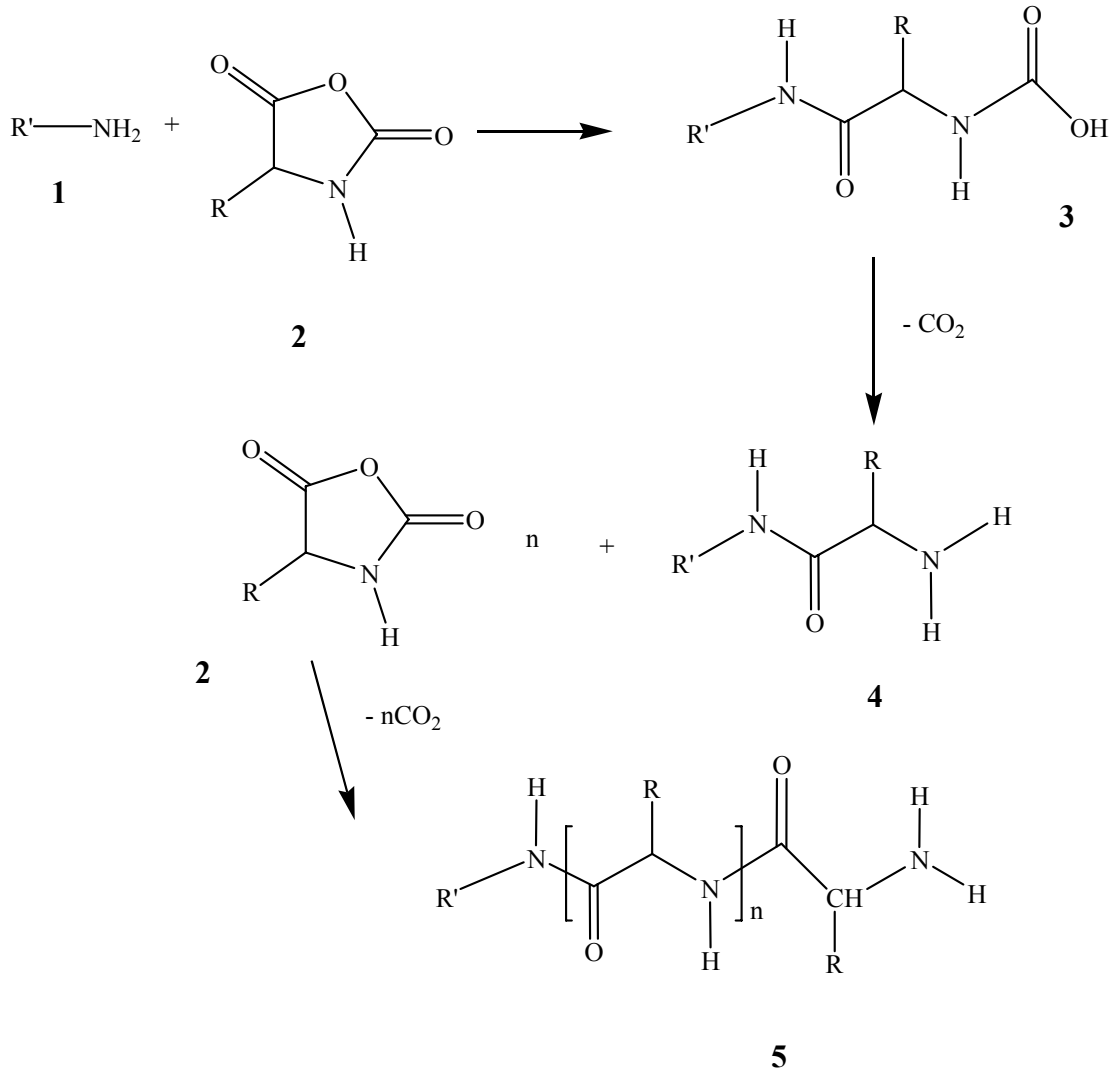

Figure 1.8 The "amine mechanism".

Besides amines, the ring-opening polymerization of NCA can be initiated by water molecules,[46,47] metal salts [46], and transition metal-amine complexes such as the nickel complex introduced by Deming's group.[48-54]

PBLG is the most frequently studied polypeptide.[55] It has a rigid rod-like α-helix conformation[33-56] which is stable up to 160 ^{o}C and the helical structure can only be disturbed by strong acids such as trifluoro acetic acid (TFA) and dichloroethylene (DCA). PBLG can be dissolved in several solvents, including chloroform, DCA, tetrahydrofuran (THF), formamide, and some mixed solvent, but only pyridine, *N*,*N*-dimethyl formamide (DMF), nitrobenzene, benzyl alcohol, and *m*-cresol can dissolve PBLG without causing aggregation.[57]

PBLG has well-defined chain conformation in solution.[55] In contrast, most common synthetic polymers lose their long-range order in solution. PBLG can change its conformation from α-helix to random coil corresponding to the change of the environmental conditions;[18-22,58-65] thus, the macromolecular properties of ordered, disordered, and intermediate states can be investigated at the same time.[66]

PCBL was first synthesized by Blout, *et al.,* in the late 1950's by using CBL-NCA as monomer. The degree of polymerization was reported to be over 5000.[67] The polymerizations were initiated by sodium methoxide in the solvent dioxane.[67,68] The optical rotatory dispersion and infrared studies indicated that PCBL has a helical conformation in $CHCl_3$ and DMF; the helix-to-coil transition happens in mixed solvents which have a strong hydrogen bonding component such as DCA. In DCA/CH_2Cl_2 mixture, the helix-coil transition occurs at about 35% DCA in CH_2Cl_2 at about 25 °C, and the transition temperature increases with increased concentration of DCA.[60] The helix-coil transition also occurs in a DCA/DCE mixture.[69] Besides the solvent used, temperature is another factor that can transfer PCBL from helix → coil or *vice versa*. Heat capacity, optical rotation, and dielectric dispersion measurements all show that the sharp inverse transition of PCBL occurs around 30 ^{o}C in *m*-cresol [70,71,72] regardless of the molecular weight and concentration.[72]

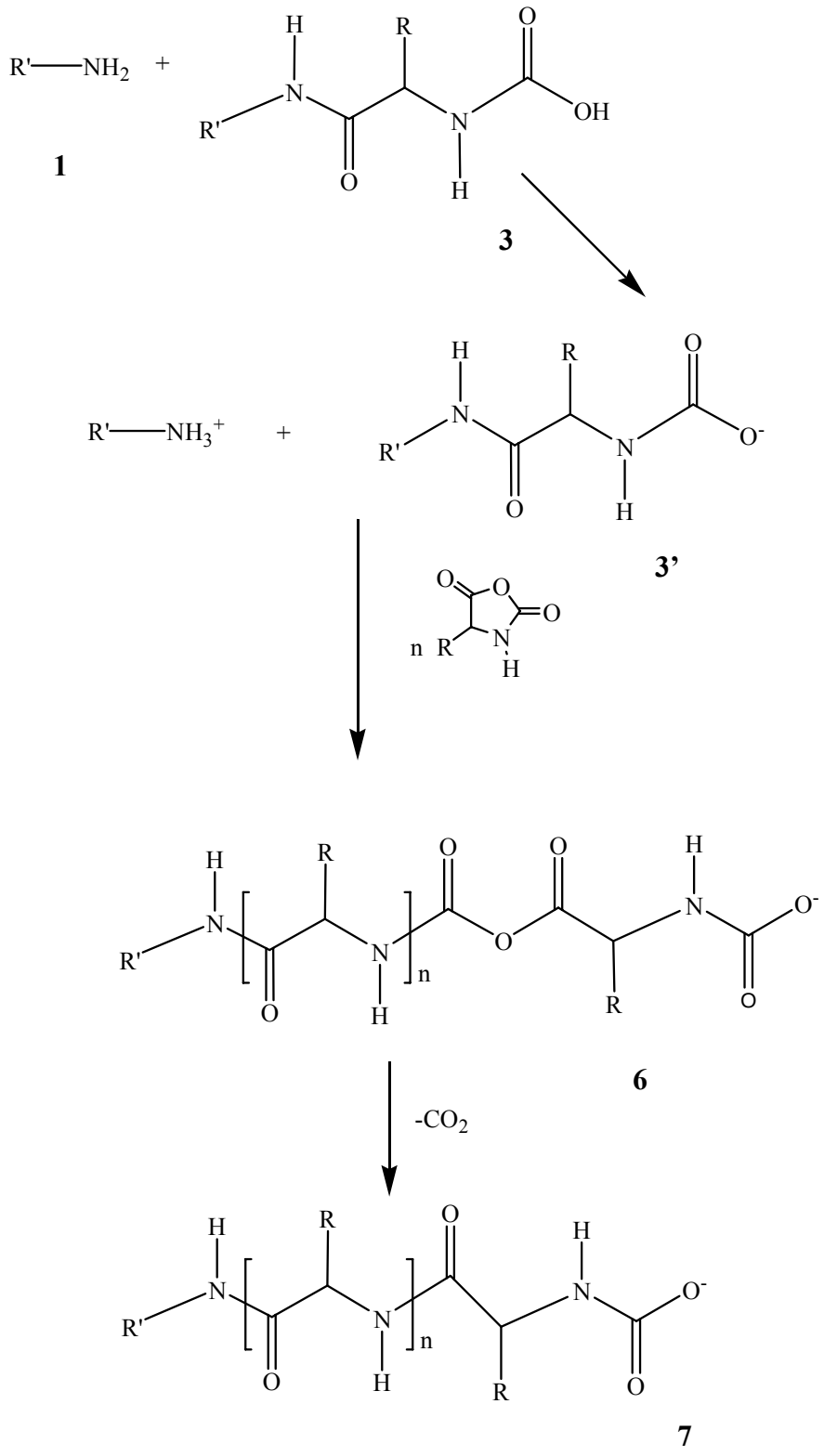

Figure 1.9 The “carbamate mechanism”.

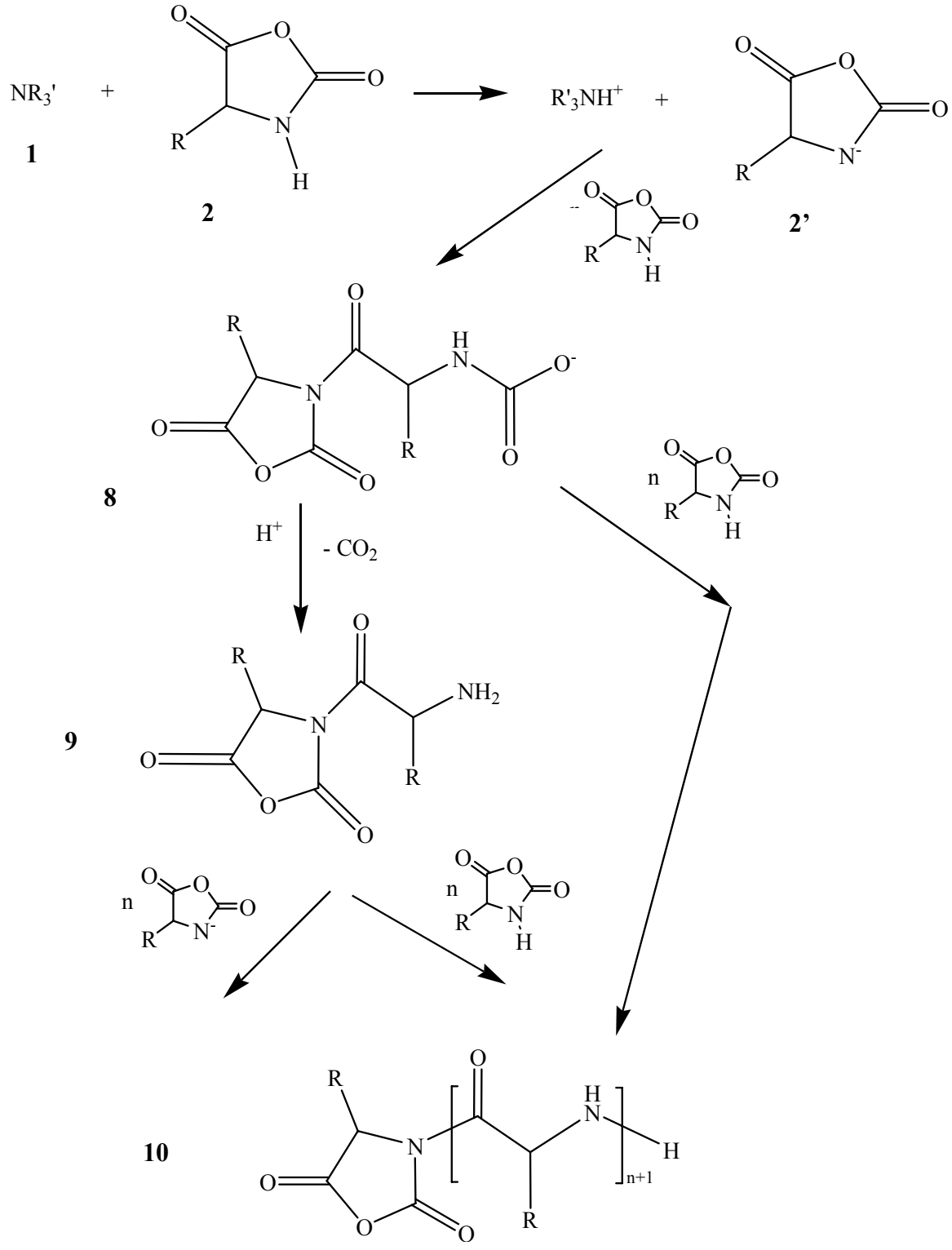

Figure 1.10 The “activated monomer mechanism”.

The transition of helix → coil may induce a size change. In dilute solution, one can trace the transition by using light scattering, which is discussed in detail in a later section. In a concentrated sample, observation of the crystal/amorphous structure by using cross-polarized optical microscopy is a simple and visual method to check the helix → coil transition of PBLG and PCBL.[66] The experimental results of the helix-coil transition of PCBL in *m*-cresol are presented in section 3.3.

1.2 Surface Grafting of Polymer

Polymer thin films can be deposited on substrates such as SiO_2 wafers or glass slides by spin-coating,[73] solvent casting,[74] the Langmuir Blodgett (LB) method [75-79], or the layer-by-layer (L-B-L) self-assembly technique.[80,81] Surface-pressure-driven LB film and a static-attraction driven L-B-L assembly also provide the opportunity to make multilayer structures. Polymer molecules are absorbed and they stay on the surface "physically". This means there is no chemical bond involved, and the film can be taken off by mechanical force. Figures 1.11 and 1.12 are the schematic representation of the procedure of LB deposition and L-B-L assembly. In the LB procedure, the monolayer of polymer dispersed on the surface of the liquid is transferred to the solid substrate by immersing and emerging the substrate in the liquid (detail is in Figure 1.11).[82] The polymer normally has a hydrophilic group at one end and a hydrophobic group at the other end. The multilayer structure can be built on the substrate by simply repeating the "immersing and emerging" steps.

Unlike the LB process, for the L-B-L process the charged solid support is sequentially immersed in a solution that contains a polyelectrolyte with the *opposite* charge of the support; and then in a solution that contains a polyelectrolyte with the *same* charge as the support after it is

rinsed briefly. By repeating these steps, alternating polyion assemblies can be obtained with reproducible layer thicknesses.

Grafting polypeptides on solid surfaces with a chemical bond began in the early 1970's. Hamann, *et al.,* reported grafting co-polypeptide from an SiO_2 surface functionalized with an aminophenyl group [figure 1.11a] in 1974.[83] One year later, the same group successfully grafted homopolymer (polystyrene and poly [vinylpyridine]) on an SiO_2 surface modified with [(mercaptonaphthyl)azo]phenyl groups.[84] Figure 1.13 "a" and "b" give the chemical structures of these two SiO_2 modifying groups

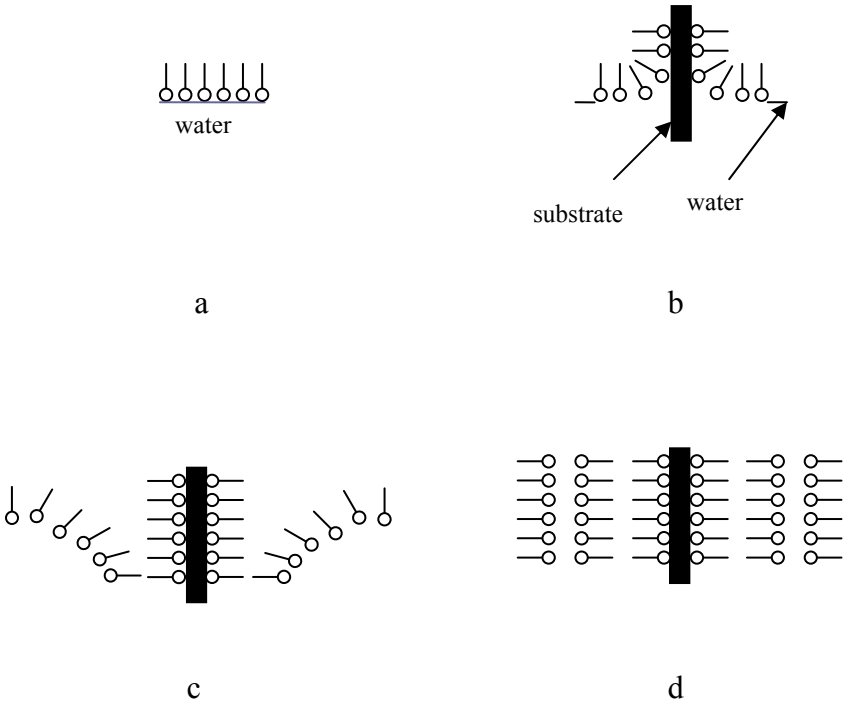

Figure 1.11 Langmuir-Blodgett film depositions (Y-type) on a hydrophilic substrate. a) monolayer on the surface of water; b) first layer deposited on the substrate; c)second layer on the substrate; d) third layer on the substrate (Adapted from Ref.79)

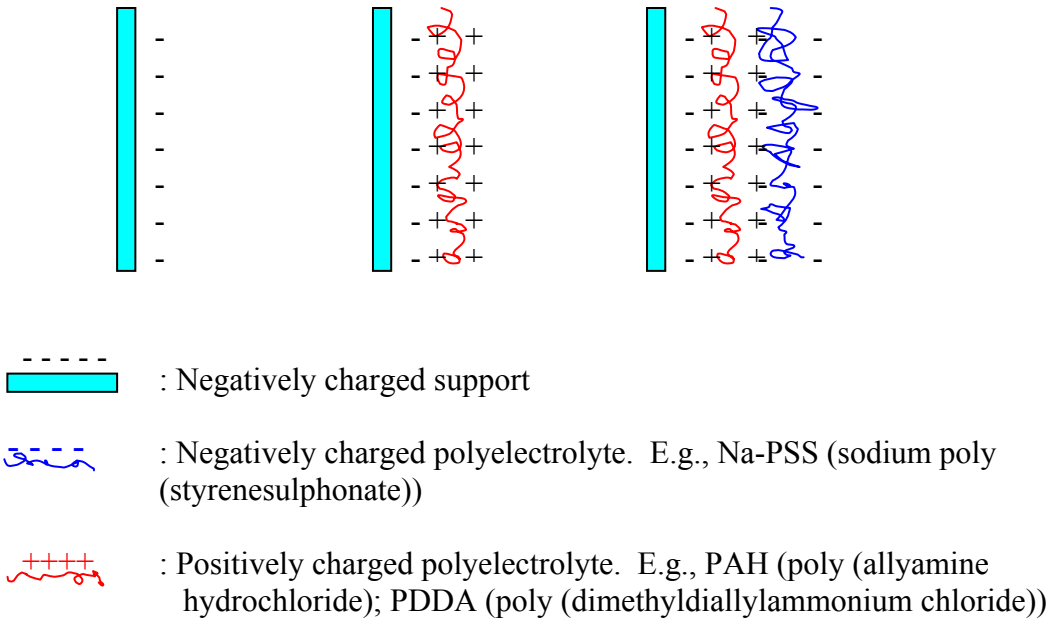

Figure 1.12 Procedure of L-B-L assembly. (Adapted from Ref.81)

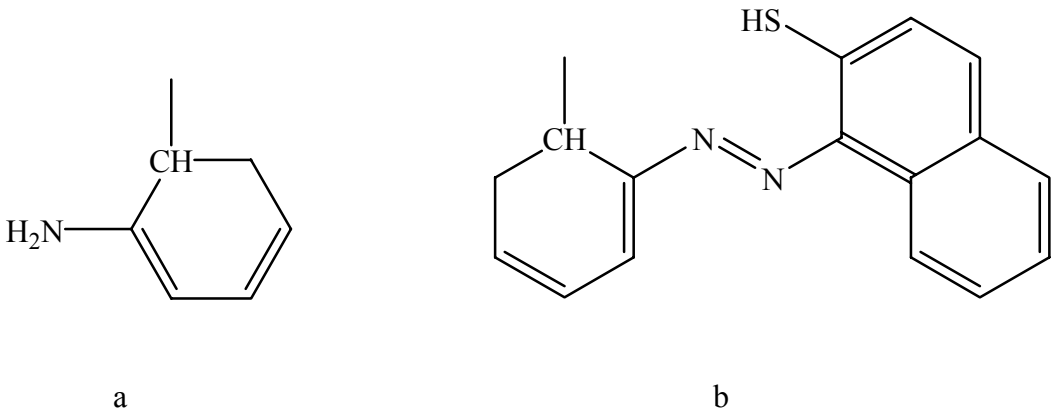

Figure 1.13 Two SiO_2 modifying groups. a): Chemical structure of aminophenyl group; b): Chemical structure of [(mercaptonaphthyl)azo]phenyl group

In 1996, Wieringa, *et al*.[85], introduced a new solvent-free method to generate poly (methyl-L-glutamate) layers on silicon wafers by spin-coating the monomer NCA, which was dissolved in THF, on a wafer followed by evaporation of solvent and polymerization in the melt. In 1998, Chang and Frank[86] applied a chemical-vapor-deposition technique to graft homo-polypeptide on silicon wafer. Later, Wang and Chang improved this method to graft co-polypeptides on silicon oxide surfaces.[87,88] Besides many grafting experiments carried out on flat surfaces,[89-94] there are also many reports of random coil polymers such as polystyrene,[95] poly (methylmethacrylate)[96] or poly (ethyleneoxide)[97] covalently or noncovalently attached to particle surfaces. However, not much research focuses on grafting polypeptide to spherical particles.

Grafting methods can be grouped into two categories: "grafting onto" (Figure 1.14a) and "growing from" (Figure 1.14b). In the "grafting onto" method, polymer chains are attached to a surface through their N- or C- terminals that can react with surface functional groups. In the "grawing from" method, polymer chains "grow up" from the surface, which means that the polymerization is initiated by surface-attached species and proceeds on the surface. Both methods have advantages and disadvantages. For the "grafting onto" method, the molecular weight and the dispersity of the attached polymer can be controlled and measured before the polymer is affixed to the surface. Conformation of the resulting polypeptide film is easily controlled because it is determined only by the conformation of the original polypeptide and the surface-denatured states. Aggregation and steric hindrance are two big problems. Poor solubility of synthetic polypeptides in typical organic solvents worsens the aggregation; at the same time, steric hindrance gets more serious when surface density increases. Moreover, the rod-like polymer may destabilize the silica dispersion before the coating reaction occurs. "Growing from" overcomes some of the disadvantages of the "grafting onto" method, but in most cases, it is

impossible to characterize the polymer directly since the polymer is synthesized from the surface. In addition, strict polymerization conditions such as dry solvent need to be considered. Figure 1.12 describes the two methods.

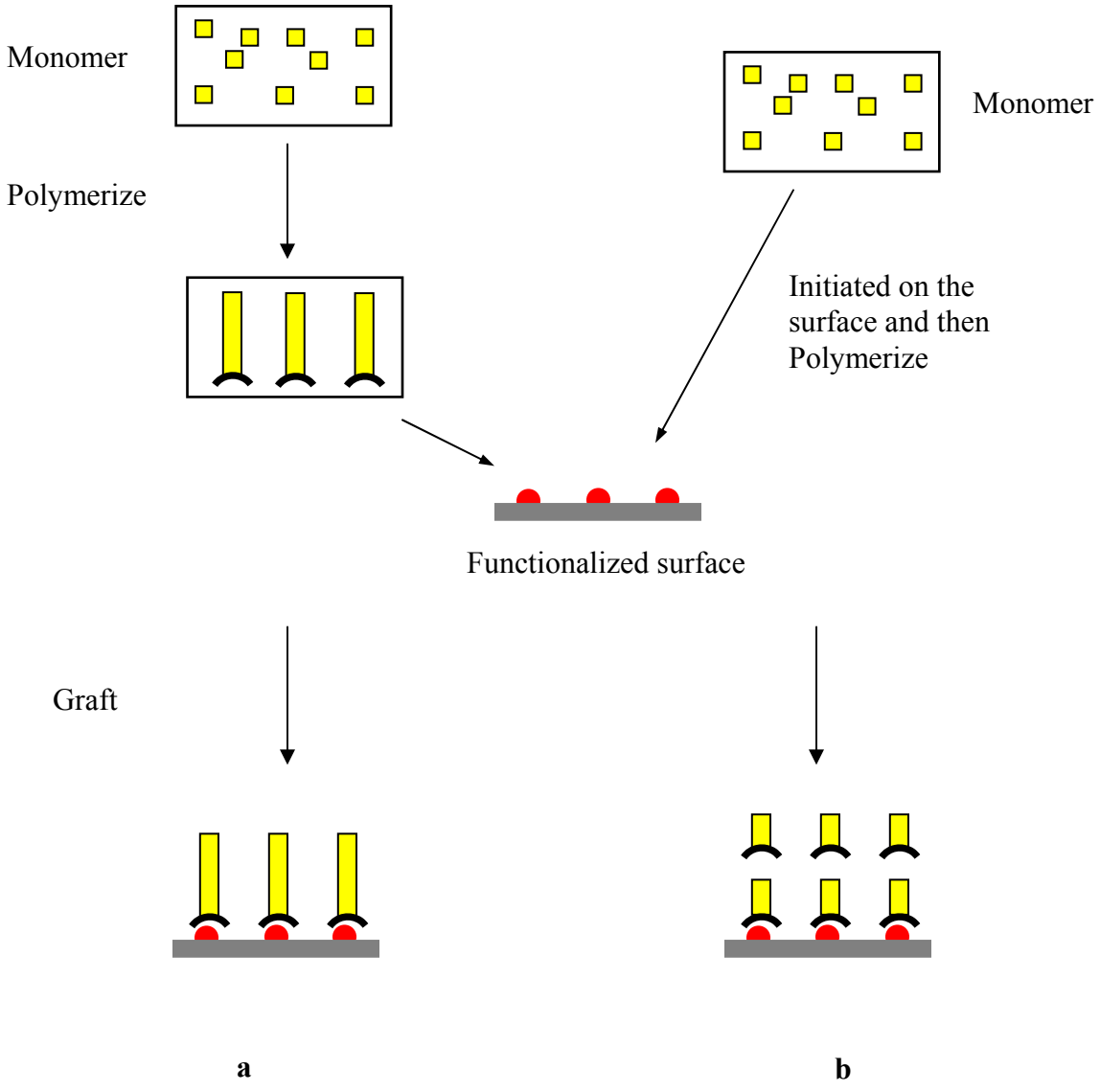

Figure 1.14 Scheme of two surface grafting methods. a): "grafting onto" method; b): "growing from" method

Grafted polymer chains may have different conformations and abilities to change the conformation due to motion constraint. For PBLG and its family protein members, Chang, *et al*., claim that "grafting onto" and "growing from" may create grafted PBLG with different conformations.[98] "Grafting onto" typically forms β sheet and α helix structures but it might depend on modification of the substrates. "Growing from" normally produces random coil structures. Moreover, all these variations come from intermolecular interaction and the interaction between polypeptides and substrates. Water-soluble polypeptides, poly (L-lysine) (PLL)[99] and poly (L-glutamic acid) (PLGA),[100] which are debenzylated from PCBL and PBLG, respectively, can change conformation by changing the concentration of salt(s) , surfactant, or pH of environments. The orientation of helical PBLG can be aligned by the "solvent quenching" treatment[101,102] where polymer chains can get "relaxed" and are stretched out in a good solvent. Meanwhile, the unidirectional structures are frozen by a bad solvent. Good and bad solvent pairs can be chloroform/acetone, DMF/water, tetrahydrofuran/hexane, or dioxane/methanol whenever the solvent pair is miscible.

1.3 Dissertation Overview

The overall aim of this study is to synthesize and characterize the SiPCPs (much of the synthesis work was done by Erick Soto-Cantu). There are several reasons why SiO_2 particles are chosen as the grafted substrate. First, silica particles can be made with variable sizes and they cost less than silver[103] or gold[104] particles. Moreover, they are easily functionalized and can be dissolved by HF[105] to yield polypeptide hollow shells, assuming the shell material can be cross linked. The radii of the SiO_2 particles are around 20-100 nm and the "growing from" method was chosen to produce SiPCPs in order to minimize the steric hindrance problem and the potential instability in mixtures of rod-like polypeptide and spherical particles.

In this dissertation, at first the "living polymerization" character is explored, and this method is used to graft copolymer on the SiO_2 surface. Secondly, the physical properties of mixtures of polypeptide and SiPCPs at low and high concentrations are studied. Then the construction of the holographic Fluorescence Photobleaching Recovery (FPR) used to measure extremely low diffusion coefficients is discussed. Finally, the effects of the polymer shell on Co-SiO_2 nanoparticles' magnetic behavior are discussed.

Chapter 2 describes the synthesis of SiPCPs with the method of reacting an NCA monomer with a 3-aminopropyltrimethoxy silane (APS)-functionalized SiO_2 sphere surface. The living feature of the polymerization is measured using dynamic light scattering and static light scattering. With the same approach of grafting homopolypeptide, block-copolymer PBLG/ PCBL is able to grow on the spherical surface.

The stability of mixtures of rod-like polymers and SiPCPs is investigated. In **Chapter 3**, dilute and concentrated mixtures are studied. At low concentrations, probe diffusion of SiPCP is measured by using a fluorescence photo-bleaching recovery (FPR) and dynamic light scattering (DLS); at high concentrations the phase separation is visualized by using polarized microscopy.

In order to measure an extremely low diffusion coefficient of a fluorescence-labeled probe, a narrower optical grating is necessary. The construction of the holographic FPR instrument, in which the grating space can be as narrow as the wavelength of the incident laser beam, is illustrated in **Chapter 4**.

In **Chapter 5**, some preliminary results of the magnetic SiPCPs are presented. The magnetic SiPCPs have nano-sized cobalt cores, and it shows superparamagnetism. The polymer shell has an effect on the particles' alignment and disassociation.

1.4 References

(1) Gold, D.; Onyenemezu, C.; Miller, W. G. Effect of Solvent Quality on the Diffusion of Polystyrene Latex Spheres in Solutions of Poly(Methyl Methacrylate). *Macromolecules* **1996,** *29,* 5700-5709.

(2) Won, J.; Onyenemezu, C.; Miller, W. G.; Lodge, T. P. Diffusion of Spheres in Entangled Polymer Solutions: A Return to Stokes-Einstein Behavior. *Macromolecules* **1994,** *27,* 7389-7396.

(3) Levitz, P. E. Interplay Between Slow Interfacial Water Diffusion and Colloid Dynamics: A Way to Probe Colloidal Transitions. *Materials Research Society Symposium Proceedings* **2004,** *790,* 101-106.

(4) van der Gucht, J.; Besseling, N. A. M.; Knoben, W.; Bouteiller, L.; Cohen Stuart, M. A. Brownian Particles in Supramolecular Polymer Solutions. *Physical Review E: Statistical, Nonlinear, and Soft Matter Physics* **2003,** *67,* 051106-1-051106/10.

(5) Richtering, W.; Mueller, H. Comparison between Viscosity and Diffusion in Monodisperse and Bimodal Colloidal Suspensions. *Langmuir* **1995,** *11,* 3699-3704.

(6) Richtering, W.; Berend, K. Dynamics of Monodisperse and Bidisperse Polymer Latexes. *Progress in Colloid & Polymer Science* **1995,** *98,* 79-84.

(7) Chang, C. L.; Fogler, H. S. Controlled Formation of Silica Particles From Tetraethyl Orthosilicate in Nonionic Water-in-Oil Microemulsions. *Langmuir* **1997,** *13,* 3295-3307.

(8) Boukari, H.; Long, G. G.; Harris, M. T. Polydispersity during the Formation and Growth of the Stober Silica Particles from Small-Angle X-Ray Scattering Measurements. *Journal of Colloid and Interface Science* **2000,** *229,* 129-139.

(9) Thies-Weesie, D. M. E.; Philipse, A. P.; Lekkerkerker, H. N. W. Sedimentation of Bidisperse, Uncharged Colloidal Sphere Suspensions: Influence of Viscosity and Irregular Surfaces. *Journal of Colloid and Interface Science* **1996,** *177,* 427-438.

(10) Thies-Weesie, D. M. E.; Philipse, A. P.; Nagele, G.; Mandl, B.; Klein, R. Nonanalytical Concentration Dependence of Sedimentation of Charged Silica Spheres in an Organic Solvent: Experiments and Calculations. *Journal of Colloid and Interface Science* **1995,** *176,* 43-54.

(11) Bansmann, J.; Baker, S. H.; Binns, C.; Blackman, J. A.; Bucher, J. P.; Dorantes-Davila, J.; Dupuis, V.; Favre, L.; Kechrakos, D.; Kleibert, A.; Meiwes-Broer, K. H.; Pastor, G. M.; Perez, A.; Toulemonde, O.; Trohidou, K. N.; Tuaillon, J.; Xie, Y. Magnetic and

Structural Properties of Isolated and Assembled Clusters. *Surface Science Reports* **2005,** *56,* 189-275.

(12) Patel, A.; Kommireddy, D.; Shutava, T.; Lvov, Y. Nano-Organized Thin Films for Surface Modifications. *Abstracts, 60th Southwest Regional Meeting of the American Chemical Society, Fort Worth, TX, United States, September 29-October 4* **2004,** SEPT04-193.

(13) Fuerbeth, W.; Nguyen, H. Q.; Schuetze, M. Small Causes with Large Effect. New Corrosion Protection Layers for Metals Based on Chemical Nanotechnology. *Metalloberflaeche* **2004,** *58,* 31-36.

(14) Arunagiri, T.; Gao, J. S.; Chen, J. J.; Goodwill, P.; Chyan, O. Deposition of Metal Nanoparticles on Diamond Surface Via a Solution Route. *Proceedings - Electrochemical Society* **2004,** *2000-34,* 26-37.

(15) Donselaar, L. N.; Philipse, A. P. Interactions between Silica Colloids With Magnetite Cores: Diffusion, Sedimentation and Light Scattering. *Journal of Colloid and Interface Science* **1999,** *212,* 14-23.

(16) Fuchs, A.; Killmann, E. Adsorption of Polyelectrolytes on Colloidal Latex Particles, Electrostatic Interactions and Stability Behaviour. *Colloid and Polymer Science* **2001,** *279,* 53-60.

(17) Limary, R.; Swinnea, S.; Green, P. F. Stability of Diblock Copolymer/Layered Silicate Nanocomposite Thin Films. *Macromolecules* **2000,** *33,* 5227-5234.

(18) Patton, D.; Locklin, J.; Meredith, M.; Xin, Y.; Advincula, R. Nanocomposite Hydrogen-Bonded Multilayer Ultrathin Films by Simultaneous Sexithiophene and Au Nanoparticle Formation. *Chemistry of Materials* **2004,** *16,* 5063-5070.

(19) Turney, K.; Drake, T. J.; Smith, J. E.; Tan, W.; Harrison, W. W. Functionalized Nanoparticles for Liquid Atmospheric Pressure Matrix-Assisted Laser Desorption/Ionization Peptide Analysis. *Rapid Communications in Mass Spectrometry* **2004,** *18,* 2367-2374.

(20) Pastoriza-Santos, I.; Gomez, D.; Perez-Juste, J.; Liz-Marzan, L. M.; Mulvaney, P. Optical Properties of Metal Nanoparticle Coated Silica Spheres: a Simple Effective Medium Approach. *Physical Chemistry Chemical Physics* **2004,** *6,* 5056-5060.

(21) Shi, W.; Sahoo, Y.; Swihart, M. T. Gold Nanoparticles Surface-Terminated With Bifunctional Ligands. *Colloids and Surfaces, A: Physicochemical and Engineering Aspects* **2004,** *246,* 109-113.

(22) Schiestel, T.; Brunner, H.; Tovar, G. E. M. Controlled Surface Functionalization of Silica Nanospheres by Covalent Conjugation Reactions and Preparation of High

Density Streptavidin Nanoparticles. *Journal of Nanoscience and Nanotechnology* **2004,** *4,* 504-511.

(23) Guo, D. j.; Li, H. l. Electrochemical Synthesis of Pd Nanoparticles on Functional MWNT Surfaces. *Electrochemistry Communications* **2004,** *6,* 999-1003.

(24) Schneider, G.; Decher, G. From Functional Core/Shell Nanoparticles Prepared Via Layer-by-Layer Deposition to Empty Nanospheres. *Nano Letters* **2004,** *4,* 1833-1839.

(25) Deng, F.; Yang, Y.; Hwang, S.; Shon, Y. S.; Chen, S. Fullerene-Functionalized Gold Nanoparticles: Electrochemical and Spectroscopic Properties. *Analytical Chemistry* **2004,** *76,* 6102-6107.

(26) Nitin, N.; LaConte, L. E. W.; Zurkiya, O.; Hu, X.; Bao, G. Functionalization and Peptide-Based Delivery of Magnetic Nanoparticles As an Intracellular MRI Contrast Agent. *JBIC, Journal of Biological Inorganic Chemistry* **2004,** *9,* 706-712.

(27) Ko, S.; Bae, J.; Jang, J. Synthesis of Poly(Glycidyl Methacrylate) Nanoparticles Using Microemulsion Polymerization. *Polymeric Materials: Science and Engineering* **2004,** *91,* 558-559.

(28) Zhang, M. Synthesis of Magnetic Nanoparticles with Polymer Coatings. *Abstracts of Papers, 228th ACS National Meeting, Philadelphia, PA, United States, August 22-26, 2004* **2004,** INOR-177.

(29) Knoll, W.; Han, M. Y.; Li, X.; Hernandez-Lopez, J. L.; Manna, A.; Muellen, K.; Nakamura, F.; Niu, L.; Robelek, R.; Schmid, E. L.; Tamada, K.; Zhong, X. Nanoscopic Building Blocks From Polymers, Metals, and Semiconductors for Hydrbid Architectures. *Journal of Nonlinear Optical Physics & Materials* **2004,** *13,* 229-241.

(30) Shim, S. E.; Lee, H.; Choe, S. Synthesis of Functionalized Monodisperse Poly(Methyl Methacrylate) Nanoparticles by a RAFT Agent Carrying Carboxyl End Group. *Macromolecules* **2004,** *37,* 5565-5571.

(31) Katz, E.; Shipway, A. N.; Willner, I. Chemically Functionalized Metal Nanoparticles: Synthesis, Properties and Applications. *Nanoscale Materials* **2003,** 5-78.

(32) Yin, Y.; Lu, Y.; Gates, B.; Xia, Y. Synthesis and Characterization of Mesoscopic Hollow Spheres of Ceramic Materials With Functionalized Interior Surfaces. *Chemistry of Materials* **2001,** *13,* 1146-1148.

(33) Pauling, L.; Corey, R. B.; Branson, H. R. The Structure of Proteins: Two Hydrogen-Bonded Helical Configurations of the Polypeptide Chain. *Proceedings of the National Academy of Sciences of the United States of America* **1951,** *37,* 205-211.

(34) Pauling, L.; Corey, R. B. Two Hydrogen-Bonded Spiral Configurations of the Polypeptide Chain. *Journal of the American Chemical Society* **1950,** *72,* 5349.

(35) Pauling, L.; Corey, R. B. Structure of Synthetic Polypeptides. *Proceedings of the National Academy of Sciences of the United States of America* **1951,** *37,* 241-250.

(36) Leuchs, H. Glycinecarboxylic Acid. *Berichte der Deutschen Chemischen Gesellschaft* **1906,** *39,* 857-861.

(37) Fuller, W. D.; Verlander, M. S.; Goodman, M. A Procedure for the Facile Synthesis of Amino-Acid N-Carboxy Anhydrides. *Biopolymers* **1976,** *15,* 1869-1871.

(38) Oya, M.; Katakai, R.; Nakai, H.; Iwakura, Y. Novel Synthesis of N-Carboxy-α-Amino Acid Anhydride. *Chemistry Letters* **1973,** 1143-1144.

(39) Katakai, R.; Iizuka, Y. Characterization of L-Methionine in a Peptide a-Helix by Far-Infrared Spectroscopy. Synthesis and Examination of Sequential Polypeptides Containing L-Methionine. *Journal of the Chemical Society, Perkin Transactions 1: Organic and Bio-Organic Chemistry (1972-1999)* **1984,** 2665-2668.

(40) Daly, W. H.; Poche, D. The Preparation of *N*-Carboxyanhydrides of α-Amino Acids Using Bis(Trichloromethyl) Carbonate. *Tetrahedron Letters* **1988,** *29,* 5859-5862.

(41) Wesseley, F. α-Amino-*N*-Carboxylic Acid Anhydrides. I. *Z. physiol. Chem.* **1925,** *146,* 72-90.

(42) Waley, S. G.; Watson, J. The Kinetics of the Polymerization of Sarcosine Carbonic Anhydride. *Proc. Roy Soc. (London)* **1949,** *A199,* 499-517.

(43) Penczek, S.; Kricheldorf, H. R. Models of Biopolymers by Ring-Opening Polymerization. Boca Raton, Fla. : CRC Press : 1990.

(44) Idelson, M.; Blout, E. R. Polypeptides. XVIII. A Kinetic Study of the Polymerization of Amino Acid N-Carboxyanhydrides Initiated by Strong Bases. *Journal of the American Chemical Society* **1958,** *80,* 2387-2393.

(45) Bamford, C. H.; Block, H. The Initiation Step in the Polymerization of N-Carboxy-α-Amino Acid Anhydrides. I. Catalysis by Tertiary Bases. *Journal of the Chemical Society* **1961,** 4989-4991.

(46) Kricheldorf, H. R. α-Amino Acid *N*-Carboxy Anhydrides and Related Heterocycles: Syntheses, Properties, Peptide Synthesis, Polymerization; 1987; pp 213.

(47) Block, H.; Jackson, J. B. Calorimetric Detection of Conformational Changes in Polypeptides. *Proc. Chem. Soc.* **1963,** 381-382.

(48) Novak, B. M.; Deming, T. J. Block Copolymers Via Living Transition Metal Initiated Polymerizations: Change of Mechanism and Bimetallic Initiator Approaches. *Polymer Preprints (American Chemical Society, Division of Polymer Chemistry)* **1993,** *34,* 207-208.

(49) Deming, T. J. Controlled Polymerization of α-Aminoacid *N*-Carboxyanhydrides Using Transition Metal Initiators. *Book of Abstracts, 211th ACS National Meeting, New Orleans, LA, March 24-28* **1996,** OLY-041.

(50) Novak, B. M.; Goodwin, A. A.; Schlitzer, D.; Patten, T. E.; Deming, T. J. Building Chiral Molecular Architectures Using Living Transition-Metal Initiated Polymerizations. *Polymer Preprints (American Chemical Society, Division of Polymer Chemistry)* **1996,** *37,* 446-447.

(51) Deming, T. J. Transition Metal-Amine Initiators for Preparation of Well-Defined Poly(γ-Benzyl L-Glutamate). *Journal of the American Chemical Society* **1997,** *119,* 2759-2760.

(52) Deming, T. J.; Curtin, S. A.; Goodwin, A. A. Use of Transition Metal Catalysis to Prepare Functionalized and Block Copolypeptide Materials. *Polymeric Materials Science and Engineering* **1999,** *80,* 37-38.

(53) Deming, T. J. Living Polymerization of α-Amino Acid-*N*-Carboxyanhydrides. *Journal of Polymer Science, Part A: Polymer Chemistry* **2000,** *38,* 3011-3018.

(54) Seidel, S. W.; Deming, T. J. Use of Chiral Ruthenium Amido-Sulfonamide Complexes for Controlled, Enantioasymmetric Polypeptide Synthesis. *Abstracts of Papers, 224th ACS National Meeting, Boston, MA, United States, August 18-22, 2002* **2002,** MSE-132.

(55) Block, H. Poly(γ-Benzyl-*L*-Glutamate) and Other Glutamic-Acid-Containing Polymers; Gordon and Breach publishers, New York: 1983.

(56) Bird, G. R.; Blout, E. R. Polypeptides. XXV. The Infrared Streaming Dichroism of Some Synthetic Polypeptides. *Journal of the American Chemical Society* **1959,** *81,* 2499-2503.

(57) Balik, C. M.; Hopfinger, A. J. Quantization of the Solvent Effect on the Adsorption of Poly-γ-Benzyl-*L*-Glutamate. *Journal of Colloid and Interface Science* **1978,** *67,* 118-126.

(58) Karasz, F. E.; O'Reilly, J. M. Deuteration and Solvent Composition Effects in the Helix-Coil Transition of Poly-γ-Benzyl-*L*-Glutamate. *Biopolymers* **1966,** *4,* 1015-1023.

(59) Karasz, F. E.; Gajnos, G. E. Enthalpies of Helix-Coil Transitions in Polypeptides. *Biopolymers* **1974,** *13,* 725-734.

(60) Ushiki, H.; Mita, I. Helix-Coil Transition Behavior of Terminal Group of Poly(γ-Benzyl *L*-Glutamate) Studied by Depolarization of Fluorescence. *Polymer Journal (Tokyo, Japan)* **1981,** *13,* 837-844.

(61) Norisuye, T.; Teramoto, A.; Fujita, H. Solution Properties of Synthetic Polypeptides. XIII. Dimensions of Interrupted Helixes of Poly(γ-Benzyl L-Glutamate). *Polymer Journal (Tokyo, Japan)* **1973,** *4,* 323-331.

(62) Matsumoto, T.; Teramoto, A. Solution Properties of Synthetic Polypeptides. XVII. Stability of the Alpha-Helical Conformation of Poly (γ-Benzyl *L*-Glutamate) in Helicogenic Solvents. *Biopolymers* **1974,** *13,* 1347-1356.

(63) Ushiki, H.; Mita, I. Study on the Fluorescence Depolarization of a Chromophore Attached to Polymer Chain End. III. Aggregation and Helix-Coil Transition Behavior of Poly(γ-Benzyl *L*-Glutamate) in *m*-Cresol and Benzene at Various Temperatures. *Polymer Journal (Tokyo, Japan)* **1985,** *17,* 1297-1300.

(64) Karasz, F. E.; Gajnos, G. E. Relative Stability of the a-Helix of Deuterated Poly(γ-Benzyl-*L*-Glutamate). *Biopolymers* **1976,** *15,* 1939-1950.

(65) Sugai, S.; Kamashima, K.; Nitta, K. Poly(g-Alkyl L-Glutamates). II. Optical Rotatory Dispersion Studies in Organic Solvents. *Journal of Polymer Science, Polymer Physics Edition* **1968,** *6,* 1065-1081.

(66) Lin, J.; Abe, A.; Furuya, H.; Okamoto, S. Liquid Crystal Formation Coupled With the Coil-Helix Transition in the Ternary System Poly(γ-Benzyl *L*-Glutamate)/Dichloroacetic Acid/Dichloroethane. *Macromolecules* **1996,** *29,* 2584-2589.

(67) Blout, E. R.; DesRoches, M. E. Polypeptides. XXIV. Preparation of High-Molecular-Weight Polypeptides. *Journal of the American Chemical Society* **1959,** *81,* 370-372.

(68) Fasman, G. D.; Idelson, M.; Blout, E. R. The Synthesis and Conformation of High Molecular Weight Poly(ε-Carbobenzyloxy-*L*-Lysine) and Poly-*L*-Lysine-HCl. *Journal of the American Chemical Society* **1961,** *83,* 709-712.

(69) Nishioka, N.; Maekawa, A.; Teramoto, A. Solution Properties of Synthetic Polypeptides. XXI. Solvent Effect on the Helix-Coil Transition of Poly(ε-Carbobenzoxy *L*-Lysine). *Biopolymers* **1978,** *17,* 665-675.

(70) Hayashi, T.; Emi, S.; Nakajima, A. Helix-Coil Transition of Poly(ε-Carbobenzyloxy-*L*-Lysine) in *m*-Cresol. *Polymer* **1975,** *16,* 396-400.

(71) Omura, I.; Teramoto, A.; Fujita, H. Dielectric Dispersion of Polypeptide Solutions. II. Helix-Coil Transition of Poly(ε-Carbobenzoxy-*L*-Lysine) in *m*-Cresol. *Macromolecules* **1975,** *8,* 284-290.

(72) Nakamoto, K.; Suga, H.; Seki, S.; Teramoto, A.; Norisuye, T.; Fujita, H. Solution Properties of Synthetic Polypeptides. XIX. Heat Capacity Measurements on the System of Poly(ε-Carbobenzyloxy-*L*-Lysine) and *m*-Cresol in the Helix-Coil Transition Region. *Macromolecules* **1974,** *7,* 784-788.

(73) Hall, D. B.; Underhill, P.; Torkelson, J. M. Spin Coating of Thin and Ultrathin Polymer Films. *Polymer Engineering and Science* **1998,** *38,* 2039-2045.

(74) Prosycevas, I.; Tamulevicius, S.; Guobiene, A. The Surface Properties of PS/PMMA Blends Nanostructured Polymeric Layers. *Thin Solid Films* **2004,** *453-454,* 304-311.

(75) Yokoi, H.; Kinoshita, T. Molecular Orientation Control in Amphiphilic α-Helical Copolypeptide Monolayer at Air/Water Interface. *Chemistry Letters* **2004,** *33,* 426-427.

(76) Ganesh, S.; Jayakumar, R. Monolayer Formation of Short Helical Turn Forming Peptide Derivatives at the Air-Water and Air-Solid Interfaces. *Chemical Physics Letters* **2003,** *380,* 681-688.

(77) Cao, X.; Sui, G.; Huo, Q.; Leblanc, R. M. Langmuir and Langmuir-Blodgett Films of a Novel Tryptophan Peptide Lipid. *Chemical Communications (Cambridge, United Kingdom)* **2002,** 806-807.

(78) Girard-Egrot, A. P.; Godoy, S.; Blum, L. J. Enzyme Association With Lipidic Langmuir-Blodgett Films: Interests and Applications in Nanobioscience. *Advances in Colloid and Interface Science* **2005,** *116,* 205-225.

(79) Roberts, G. G. Langmuir-Blodgett Films. *Contemporary Physics* **1984,** *25,* 109-128.

(80) Decher, G.; Hong, J.-D.; Lowack, K.; Lvov, Y.; Schmitt, J. Layer-by-Layer Adsorption: The Solid/Liquid-Interface As a Template for the Controlled Growth of Well-Defined Nanostructures of Polyelectrolytes, Proteins, DNA, and Polynucleotides. *NATO ASI Series, Series C: Mathematical and Physical Sciences* **1994,** *446,* 267-272.

(81) Decher, G.; Lehr, B.; Lowack, K.; Lvov, Y.; Schmitt, J. New Nanocomposite Films for Biosensors: Layer-by-Layer Adsorbed Films of Polyelectrolytes, Proteins or DNA. *Biosensors & Bioelectronics* **1994,** *9,* 677-684.

(82) Peterson, I. R. Langmuir-Blodgett Films. *Journal of Physics D: Applied Physics* **1990,** *23,* 379-395.

(83) Dietz, E.; Fery, N.; Hamann, K. Polyreactions and Pigment Surfaces. IV. Polymerization of N-Carboxy-α-Amino Acid Anhydrides on a Silicon Dioxide Surface. *Angewandte Makromolekulare Chemie* **1974,** *35,* 115-129.

(84) Hamann, K.; Laible, R.; Horn, J. Polymer Reactions on Solid Surfaces. *Polymer Science and Technology (Plenum)* **1975,** *9A,* 93-105.

(85) Wieringa, R. H.; Schouten, A. J. Oriented Thin Film Formation by Surface Graft Polymerization of γ-Methyl *L*-Glutamate N-Carboxyanhydride in the Melt. *Macromolecules* **1996,** *29,* 3032-3034.

(86) Chang, Y. C.; Frank, C. W. Vapor Deposition-Polymerization of α-Amino Acid N-Carboxy Anhydride on the Silicon(100) Native Oxide Surface. *Langmuir* **1998,** *14,* 326-334.

(87) Wang, Y.; Chang, Y. C. Grafting of Homo- and Block Co-Polypeptides on Solid Substrates by an Improved Surface-Initiated Vapor Deposition Polymerization. *Langmuir* **2002,** *18,* 9859-9866.

(88) Wang, Y.; Chang, Y. C. Grafting of Diblock Copolypeptides on Solid Substrates. *Polymeric Materials Science and Engineering* **2001,** *84,* 29-30.

(89) Chang, Y. C.; van Esbroeck, H.; Frank, C. W. Surface Initiated Polymerization of Polyglutamate Copolymers. *Polymer Preprints (American Chemical Society, Division of Polymer Chemistry)* **1995,** *36,* 121-122.

(90) Chang, Y. C.; Frank, C. W. Surface Polymerization of Poly(γ-Alkyl *L*-Glutamate) on Solid Substrates. *Macromolecular Symposia* **1997,** *118,* 641-646.

(91) Heise, A.; Menzel, H.; Yim, H.; Foster, M. D.; Wieringa, R. H.; Schouten, A. J.; Erb, V.; Stamm, M. Grafting of Polypeptides on Solid Substrates by Initiation of N-Carboxyanhydride Polymerization by Amino-Terminated Self-Assembled Monolayers. *Langmuir* **1997,** *13,* 723-728.

(92) Worley, C. G.; Linton, R. W.; Samulski, E. T. Electric-Field-Enhanced Self-Assembly of a-Helical Polypeptides. *Langmuir* **1995,** *11,* 3805-3810.

(93) Machida, S.; Sano, K.; Sasaki, H.; Yoshiki, M.; Mori, Y. Preparation of Monolayer of Poly(γ-Benzyl-L-Glutamate) by Chemical Reaction on a Silicon Crystal Surface. *Journal of the Chemical Society, Chemical Communications* **1992,** 1626-1628.

(94) Machida, S.; Sano, K.; Sunohara, K.; Kawata, Y.; Mori, Y. The Novel Texture of a Liquid Crystal Induced by Poly-γ-Benzyl-L-Glutamate Chemical Reaction Alignment (CRA) Film. *Journal of the Chemical Society, Chemical Communications* **1992,** 1628-1629.

(95) Clarke, J.; Vincent, B. Nonaqueous Silica Dispersions Stabilized by Terminally Anchored Polystyrene: the Effect of Added Polymer. *Journal of Colloid and Interface Science* **1981,** *82,* 208-216.

(96) Ogden, A. L.; Lewis, J. A. Effect of Nonadsorbed Polymer on the Stability of Weakly Flocculated Suspensions. *Langmuir* **1996,** *12,* 3413-3424.

(97) Seebergh, J. E.; Berg, J. C. Depletion Flocculation of Aqueous, Electrosterically-Stabilized Latex Dispersions. *Langmuir* **1994,** *10,* 454-463.

(98) Chang, Y. C.; Frank, C. W. Grafting of Poly(γ-Benzyl-L-Glutamate) on Chemically Modified Silicon Oxide Surfaces. *Langmuir* **1996,** *12,* 5824-5829.

(99) Wang, Y.; Chang, Y. C. Synthesis and Conformational Transition of Surface-Tethered Polypeptide: Poly(L-Lysine). *Macromolecules* **2003,** *36,* 6511-6518.

(100) Wang, Y.; Chang, Y. C. Synthesis and Conformational Transition of Surface-Tethered Polypeptide: Poly(L-Glutamic Acid). *Macromolecules* **2003,** *36,* 6503-6510.

(101) Wang, Y.; Chang, Y. C. Alignment of Rigid-Rod Polypeptide Chains by Solvent Quenching. *Materials Research Society Symposium Proceedings* **2003,** *771,* 345-350.

(102) Wang, Y.; Chang, Y. C. Preparation of Unidirectional End-Grafted a-Helical Polypeptides by Solvent Quenching. *Journal of the American Chemical Society* **2003,** *125,* 6376-6377.

(103) Ung, T.; Liz-Marzan, L. M.; Mulvaney, P. Controlled Method for Silica Coating of Silver Colloids. Influence of Coating on the Rate of Chemical Reactions. *Langmuir* **1998,** *14,* 3740-3748.

(104) Hall, S. R.; Davis, S. A.; Mann, S. Cocondensation of Organosilica Hybrid Shells on Nanoparticle Templates: A Direct Synthetic Route to Functionalized Core-Shell Colloids. *Langmuir* **2000,** *16,* 1454-1456.

(105) Xu, X.; Asher, S. A. Synthesis and Utilization of Monodisperse Hollow Polymeric Particles in Photonic Crystals. *Journal of the American Chemical Society* **2004,** *126,* 7940-7945.

CHAPTER 2 LIVING FEATURE OF SiPCPs

2.1 Introduction

As described in Chapter 1, grafting polypeptides on solid surfaces can be traced back to the 1970's.[1;2] Two different methods were applied to chemically graft polypeptides on solid surfaces. In the "grafting onto" method, preformed polymers are deposited on a surface through the reaction between the surface-active groups and the active-end groups of the polymer chains. In the "growing from" method, the polymerization is initiated and progresses after monomers come in contact with the surface bounded initiators. Thicker polymer layers can be obtained through the "growing from" method because of the elimination of steric hindrance (details are described in Chapter 1). The "growing from" method has been widely reported for creating polypeptide-grafted surfaces.[3-12] In 1998, Frank, *et al.,* grafted PBLG on silicon surfaces by using a chemical-vapor-deposition technique, [13] and with a similar procedure Chang, *et al*., produced PLPA (poly-L- phenylalanine) –PBLG and PBLG-PCBL diblock copolymer-grafted surfaces.[6] Wieringa was able to deposit poly (*L*-glutamates) on silicone surfaces in solution.[3;14]

In this study, SiO_2 colloidal particles were functionalized with APS to introduce amino groups on their surfaces, which will act as initiator for the polymerization. The PBLG, PCBL, or the diblock copolypeptides grew from the spherical surfaces through ring-opening polymerization of NCA monomers with active NH_2 groups at the end of polymer chains. These active end groups allow the polymer to grow as more and more monomer is added. This gives the polypeptide chains a "living" character. So by this method we can control the architecture of the polypeptides by changing the concentration of monomer and the reaction time. In this chapter, the polymerization as a function of time and the effect of the amount of monomer was explored.

2.2 Experiments

2.2.1 Materials

Functionalized SiO_2 particles and NCA derivatives, including BLG-NCA and CBL-NCA, were provided by Erick Soto-Cantu. The solvent *m*-cresol (99%) and the anhydrous solvent pyridine (99.8%) were purchased from Aldrich and were used without further purification. Nanopure water was obtained by using Barnstead Nanopure Water System (18MΩ).

2.2.2 Sample Preparation

Two procedures were used to synthesize SiPCPs, *in situ* and "big batch."

2.2.2.1 Synthesis of SiPCPs *in situ*1

The PCBL-grafted SiO_2 particles were synthesized by the following procedure. A 1-mL suspension of amino-functionalized silica particles (0.24 g/mL) in pyridine was injected into a 50-mL solution of 0.12 g CBL-NCA dissolved in pyridine. The released CO_2 gas was captured and transferred to 50 mL of 1N NaOH. $NaHCO_3$ formed with the reaction of CO_2 and NaOH was titrated to determine the amount of CO_2 produced. The reaction was under N_2 and one mL of the reaction mixture was taken out for light scattering measurement after three days. One mL of a CBL-NCA mixture with the desired concentration was added and three days later, one mL of the CBL-NCA reaction mixture (at a new concentration) was taken out for DLS measurement. This procedure was repeated four times. The samples extracted from each step were measured by light scattering after three weeks and after one year. (The synthesis was performed by Sibel Turksen.)

2.2.2.2 Synthesis of the SiPCPs *in situ*2

One mL of pyridine was added to a pre-cleaned DLS tube, and then a 5-10 μL suspension of APS-functionalized Stöber spheres (0.049 g/ml) was added. The sample was homogenized by using a vortex mixture and then sonicated to ensure the Stöber spheres were dispersed in the

solvent evenly, followed by the addition of 5-15 mg BLG-NCA or CBL-NCA monomers. Several light scattering measurements were made in a period of several days, and the sample was sonicated in Branson 2510 bath sonicator for 10-15 minutes before each DLS and static light scattering (SLS) measurement. More NCA monomer was added to the DLS tube directly and then the sample was measured by light scattering. The addition and measurement routine was repeated for 4-5 consecutive times.

For these *in situ* methods, the sample was less prone to be contaminated; however, the productivity is very low and it is impossible to provide enough samples for thermogravimetric analysis (TGA) measurement.

2.2.2.3 Synthesis of SiPCPs in big batch

Eleven grams of BLG-NCA was dissolved in ~ 100 mL of anhydrous THF, and then 0.95 g of functionalized Stöber spheres in THF (10% amino groups) (ES.3.3.36A) (0.11718 g/mL) (R_h =103.2 nm) were added. The released CO_2 was captured and transferred to a cylinder filled with mineral oil. The volume of CO_2 was determined by measuring the volume of mineral oil displaced by CO_2. The reaction was completed after 6 days until the production of CO_2 was null. Then the SiPCPs were washed in pyridine (centrifugation-redispersion) 3-4 times. (The synthesis was performed by Erick Soto-Cantu.)

2.2.3 Characterization Techniques

2.2.3.1 Dynamic Light Scattering

DLS was used to determine the size of the SiPCPs dispersed in solvent. The custom-built instrument uses an ALV5000 wide-range digital autocorrelator and an HeNe laser source operating at 632.8 nm. Measurements were conducted from 30° to 90° in 15° increments. Cumulants[15] analysis was used to fit the data. By using the following equations, one can

calculate the diffusion coefficient and hydrodynamic radii of the particles. Through the electric field autocorrelation function $g^{(1)}(t)$, one can obtain the decay rate (Γ), which is the reciprocal of the decay time and consequently can calculate the diffusion coefficient D_m (equation 2.1 and 2.2)

$$g^{(1)}(t) = e^{-\Gamma t} \qquad \text{equation 2.1}$$

$$\Gamma = \tau^{-1} = q^2 D_m \qquad \text{equation 2.2}$$

Where D_m is the mutual diffusion coefficient, and q is the scattering vector defined as

$$q = \frac{4n\pi \sin(\theta/2)}{\lambda_0} \qquad \text{equation 2.3}$$

where n is the refractive index of the solvent. θ is the scattering angle and λ_0 is the wavelength of incident laser. D_m becomes D_o in a very diluted solution. The hydrodynamic radius of a sample molecule (R_h) can be calculated by the Stokes – Einstein equation:

$$R_\mathrm{h} = \frac{kT}{6\pi\eta_\mathrm{o} D_\mathrm{o}} \qquad \text{equation 2.4}$$

where k is Boltzmann's constant; T is the temperature in Kelvin; and η_o is viscosity of solvent.

2.2.3.2 Static Light Scattering

The SLS technique was applied to measure the size of the SiO_2 core of the SiPCPs. SLS experiments were made with self-built equipment incorporating a red laser at wavelength λ_o = 632.8 nm in vacuo. The scattering angle, θ, ranged from 30° to 90° with an interval angle of 5°. The radius of gyration, R_g, can be calculated from a Guinier plot when the product qR_g is sufficiently small ($qR_\mathrm{g} < \sim 1$, depending on shape). The Guinier relation is:

$$\ln(I(q)) = \ln(I(0)) - \frac{q^2 R_\mathrm{g}^2}{3} \qquad \text{equation 2.5}$$

where $q = 4\pi n \sin(\theta/2)/\lambda_\circ$, $I(0)$ is the scattering intensity extrapolated to $q = 0$ and n is the refractive index of the solution. For uniform spheres, R_g is smaller than R:

$$R_g = \sqrt{\frac{3}{5}}\, R = 0.775\, R \text{ (uniform spheres)} \qquad \text{equation 2.6}$$

Rather than use a linear fit to the low-angle data, which are often too few in number or corrupted by inhomogeneities or stray light, one may profitably fit many points to a known form factor. The downside of such an approach is that a shape and corresponding form factor,[16;17] $P(qR) = I(q)/I(q=0)$, must be assumed (the form factor is sometimes described as $P(\theta)$). This approach is effective for the large spheres and their aggregates in this study. For uniform spheres of radius R,[18]

$$P(q) = I(q)/I(q=0) = \left[\frac{3(\sin u - u\cos u)}{u^3}\right]^2 = \frac{9\pi}{2}\frac{J_{3/2}{}^2(u)}{u^3} \qquad \text{equation 2.7}$$

Where $u = qR$ and $J_{3/2}$ is the spherical Bessel function of order 3/2. Data were fitted to equation 2.7 by adjusting $I(q=0)$ and R using Microsoft Excel's Solver, a versatile nonlinear least-squares algorithm. In this dissertation, R_{SLS} is defined as $(R_{\text{sphere fit}} + R_{\text{g,Guinier plot}} \cdot \sqrt{5/3})/2$.

2.2.3.3 Differential Refractometer

A Brice-Phoenix (BP) differential refractometer was used to determine the refractive index of the polypeptides. Light meets the sample cell by passing through a wavelength filter, mirror, and adjustable slit. Four different wavelength filters are available; they are red (helium-neon laser, λ =632.8 nm), orange (sodium lamp D line, λ =589 nm), green (argon ion laser, λ = 514.5 nm), and blue (argon ion laser, λ = 488 nm). The sample cell is a cubic glass cell with a glass wall inside which is inclined at an angle from the incident beam as Figure 2.1 shows. According to Snell's law, there would be deflection between the incident light and the output

light if the refractive index of sample 1 (n_1) and sample 2 (n_2) are different. After the output light goes through a series of optical elements, the measurable signal, which is proportional to $\Delta n = n_1 - n_2$, can be obtained by the aid of a microscope. In order to get the refractive index of a polymer, diluted polymer solutions in different solvent are prepared. The solvent and the corresponding solutions are placed in the two parts of the cubic cell as sample 1 and sample 2. By plotting the change of the signals between the solvent and the solution (y axis) *vs.* the refractive index (x axis), the refractive index of the polymer can be obtained as the interception of the x-axis.

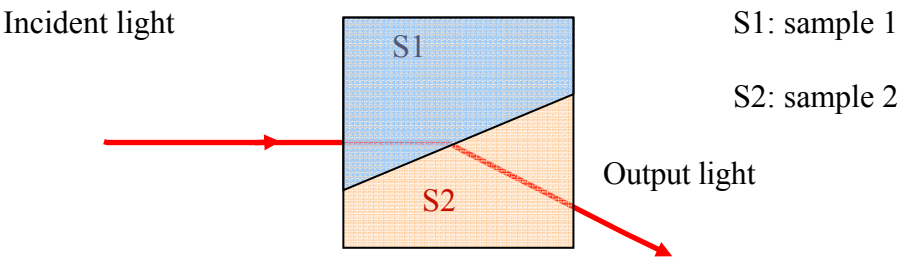

Figure 2.1 Scheme of sample cell of BP differential refractometer.

2.2.3.4 Transmission Electron Microscopy (TEM)

A JEOL 100 CX TEM was used to visualize the polypeptide-grafted particles. (The experiments were performed by Erick Soto-Cantu with help of Cindy Henk.)

2.2.3.5 Thermogravimetric Analysis (TGA)

Thermogravimetric analysis was used to measure the weight loss of the SiPCPs. The experiments were performed by using the Seiko EXSTAR 6000 system. A sample of 5 mg mass was heated from room temperature to 1000 ^{o}C with the rate of 20 ^{o}C/min under air flow (20 mL/min).(The experiments were performed by Erick Soto-Cantu.)

2.3 Results and Discussion

2.3.1 The TEM Images of Core-Shell Structure

After the SiPCPs were synthesized by the big-batch method (section 2.2.2.3), some particles were taken out for TEM experiments. Figure 2.2 is the images of SiO_2 particles.

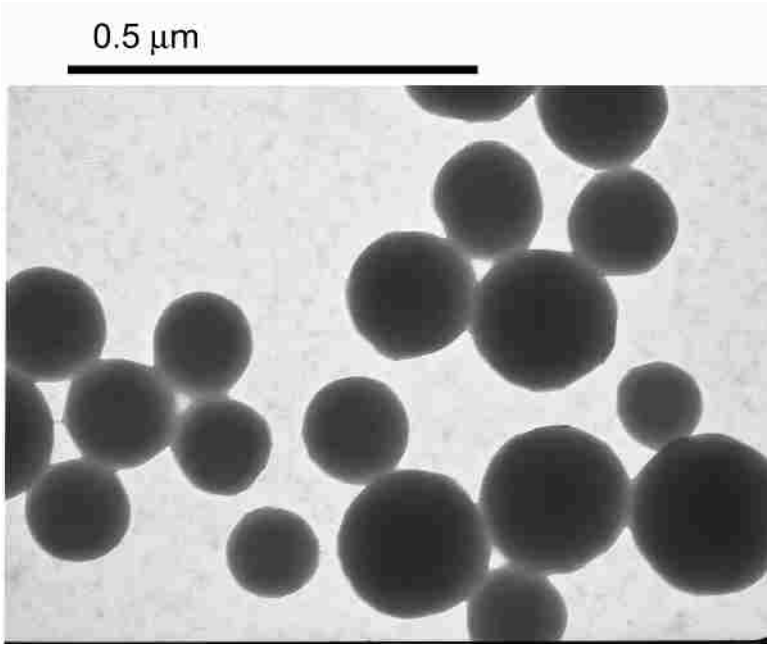

Figure 2.2 TEM image of SiO_2 particles (ES 3.127A). (Picture is provided by Erick Soto-Cantu.)

The size (diameter) of the SiO_2 is around 50-100 nm, and after the PBLG was graft on the SiPCPs (picture is not shown here), the size of the particles grows to 300-400 nm in diameter. The surfaces of SiO_2 spheres are smooth, and particles contact each other. After the PBLG was grafted, surfaces of the particles became coarse, with radiating spikes evident on the surfaces. This result demonstrates that the polypeptides were grafted on the SiO_2 spheres successfully by the "growing from" routine. TGA data (Figure 2.3) also confirms there are grafted PBLG polypeptides.

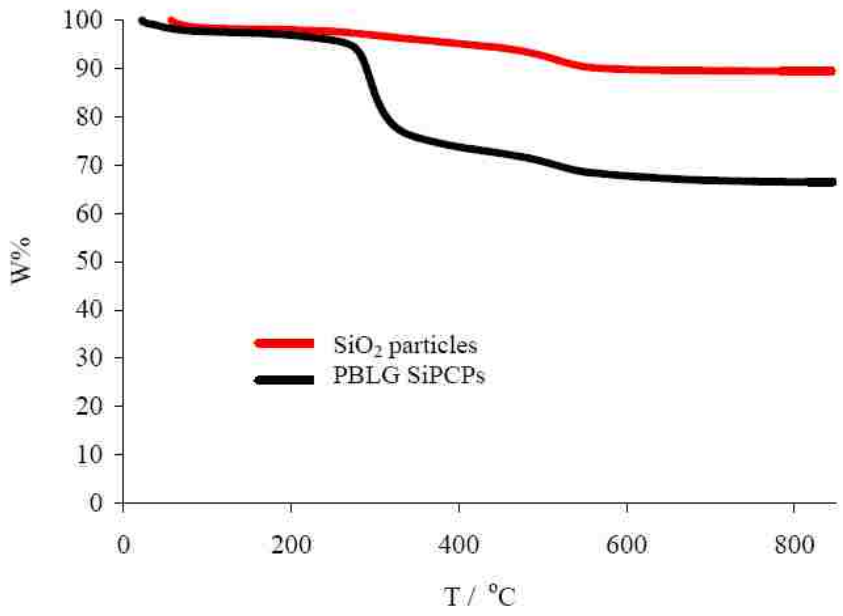

Figure 2.3 TGA results of SiO_2 particles and PBLG SiPCPs. (SiO_2 particles: ES3.127A; PBLG SiPCPs: ES3.128B. Figure is provided by Erick Soto-Cantu)

In Figure 2.3, one can see the SiO_2 particles lose about 10.5 % (red line) of total weight, and there is no more weight lost after the temperature is raised to 500°C. The weight loss is from the absorbed moisture of SiO_2 particles, and the partilces are totally dried when the temperature is above 500°C. The moisture absorption of silica is also observed by Odlyha, *et al*.[19] For SiPCPs (black line), there is a big drop of wt % curve (weight loss is about 23.5%) at about 300 °C, which should be the decomposition of PBLG. The second drop at 400-500 °C, in a similar trend as the wt % curve of SiO_2 particles, is the loss of moisture.

2.3.2 Refractive Index Matching

For polymer-grafted spheres, at least two material layers exist: the outside polymer "shell" and the inside SiO_2 "core" (There could be even more layers, e.g., in the magnetic sphere experiments, the core is a Co-SiO_2 sphere). All these layers have different densities and possibly different refractive indexes. If the refractive index (n) of the outer polymer shell is very close to

that of the solvent, there will be no scattering from the polymer shell; therefore, the R_g obtained will be that of the core. Figure 2.3 shows the difference of the refractive index of the PCBL solution characterized by the BP differential refractometer (model BP-2000-V). The intercept of the X axis (the axis of refractive index) indicates the refractive index of PCBL. Here we used the average of the results from 0.1 wt% and 1 wt% solution. From Figure 2.3, one can see that PBLG (n =1.544) and *m*-cresol (n =1.541) have a very similar refractive index. Therefore, in the PCBL-coated sphere/ *m*-cresol mixture, the PCBL shell will scatter almost nothing and the R_g obtained will be that of the core. The refractive index of PBLG is assumed to be the same as PCBL. The refractive index of pyridine is 1.510, which is a very close refractive index as PBLG or PCBL compared with SiO_2 (n = 1.445),[20] even though it is not as perfectly matched as *m*-cresol.

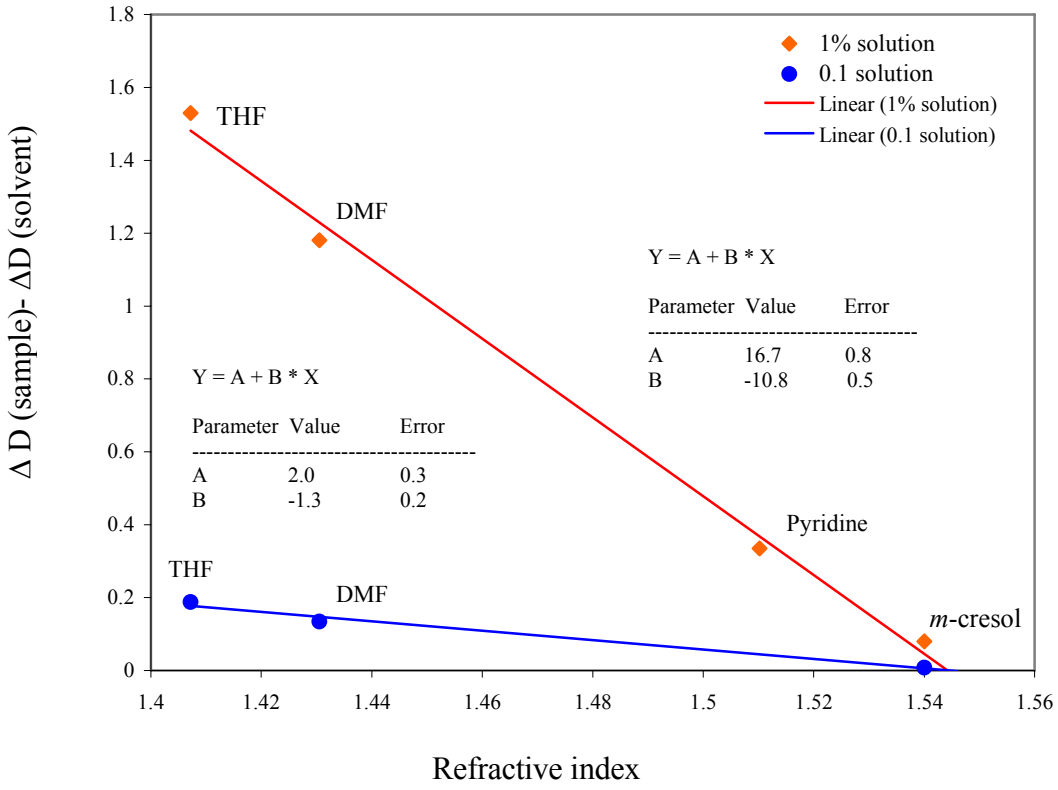

Figure 2.4 Refractive index measurement of PCBL. (M_w=10,000, Sigma). Two concentration samples (0.1 wt% and 1 wt%) were measured. The interception of the X axis (refractive index) indicates the refractive index of PCBL.

2.3.3 The Living Character of SiPCPs

2.3.3.1 Living Feature SiO_2-PCBL in Pyridine

The sample was made by the *in situ*1 method (ST4.25A-E). Figure 2.5 shows the growth of the PCBL polymer chain on a SiO_2 surface with an increased amount of monomer added. The middle panel plots the dynamic radius of SiO_2-PCBL particles *vs*. concentration of monomer. R_{DLS} is proportional to the monomer added. The measurement shows that the reaction is almost completed in less than three days and the R_{DLS} only changes slightly after 3 weeks. On the bottom panel, the low value of the polydispersity index (μ_2 / I^2) indicates the particles are nearly monodispersed comparable to latex standards. These results suggest that it is possible to control the polymer shell thickness by controlling the amount of monomer added. However, one cannot calculate the chain growth simply by the amount of monomer added. The quantity of monomer is just one of the factors; the surface density is another issue to determine the length of the polypeptide chain raised from the surface. Riffle, *et al*.[21], used back titration to quantify the amino group bound to the surface, but it seems likely that not all the amino groups on SiO_2 can react with monomer because of surface hindrance. The situation is worse after the polymerization starts and some grown polymer chains occupy the space on the surface. The samples were also investigated by SLS after two months. It was possible to determine the size of the SiO_2 core by using SLS since the PCBL shell almost doesn't scatter in pyridine. Therefore, the SLS data could provide the information of the aggregation, which also appears as a bigger hydrodynamic radius. The value of R_{SLS} was determinded by multiplying the R_g value from Guinier plots by $\sqrt{5/3}$ and also obtained by nonlinear least squares fitting to the form factor equation for spheres.[18] The average value is plotted in Figure 2.5. The difference supplies the estimated error bars. Within error, R_g does not increase with added monomer. This result

confirms that only particle shell size increases with the polymerization, and the core size is not affected. Measurements at lower angles indicated slightly larger values, which may suggest aggregation after two months. The aggregation could be reversed by sonication, even after one year. The results of D_{app} radius *vs.* scattering vector of PCBL-coated silica particles, which were measured at different monomer concentrations, indicate the particle size is independent of the scattering angle for all different concentrations of monomer measured. This result demonstrates the uniformity of the particle growth.

Table 2.1 shows the size change of PCBL-coated silica particles (ST4.25D) over one year. The sample used for this analysis was produced at 0.004 g/mL added monomer. The results show that the aggregation is reversible by repetitive sonication. After sonicating the sample twice, the particle radius, R_h, returned to a value similar to that measured one year earlier. The sample was centrifuged and a drop of water was added to verify the absence of free polymer initiated by solvent and the broken polymer from sonication (see next paragraph). The downward trend of the polydispersity index, μ_2/Γ^2, with angle can be explained by some persistent aggregates that could not be separated into individual particles by sonication.

The sample was centrifuged at 3000 rpm (centrifugal force ≈ 11.9 kg·m·s^{-2}) for 1 hour after all these measurements were completed, and the supernatant phase was measured by DLS. If the supernatant phase scatters enough light, it means there were possibly some free polymers which may increase the viscosity of the mixture and consequently let the R_h appear larger. No scattering signal of the supernatant phase was observed, and there was no white precipitate produced after the one drop of water was added. This provides strong evidence for the lack of free polymer or broken polymer from sonication in the mixture.

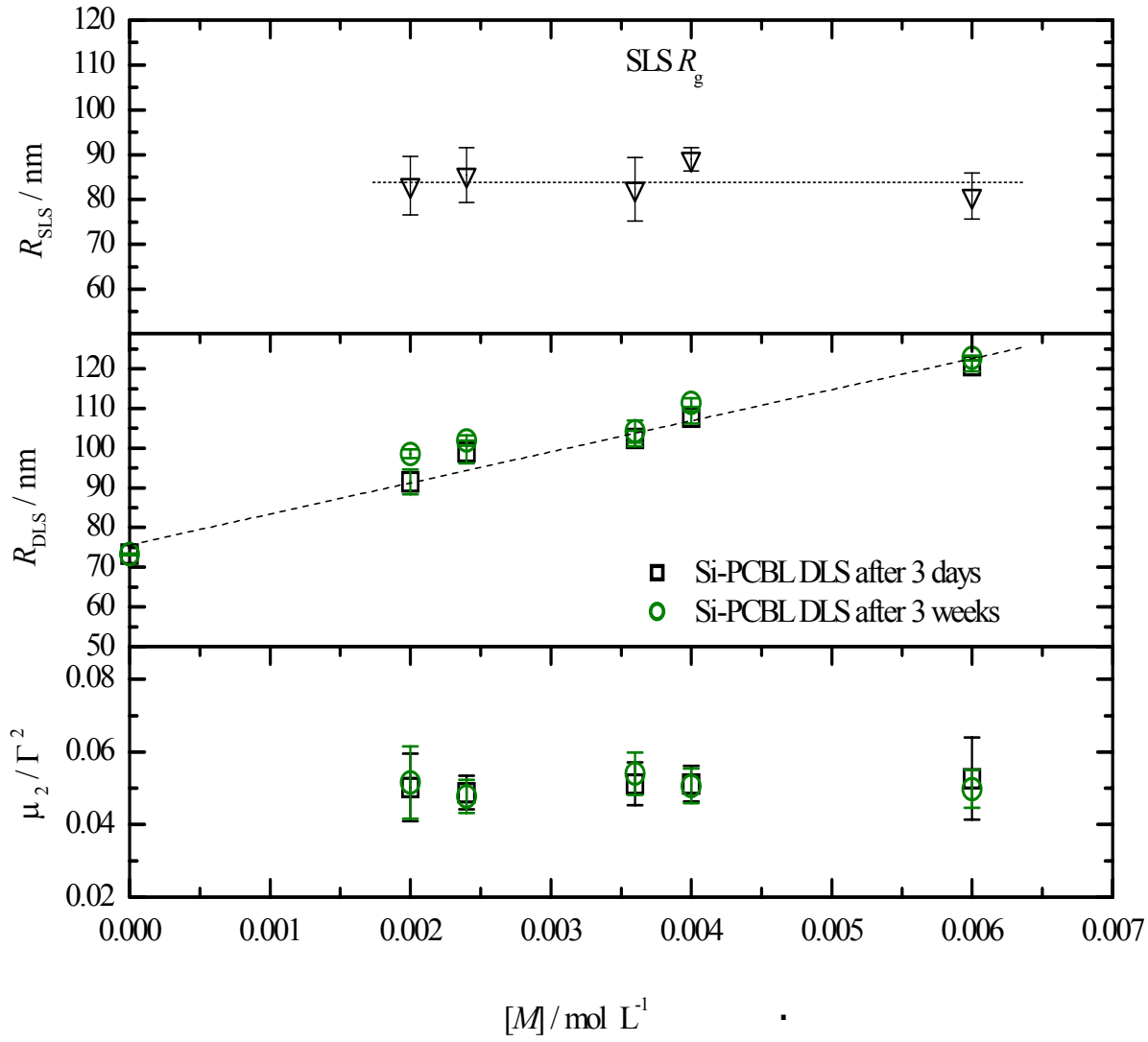

Figure 2.5 Light scattering results for PCBL SiPCPs in pyridine as a function of concentration of monomer.(ST4.25A-E) Upper pane: R_{SLS} data point was obtained by taking the average of a value from a nonlinear fit to the spherical particle form factor and another from a Guinier plot, multiplied by $\sqrt{5/3}$ to reflect the conversion from R_g to R. The difference supplies the estimated error bars. Middle panel: Hydrodynamic radii of PCBL SiPCPs as function of monomer concentration by using multi-angle light scattering. The tests were done 3 days and 3 weeks after the monomer was added; Lower panel: polydispersity index, μ_2/Γ^2, error bars reflect average over different scattering angles.

Table 2.1 R_h and R_g of PCBL SiPCPs (0.004 g/mL monomer added) (ST4.25D)

Time	R_h (DLS) (nm)	R_g (SLS) (Guinier) (nm)	μ_2/Γ^2 30°	μ_2/Γ^2 90°	μ_2/Γ^2 Avg	μ_2/Γ^2 trend with q^2
3 weeks later	111 ± 1	78 ± 5	0.04 ± 0.07	0.03 ± 0.09	0.04 ± 0.02	no trend
1 year later (no sonication)	170 ± 7	109 ± 5	0.19 ± 0.01	0.12± 0.08	0.16 ± 0.05	down
1 year later 1st sonication	123 ± 1	----------	0.14 ± 0.05	0.05 ± 0.00	0.13± 0.04	down
1 year later 2nd sonication	104 ± 6	77 ± 3	0.20 ± 0.01	0.06 ± 0.02	0.13 ± 0.06	down

2.3.3.2 Living Feature of SiO_2- PBLG in Pyridine

BLG-NCA can also polymerize on the SiO_2 surface just like CBL-NCA, and the product is a SiO_2 – PBLG sphere.[22] In this part, the "living feature" at short-time range was studied. The sample was made by the *in situ*2 routine. The Stöber spheres and BLG-NCA were provided by Erick Soto-Cantu. CO_2 gas was released occasionally under N_2 instead of being trapped with NaOH. The 7 mg NCA (the average amount of NCA added) would produce 0.6 mL CO_2 maximally, which is less than 5% of the volume of the DLS tube, so it is assumed the pressure change will not affect the equilibrium of the reaction.

Figure 2.6 shows the PBLG polymer chains' growth increased with an increasing amount of added monomer (JQ3.69A). The numbers "1-4" represent four sequential monomer additions. The broken-lines present the trend of R_h, R_g and $R_{spherical\ fit}$ (the definitions of R_g and $R_{spherical\ fit}$ are in section 2.2.3.2). At steps 1-4, 5.1 mg, 5.3 mg, 4.9 mg, and 5.5 mg BLG-NCA were added to the reaction suspension. Both R_g and $R_{spherical\ fit}$ almost remained the same with an increased amount of monomer, which confirms the sample is not aggregated. The "stair-like" trend of R_h means: 1) the NH_2 groups at the end of PBLG chain always keep active, so the polymerization could be reactivated with every addition; 2) the reaction was completed in just one day. After one day, the R_h stayed unchanged, and one can see the flat plateau for the following couple of days; 3) with a similar amount of monomer added in each step, the increments of R_h are similar at each step. To exam the presence of free polymer, the technique described above for PCBL-SiPCPs were used. After all the measurements of sample JQ 3.69A were completed, the sample was centrifuged at 3000 rpm (centrifugal force ≈ 11.9 $kg{\cdot}m{\cdot}s^{-2}$) for 1 hour. The supernatant phase was measured by DLS and then one drop of water was added in. Lack of scattering signal and no white precipitate observed confirmed there was no free polymer.

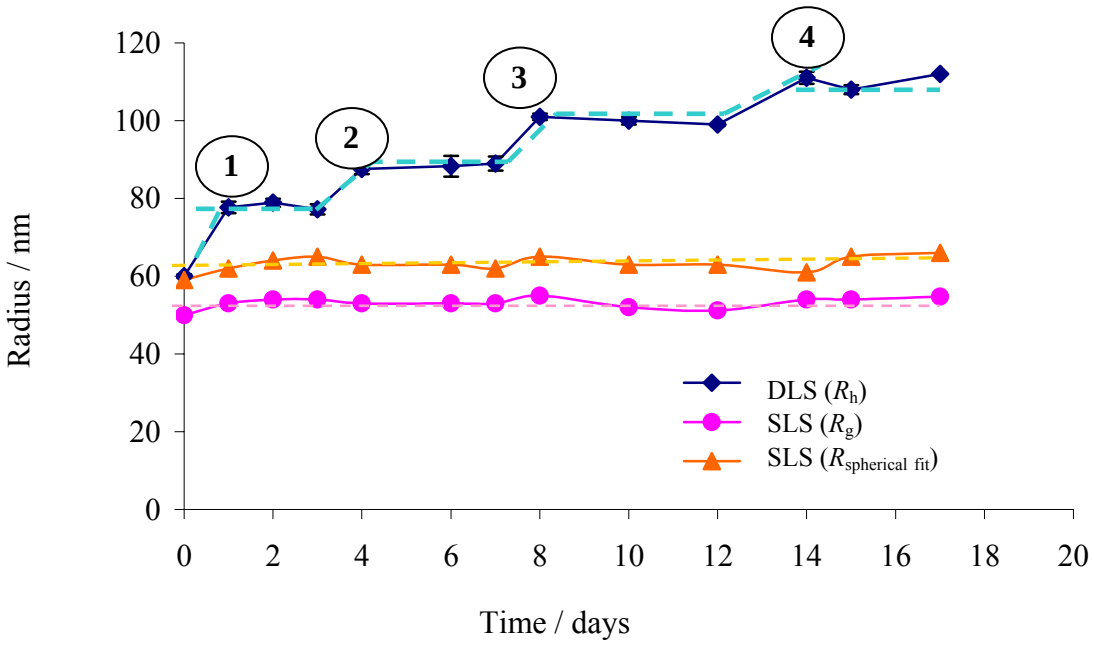

Figure 2.6 Size growth of PBLG SiPCPs as a function of time and the amount of monomer added. (JQ3.69A). 5.1 mg, 5.3mg, 4.9 mg and 5.5 mg BLG-NCA monomer was added at steps 1-4 respectively. DLS (R_h) was obtained from multi-angle DLS measurements; SLS (R_g) data was from a Guinier plot; and SLS ($R_{spherical\ fit}$, definition is in section 2.2.3.2) was from a nonlinear fit to the spherical particle form factor.

Table 2.2 is the comparison of two samples with different amounts of monomer added. For sample JQ3.69A, about 5 mg monomer was added at each step and for sample JQ3.72A, about 10 mg monomer was added. For sample JQ3.72A, there is almost double the amount of monomer added at each step, but the polymer chains don't grow up twice as long as sample JQ3.69A. This *may be* because after the first addition of monomer, particles in sample JQ3.72A have more polymer chains on the surface than sample JQ3.69A. After the polymerization of the first addition was completed, the grown polymer chains on the surface blocked the area around the surface and, consequently, when more monomer was added, the monomer was limited to react with the NH_2 at the end of the polymer chain. Therefore, in steps 2-4, the ratio of monomer obtained/chain of sample JQ3.72A to sample JQ3.69A is less than 2.

Techniques that can measure the surface density, such as TGA or gel permeation chromatography-light scattering (GPC-LS), are necessary to explain this observation. GPC-LS can measure the molecular weight and concentration of polypeptide, so one needs to cut off the SiO_2 core, e.g., dissolve the core by using HF before take the measurement with GPC-LS. As the samples were prepared with the *in situ2* method, only small amounts of SiPCPs were produced, preventing this path of study. One hopes that with the big batch method enough product for surface density measurements can be obtained.

Table 2.2 Comparison of two samples with different amounts of BLG-NCA monomer added at each step.

	Sample JQ3.69A			Sample JQ3.72A		
Step	NCA added (mg) at each step	Cumulative NCA added (mg)	R_h (nm)	NCA added (mg) at each step	Cumulative NCA added (mg)	R_h (nm)
0	0.00	0.00	60.0 ± 0.2	0.00	0.00	60.0 ± 0.2
1	5.10	5.10	80.5 ± 1.0	9.80	9.80	82.5 ± 1.5
2	5.30	10.40	92.3 ± 2.7	9.33	19.13	95.7 ± 0.3
3	4.90	15.30	103.2 ± 1.8	9.83	28.96	108.2 ± 5.5
4	5.57	20.87	114.6 ± 1.6	-------	-------	-------

2.3.4 Copolymer SiO_2- polypeptide Particles

The "living feature" of the SiPCPs, which is confirmed in part 2.3.3, leads us to consider grafting copolymer chains. Through the same synthetic route used to obtain SiO_2-PBLG in pyridine with the *in situ*2 method, the PBLC and PCBL block copolymer were grafted onto the surface. The Stöber sphere, CBL-NCA and BLG-NCA monomer were provided by Erick Soto-Cantu. The chain-length increments with the amount of added monomer are presented in Figure 2.7 (JQ3.121A, arabic numbers 1 and 2 indicate the PBLG blocks and letters A and B indicate the PCBL blocks). First 5.5 mg (3.4 E-05 mol)BLG-NCA was added in step 1 and PBLG polymer chains were formed. After the polymerization was completed, 6.4 mg (3.1 E-05 mol) of CBL-NCA monomer was added and the PCBL block was grafted at the end of the PBLG part in step A. The same procedure (step 1 and A) was repeated to graft another PBLG-PCBL block. Again, almost level SLS data prove there is no aggregation.

Table 2.3 is the comparison of size growth of co-block polymer-grafted SiPCPs with different grafting sequences. One can see copolymers can be grown no matter the sequence. In table 2.3, sample JQ3.185A has PBLG as the first layer, and then PCBL chains grew from the end of PBLG chains. Sample JQ3.185B is made on an opposite processor, and the results don't show any noticeable effect of the sequence.

The existence of free polymer in the SiO_2-copolypeptide was investigated by centrifuging the sample and adding one drop of water to the supernatant phase. No white precipitant observed confirmed there was no free polymer in the solution.

2.4 Conclusions

PBLG or PCBL polypeptide chains were attached on SiO_2 using the "growing from' methods. The polypeptide grafted silica particles are called silica polypeptide composite particles

(SiPCPs). TEM pictures and TGA data confirm the attachment of the polymer chains. Polymerization of BLG-NCA or CBL-NCA was initiated and processed on the SiO_2 surface through ring-opening polymerization and the NH_2 groups were left at the end of the polymer chains. Polymer chains continued to grow as long as additional monomer was added. The chain growth of PBLG and PCBL as a function of time was investigated in this chapter. The results show that the polymerization of each addition of monomer can be completed in 1-2 days. The particles tend to aggregate after a long period of time, and the aggregation can be broken down with ultrasonication. Block copolymers can be grafted on SiO_2 with the same synthetic route, and our results indicate that the grafting sequences don't affect the polymer growth.

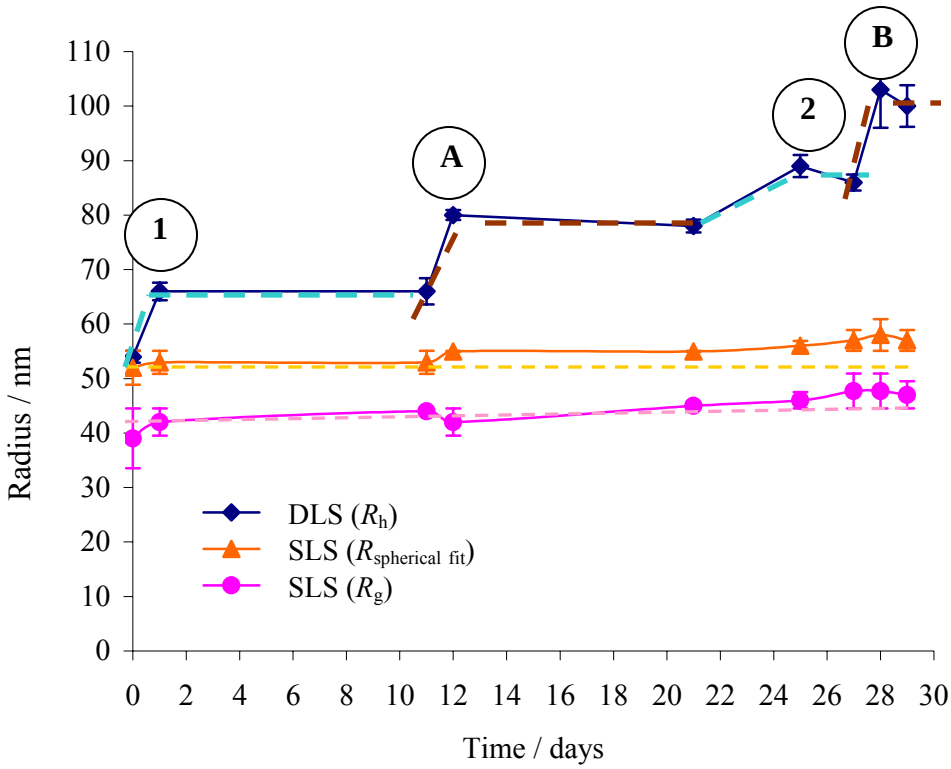

Figure 2.7 Size growth of PBLG-PCBL copolymer SiPCPs as a function of time and the amount of monomer added.(JQ3.121A) 5.5 mg BLG-NCA, 6.4 mg CBL-NCA, 5.15 mg BLG-NCA and 9.13 mg CBL-NCA monomer was added at steps 1,A,2 and B respectively. DLS (R_h) was obtained from multi-angle DLS measurements; SLS (R_g) data was from a Guinier plot; and SLS ($R_{spherical\ fit}$) was from a nonlinear fit to the spherical-particle-form-factor.

Table 2.3 Comparison of the sequence of polypeptide block grafted on SiO_2

Sample JQ3.185A (PBLG-PCBL)				Sample JQ3.185B (PCBL-PBLG)			
monomer added (mg) at each step	R_h (nm)	$R_{spherical\ fit}$ (nm)	R_g (nm)	monomer added (mg) at each step	R_h (nm)	$R_{spherical\ fit}$ (nm)	R_g (nm)
0	53.5 ± 1.5	54.0 ± 1.0	40.1 ± 1.4	0	53.5 ± 1.5	54.0 ± 1.0	40.1 ± 1.4
5.57 (BLG-NCA)	66.1 ± 0.4	55.0 ± 0.0	43.2 ± 0.8	5.87 (CBL-NCA)	71.7 ± 0.3	56.0 ± 1.0	44.3 ± 1.2
7.64 (CBL-NCA)	84.1 ± 2.4	53.5 ± 3.5	43.0 ± 1.8	7.31(BLG-NCA)	80.4 ± 0.5	56.0 ± 1.0	45.7 ± 2.2

2.5 Future Work

As shown in chapters 2, SiPCPs were successfully prepared via the "grafting onto" method. Although satisfactory results were obtained as indicated by characterization techniques such as DLS, and TEM, the grafting density, which can be measured by TGA, concerns us and consequently we sought an alternate method to produce SiPCPs with high yield. With the innovation of "click chemistry", the "grafting onto" method is again being considered. This method can be a challenge because of the tiny size of the SiO_2 particles and the possible destabilization of the cores by rod depletion; nevertheless, it may be worth the try.

The NMR and IR data, which provide the chemical information, are necessary for both homo- and copolypeptide grafted SiPCPs. The comparison (NMR and IR data) of the free

polypeptides, SiPCPs and the free polypeptides that are produced by dissolving the core of SiPCPs is preferred. The comparison can provide information on whether the polypeptides change their properties when they are located on spherical surfaces. Further investigations can seek to determine the effect of different surface densities on polypeptide conformation.

In order to measure the molecular weight and molecular weight distribution, one can dissolve the SiO_2 core of SiPCPs by using HF, and then measure the "cut off" polypeptide with GPC-LS. The GPC-LS data can also provide information about grafted surface density.

The "living future" of SiPCPs in this study was investigated daily or even longer (for PCBL SiPCPs, the sample was measured after 3 days and after 3 weeks). The shorter time range measurement such as hour by hour can provide chain growth kinetics. A possible experimental plan can be 1) synthesize the SiPCPs with *in situ 2* method and measure the "real time" chain growth with multi-angle DLS; 2) synthesize the SiPCPs by using big batch method, remove some sample every hour and measure the "aliquoted sample", subsequently, wash/rinse off the free polymers (the washing process is necessary for terminating the polymerization).
Making deuterated onion structures of homo- or copolypeptide grafted SiPCPs is another interesting project. With the help of SANS (small angle neutron scattering), one can investigate the thickness and location of the polypeptide chain.

2.6 References

1) Dietz,E.; Fery,N.; Hamann,K. Polyreactions and pigment surfaces. IV. Polymerization of N-carboxy-α-amino acid anhydrides on a silicon dioxide surface. *Angewandte Makromolekulare Chemie* **1974**, *35*, 115-129.

2) Hamann,K.; Laible,R.; Horn,J. Polymer reactions on solid surfaces. *Polymer Science and Technology (Plenum)* **1975**, *9A*, 93-105.

3) Wieringa,R.H.; Siesling,E.A.; Geurts,P.F.M.; Werkman,P.J.; Vorenkamp,E.J.; Erb,V.; Stamm,M.; Schouten,A.J. Surface Grafting of Poly(*L*-glutamates). 1. Synthesis and Characterization. *Langmuir* **2001**, *17*, 6477-6484.

4) Wieringa,R.H.; Siesling,E.A.; Werkman,P.J.; Vorenkamp,E.J.; Schouten,A.J. Surface Grafting of Poly(*L*-glutamates). 3. Block Copolymerization. *Langmuir* **2001**, *17*, 6491-6495.

5) Wang,Y.; Chang,Y.C. Grafting of diblock copolypeptides on solid substrates. *Polymeric Materials Science and Engineering* **2001**, *84*, 29-30.

6) Wang,Y.; Chang,Y.C. Grafting of Homo- and Block Co-polypeptides on Solid Substrates by an Improved Surface-Initiated Vapor Deposition Polymerization. *Langmuir* **2002**, *18*, 9859-9866.

7) Li,C.; Bansal,A.; Chen,Q.; Lewis,S.; Kumar,S.; Schadler,L.; Benicewicz,B. Synthesis of Polymer Brushes Grafted Silica Nanoparticles via Surface Reversible Addition-Fragmentation Chain Transfer (RAFT) Polymerization. *Abstracts, 32nd Northeast Regional Meeting of the American Chemical Society, Rochester, NY, United States, October 31-November 3* **2004**, GEN-122

8) Kurita,K.; Kanari,M.; Koyama,Y. Studies on chitin. 11. Graft copolymerization of γ-methyl *L*-glutamate NCA onto water-soluble chitin. *Polymer Bulletin (Berlin, Germany)* **1985**, *14*, 511-514.

9) Heise,A.; Menzel,H.; Yim,H.; Foster,M.D.; Wieringa,R.H.; Schouten,A.J.; Erb,V.; Stamm,M. Grafting of Polypeptides on Solid Substrates by Initiation of N-Carboxyanhydride Polymerization by Amino-Terminated Self-Assembled Monolayers. *Langmuir* **1997**, *13*, 723-728.

10) Chang,Y.C.; Frank,C.W. Grafting of Poly(γ-benzyl-*L*-glutamate) on Chemically Modified Silicon Oxide Surfaces. *Langmuir* **1996**, *12*, 5824-5829.

11) Koga,T.; Nagaoka,A.; Higashi,N. Fabrication of a switchable nano-surface composed of acidic and basic block-polypeptides. *Colloids and Surfaces, A: Physicochemical and Engineering Aspects* **2006**, *284+285*, 521-527.

12) Liu,Z.M.; Xu,Z.K.; Wang,J.Q.; Yang,Q.; Wu,J.; Seta,P. Surface modification of microporous polypropylene membranes by the grafting of poly(γ -stearyl-*L*-glutamate). *European Polymer Journal* **2003**, *39*, 2291-2299.

13) Chang,Y.C.; Frank,C.W. Vapor Deposition-Polymerization of a-Amino Acid *N*-Carboxy Anhydride on the Silicon(100) Native Oxide Surface. *Langmuir* **1998**, *14*, 326-334.

14) Wieringa,R.H.; Siesling,E.A.; Werkman,P.J.; Vorenkamp,E.J.; Schouten,A.J. Surface Grafting of Poly(*L*-glutamates). 3. Block Copolymerization. *Langmuir* **2001**, *17*, 6491-6495.

15) Koppel,D.E. Analysis of Macromolecular Polydispersity in Intensity Correlation Spectroscopy. Method of Cumulants. *Journal of Chemical Physics* **1972**, *57*, 4814-4820.

16) Tanford,C.*Physical Chemistry of Macromolecules*; 1961;

17) Van Holde,K.E.*Physical Biochemistry*; Prentice Hall: 1985;

18) Kerker,M.*The scattering of light and other electromagnetic radiation*; Academic press: 1969;

19) Odlyha,M.; Scott,R.P.W.; Simpson,C.F. The hydroxyl content of silica gel. *Journal of Thermal Analysis* **1993**, *40*, 1197-1212.

20) Viravathana,P.; Marr,D.W.M. Synthesis of colloidal aluminosilicate for light-scattering investigations. *Journal of Colloid and Interface Science* **2003**, *265*, 15-22.

21) Vadala,M.L.; Zalich,M.A.; Fulks,D.B.; St.Pierre,T.G.; Dailey,J.P.; Riffle,J.S. Cobalt-silica magnetic nanoparticles with functional surfaces. *Journal of Magnetism and Magnetic Materials* **2005**, *293*, 162-170.

22) Fong,B.; Russo,P.S. Organophilic Colloidal Particles with a Synthetic Polypeptide Coating. *Langmuir* **1999**, *15*, 4421-4426.

CHAPTER 3 PHASE BEHAVIOR AND PROBE DIFFUSION OF SiPCPs / PBLG MIXTURE

3.1 Introduction

3.1.1 The Phase Behavior of Rod-Like Polymer and Spherical Colloids

Colloidal mixtures exist in many industrial areas such as paints, lubricants, and adhesives.[1] The stability of the suspension is one of the main issues in colloidal science. In the paint industry, the product is expected to be stable without any phase separation throughout long periods of time, while, on the other hand the rapid sedimentation is required for water treatment or mineral recovery.[2;3] Relevant to the production of SiPCPs, especially for the "grafting onto" method, rod-like polypeptides co-exist with spherical SiO_2 or SiPCPs particles. The stability of the mixture directly affects the grafting procedure and the final SiPCPs product. The description of the interaction between rods, spheres and the depletion attraction of rod-sphere mixtures is addressed here.

3.1.1.1 Density Functional Theory [4]

The Density Functional Theory (DFT)[4] is the major theory used for studying the ordering transitions in hard-particle fluids. The simplest DFT version only counts the second virial approximation and such simplification can be applied to some isotropic solutions,[5;6] However, in the highly ordered rods' smectic/nematic phase, the third and fourth virial coefficients are not neglected. In simplified DFT, the free energy of the hard-particles suspension is expressed as equation 3.1:

$$\frac{F}{K_b T} = \int_V d\mathbf{r}\rho(\mathbf{r})\ln(\rho(\mathbf{r})) - \frac{1}{2}\int_V d\mathbf{r}_1 \int_V d\mathbf{r}_2 \rho(\mathbf{r}_1)\rho(\mathbf{r}_2)\beta(\mathbf{r}_1,\mathbf{r}_2) \qquad \text{equation 3.1}^5$$

where, $\rho(\mathbf{r})$ is the density of the particle; $\mathbf{r_1}$ and $\mathbf{r_2}$ are vectors related to the particle's position and orientation; $\beta(\mathbf{r_1}, \mathbf{r_2})$ is Meyer-Meyer overlap function, which is -1 when two particles (located at $\mathbf{r_1}$ and $\mathbf{r_2}$, respectively) overlap each other, while it is 0 when the two particles are totally separated. The first integral in equation 3.1 is the ideal part of free energy; the second integral presents the interaction energy which comes from the second virial approximation and is proportional to excluded volume. Theoretically, if particles are distributed uniformly in the system, $\rho(\mathbf{r})$ is constant and interaction energy is the only factor that contributes to the total free energy (F). In reality, the ordering transition depends on the competition between the ideal free energy which suppresses an ordering transition and the interaction energy which drives the system toward ordering. In addition, DFT indicates that in any hard-particle fluid, the phase diagram is only entropy related, which means it is temperature independent.

3.1.1.2 Simplified Onsager Theory for Ordering Transition of Rods

In 1925, Zocher noticed that phase separation occurs in the rod-like particles benzopurpurin 4B and chrysophenin suspension when the critical concentration is exceeded.[7] In 1949, Onsager[6] explained the phase separation of long spherical cylinder particles ($L >> D_{sc}$, L is the length and D_{sc} is the diameter of the cylinder) in theory, which actually agrees with equation 3.1. In the last two decades, the disordered-oriented transition (isotropic [I] phase- nematic [N] phase) of rod-like particle suspensions has been discussed theoretically[8-11] and experimentally.[12;13]

Two major theories attempt to explain the I-N transition. The Maier-Saupe theory[14] neglects variation of density and determines the I-N transition by calculating the free enthalpies of the phase; this also means the theory is appropriate for the thermotropic system where the I-N transition is driven by variations of temperature. It ignores the importance of short-range forces

and focuses only on long-range attraction.[15;16] On the other hand, Onsager's theory[6] is appropriate for lyotropic material. According to Onsager's calculation, the suspensions of the rod-like Tobacco Mosaic Virus (TMV) with length L and diameter D_{sc} ($L>>D_{sc}$) form an anisotropic phase at low concentration (2%).

In Onsager's theory, the Helmholtz free energy of the system at temperature T is:

$$\frac{\Delta F}{Nk_BT} = \frac{F(solution) - F(solvent)}{Nk_BT} = \frac{\mu^O(T,\mu_0)}{k_BT} - 1 + \ln c + \sigma(f) + bc\rho(f) \quad \text{equation 3.2}$$

where the concentration distributions of c^2 and higher orders are neglected, because for long rods, the $B_3 / B_2^2 << 1$ (B_3 and B_2 are the third and second virial coefficients). This simplification is only valid when $L / D_{sc} > 100$,[17;18] but Frenkel pointed out that reliable results may be received as long as $L / D_{sc} > 20$.[18] In equation 3.2, N is the number of rods in the solution; $\mu^O(T,\mu_0)$ is the standard chemical potential of rods at temperature T in the solvent with μ_0 chemical potential; $c = (N/V)$ is the number density; $b = (\pi/4)L^2 D_{sc}$ is the average excluded volume between two randomly oriented rods; and $\sigma(f)$ and $\rho(f)$ are the following functions of the orientation-distribution function $f(\Omega)$:

$$\sigma(f) = \int f(\Omega) \ln 4\pi f(\Omega) d\Omega \quad \text{equation 3.3}$$

$$\rho(f) = \frac{4}{\pi} \iint \sin\gamma(\Omega', \Omega) f(\Omega) f(\Omega') d\Omega d\Omega' \quad \text{equation 3.4}$$

where Ω is the solid angle that represents the orientation of the rods, $f(\Omega)$ is the possibility that a rod locates at angle Ω, and γ is the relative angle between two rods. So, it may be understood that $\sigma(f)$ is for an isolated particle, and $\rho(f)$ is associated with two particles. For one particle,

$$\int f(\Omega) d\Omega = 1$$

equation 3.2 can be transformed to equation 3.5 by setting the free energy to zero and applying equation 3.3 and 3.4

$$0 = C + \sigma(f) + bc\rho(f)$$

$$\ln 4\pi f(\Omega) = -C - bc\frac{8}{\pi}\int \sin(\gamma)(\Omega,\Omega')f(\Omega')d\Omega' \qquad \text{equation 3.5}$$

where $C = \dfrac{\mu^O(T,\mu_0)}{k_BT} - 1 + \ln c$ and $bc = (\pi/4)L^2 D_{sc}\dfrac{N}{V}$

In the isotropic phase, $\ln 4\pi f(\Omega) = 0$, so $f^0(\Omega) = (1/4\pi)$ is the solution for equation 3.5, regardless the value of "*bc*". Additionally, in the isotropic phase, $\sigma = 0$ and $\rho = 1$; therefore, the orientation-distribution-function part of the free energy includes component "$bcNk_BT$" (compare equations 3.2 and 3.5), whereas $\sigma > 0$ and $0 < \rho < 1$ in the uniaxial anisotropic phase (e.g., nematic phase). Kasyer[19] claimed that the I-N transition starts at $bc = 4$.

$$4 = bc = (\pi/4)L^2 D_{sc}\frac{N}{V} = \frac{L}{D_{sc}}\phi$$

$$\phi = 4\frac{D_{sc}}{L} \qquad \text{equation 3.6}$$

Equation 3.6 explains that a solution of long thin rods becomes unstable (starts to form anisotropic phase) at low concentrations.

Onsager's theory is valid only for a solution of rigid, monodispersed, thin rods. For a solution of semi-flexible rods, two more factors need to be considered: 1) the persistence length of the rods rather than the actual length should be applied; 2) the internal configurations need to be considered.[5;20] Khokhlov, *et al*., observed that the concentration needed for the isotropic-anisotropic transition was increased for the solution with flexible rods.[21;22] Lekkerkerker, *et al*., investigated the isotropic-anisotropic phase separation of the solutions of rods with different

length. Simulation results indicate the concentration of longer rods in the anisotropic phase is much higher than the concentration in the isotropic phase, and the longer rods are more likely aligned when mixed with shorter rods.[8] The Onsager's theory also fails to predict the ordering or demixing of binary mixture rods with two different diameters.[23;24]

Flory, *et al.,* studied the phase behaviors of rod-like polymers by using a modified lattice model. The intermolecular configuration, which is affected by the flexibility of the polymer chains, was considered.[25;26]

The scaled-particle theory (SPT) of hard rods was introduced in 1978.[27] This theory considers the third or higher virial coefficient, compared to the Onsager's theory. SPT is more accurate to treat solutions with higher concentration of rods or solutions of rods with lower a L/D_{sc} ratio. Besides the mixture of rods or spherically symmetric molecules, SPT is possibly appropriate to the mixture of hard-particles with simple various shapes by modifying some parameters.

3.1.1.3 Depletion Interaction between Spheres and Polymer

Two similar theories (excluded volume and entropy) are applied to explain the depletion interaction between two spheres. The excluded-volume theory was first introduced by Asakura and Oosawa (AO model)[28] in 1958 and was re-explored by Vrij in 1976.[29] According to the excluded-volume theory, in a sphere/polymer mixture, the spherical colloid with diameter D_{sp} is surrounded with an excluded shell. The thickness of the shell equals R_g of the polymer (Figure 3.1 a). When two colloids approach each other and the distance between the inside walls of the two colloids is shorter than 2 R_g of the surrounding polymer (Figure 3.1b), the depletion force of the polymer between the two colloids leads to the imbalance of osmotic pressure, and finally leads to the attraction of the colloids. The depletion is related to the R_g and the concentration of

the polymer. Entropy theory explains that the depletion-attraction occurs because the entropy of mixing decreases when the two colloids are very close to each other, but at the same time the accessible volume of the small polymers increases; and consequently the total entropy of polymers in the system rises. When the entropy gain is over the entropy lost, the whole system is stabilized by this "attraction through repulsion."

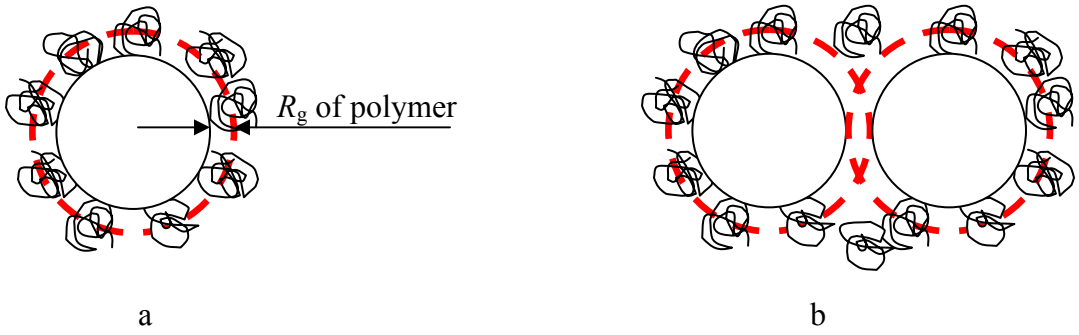

Figure 3.1 Scheme of mixture of spheres and polymers. a): One sphere is surrounded with polymers and the thickness of the excluded shell the equals the R_g of the polymer b): Two colloids approach each other and the distance between the inside walls of the two colloids is shorter than 2 R_g of surrounding polymers.

In the AO model, the polymer is treated as an ideal particle, so it is assumed there is no interaction between the polymer particles. Meanwhile, colloids react with each other through the hard-core-excluded volume repulsion.[28] In fact, increasing the concentration of polymers may affect intermolecular potential; also interpenetration between polymers and colloids, which decreases the depletion potential, may occur for large-size polymers. The range of attraction force, which is controlled by the size of the polymer, decides the phase behavior of colloid/polymer. For colloids with long-distance attraction, gas-liquid, gas-solid, and liquid-solid transitions are observed, while for colloids with short-distance attraction, only a gas-solid transition is observed. [30-32]

The phase behavior of a binary hard-sphere mixture is different from the behavior of rods. For a long time it was inaccurately thought that hard spheres are miscible regardless of their size and concentration.[33] Until 1991, Biben, *etc*., reported in theory that the phase separation happens when the size ratio S1/S2 is less than 0.2.[34] The "depletion potential" of a binary hard-sphere mixture is described as:[35]

$$\frac{W(h)}{k_B T} = -3\phi_s \frac{R}{\sigma}\left(1 - \frac{h}{\sigma}\right)^2 \qquad \text{equation 3.7}$$

where $W(h)$ is the depletion potential; k_B is the Boltzmann's constant; T is the absolute temperature; ϕ_s is the volume fraction of a small sphere; σ is the diameter of a small sphere; R is the radius of a large sphere and h is the distance between two large spheres. The depletion potential is zero when $h \geq \sigma$.

3.1.1.4 Depletion Interaction between Rods and Sphere

In addition to polymers and spheres, isotropic rods can be a very effective depletion agent, especially when $L << D_{sp}$ (L is length of rod, D_{sp} is diameter of sphere). The depletion potentials can be expressed as equation 3.8.[36]

$$\frac{W(h)}{k_B T} = -\frac{1}{3}\phi_{rod} \frac{L}{D_{rod}} \frac{D_{sp}}{D_{rod}}\left(1 - \frac{h}{L}\right)^3 \qquad \text{equation 3.8}$$

This is very similar as equation 3.7, which describes the depletion potential of two spheres. Nevertheless, in this equation, ϕ_{rod} is the volume fraction of rods; L is the length of the rod; D_{sp} is the diameter of the sphere; D_{rod} is the diameter of the rod; and h is the distance between two spheres. Lekkerkerker [36] studied the influence of the concentration of SiO_2-coated boehmite rods (L = 118 nm, D_{rod} = 13.9 nm) on the sedimentation ratio of SiO_2 spheres (D_{sp} = 700 nm). Phase separation was observed as expected, but the concentration of rods when two

phases start was lower than prediction from theory, and the addition of rods accelerated the phase separation. Dogic and Fraden[5] studied the mixture of *fd* rods (L = 0.9 μm, at 2 mg/ml) and various sizes of PS spheres. They observed that there is no phase separation when PS spheres are small (D_{sp} = 1 μm); crystallization occurs when the diameter of spheres increase to 1.5 μm. Phase separation in bulk happens when D_{sp} = 2 μm, at the same time the particles settle since they are too heavy. Equation 3.8 only shows the volume fraction of rods ϕ_{rod} affects the depletion potential. Experimentally the concentrations of both rods and spheres are the critical factors. Tracy, *et al*., studied mixtures of PBLG polymers and silica spheres in DMF.[37] They did not observe phase separation, probably because in their experiments the mixtures were at low concentrations. In 1999, Koenderink *et al*. [35] reported depletion-induced crystallization in the rod/sphere mixture. They confirmed that a certain concentration of rods and spheres is necessary in order to get depletion attraction and that increased concentration of both rods and sphere can speed the crystallization procedure. They also illustrated that the increased viscosity may drag back the depletion action at high concentrations. Figure 3.2 is a picture of SiO_2-coated boehmite rods (L = 230 ± 90nm, D_{rod} = 9 ± 2 nm) (Figure 3.2a) and the mixture of the rods and SiO_2 spheres (D_{sp}= 740 nm) (Figure 3.2b) in DMF with 0.001M LiCl.

All the examples shown above are the cases of a mixture of rods and large spheres. Small spheres also induce phase separation in a rod/sphere mixture as well. Surprisingly, a layered phase, instead of bulk demixing, is observed in the solution.[12;38] Fraden, *et al.*, studied phase behavior of a mixture of *fd* virus rods and PS spheres theoretically, experimentally, and by computer simulation. The *fd* rods had a contour length of 880 nm, a persistence length of 2.2 μm, and a diameter of 6.6 nm. The PS spheres used had various diameters from 22 nm to 1.0 μm. At certain concentration, PS spheres in a range of 60-120 nm (diameter) are able to form a columnar

phase; while to form a lamellar phase, PS spheres have to be in the range of 22-120 nm. Smaller spheres need higher concentration.

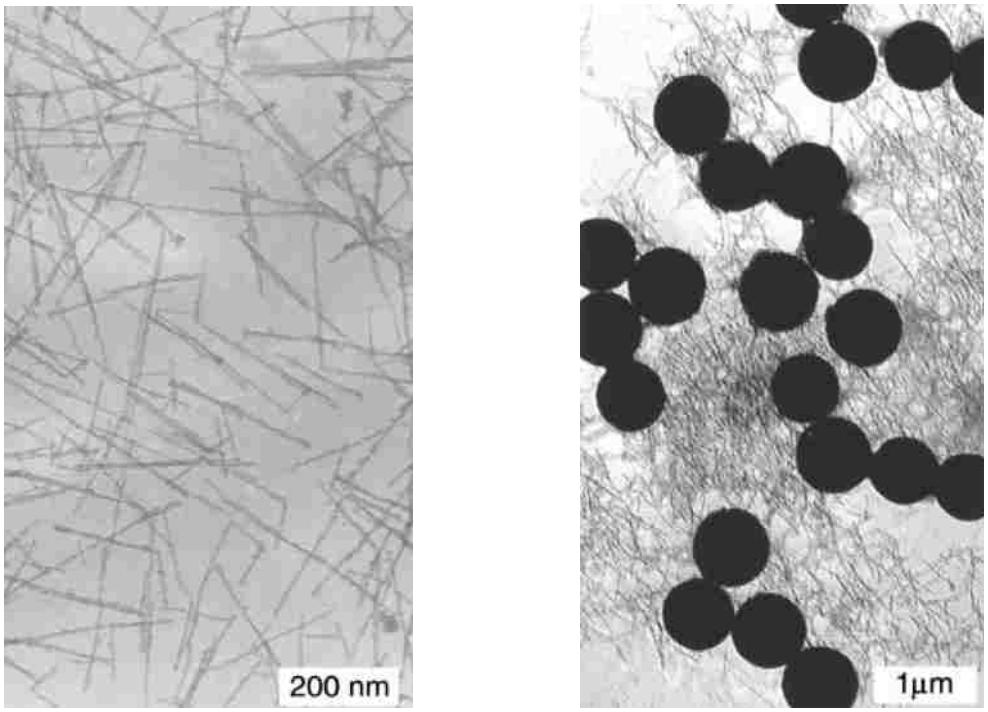

a b

Figure 3.2 EM pictures of SiO_2-coated boehmite rods and the mixture of boehmite rods and SiO_2 spheres. a) EM picture of SiO_2-coated boehmite rods (L = 230 ± 90nm, D_{rod} = 9 ± 2 nm). b) EM picture of the mixture of SiO_2-coated boehmite rods and SiO_2 spheres (D_{sp}= 740 nm). Both are in DMF with 0.001M LiCl. (Copied from Ref. 35)

Figure 3.3 has the photographs (by using differential interference microscopy) and diagram of *fd*/PS (D_{sp}=100 nm) mixture with columns and lamellar. Figure 3.4 illustrates the excluded volume of rod/sphere mixtures in (a) nematic, (b) layered phase and (c) immiscible phase. The grey areas represent the excluded volume. One can see that the excluded volume reaches a minimum in the layered phase. In addition, theoretically, the layered phase is more stable with larger ratio of the length of rods (L) to the size of sphere (D_{sp}).

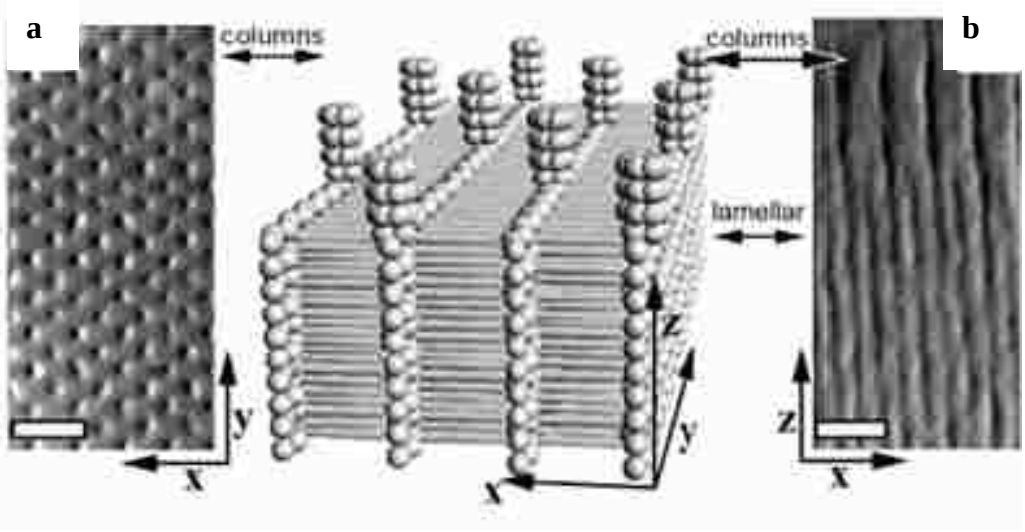

Figure 3.3 Photographs and diagram of *fd* (rods)/PS (spheres) mixture. The scale bars are 3 μm. a) and b) are orthogonal sections of co-existing columnar and lamellar phases. (Copied from Ref. 12)

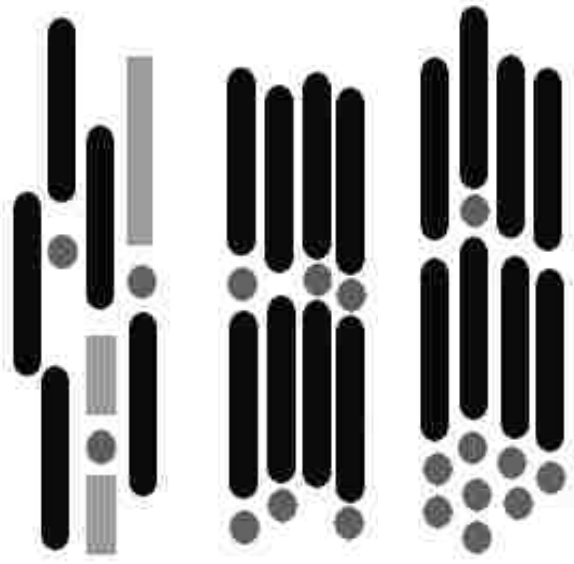

a) b) c)

Figure 3.4 Scheme of excluded volume effect. a) in nematic, b) in layered and c) in immiscible phase which has rod-rich and sphere-rich phases.(Adapted from Ref. 38)

3.1.2 Probe Diffusion

3.1.2.1 Categorization of Diffusion Coefficients

Diffusion of polymer in a complex solution is considered as a key issue in many areas such as biology, coating and polymer industries. [39-43] A number of theoretical and experimental studies have been performed in past decades.[44-47] For the solution which has only one molecular species besides solvent, two kinds of diffusion are generally mentioned: mutual diffusion and self diffusion.

Mutual diffusion refers to the gradients of concentration. It can be defined as Fick's first law: [48;49] (the development below follows Ref.49)

$$J = D_m(\nabla c) \qquad \text{equation 3.9}$$

where J is the diffusion current (flux), (∇c) describes concentration gradient, and the concentration c is chemical-potential dependent. In a binary solution (subscript 1 represents solvent, and subscript 2 represents solute) the chemical potential gradient is:

$$-\nabla\mu_1 = f_{12}\left(\frac{c_2}{c_1}J_1 - J_2\right) \qquad \text{equation 3.10}$$

where f_{12} is the friction coefficient between the two components; μ_1 is chemical potential of solvent. In a volume-conserving system,

$$J_1\upsilon_1 + J_2\upsilon_2 = 0 \qquad \text{equation 3.11}$$

where υ is the partial molar volume. The system is also mass conservative, so

$$\sum_i c_i\upsilon_i = 1 \qquad \text{equation 3.12}$$

Then by eliminating J_1 in equation 3.10, equation 3.13 is obtained

$$J_2 = \frac{c_1\upsilon_1}{f_{12}}\nabla\mu_1 \qquad \text{equation 3.13}$$

The chemical potential of a solvent can be presented in terms of osmotic pressure:

$$\mu_1 - \mu_1^0 = -\upsilon_1 \pi = -RT\upsilon_1 (c_2 + A_2 c_2^2 + ...) \qquad \text{equation 3.14}$$

where π is osmotic pressure; A_2 is the second virial coefficient (in Onsager's theory, the virial coefficient is normally presented as B).

One can get equation 3.15 by using equation 3.12, 3.13 and 3.14

$$J_2 = -\frac{RT(1-c_2\upsilon_2)^2}{f_{12}c_1}(1 + 2A_2 c_2 + ...)\nabla c_2 \qquad \text{equation 3.15}$$

With equation 3.9, and 3.15, we obtain

$$D_m = \frac{RT(1-c_2\upsilon_2)^2}{f}(1 + 2A_2 c_2 + ...) \qquad \text{equation 3.16}$$

where $f = f_{12}c_1$ is the molar hydrodynamic friction coefficient of the solute.

Compared with mutual diffusion, self diffusion is more easily understood. One can get the diffusion coefficient of the a particle with the Brownian motion by measuring the probability $f(x,t)$ that the particle appears at x (location) from time t to $(t + \tau)$. The possibility follows the Gaussian distribution (equation 3.17)

$$f(x,t) = \frac{n}{\sqrt{4\pi D_s t}} \exp(-\frac{x^2}{4D_s t}) \qquad \text{equation 3.17 [50]}$$

where n is the number density of particles and D_s is the self diffusion coefficient. On the other hand, it can be explained that one can measure the diffusion speed of a particle by testing how far the particle can travel during a time interval τ. The random motion of a particle can be described as equation 3.18:

$$\left\langle \left| \mathbf{r}(t+\tau) - \mathbf{r}(t) \right|^2 \right\rangle = 2d_{men} D_s \tau \qquad \text{equation 3.18}$$

$\left\langle \left|\mathbf{r}(t+\tau)-\mathbf{r}(t)\right|^2 \right\rangle$ is the mean squared dislocation of a particle from time t to $(t + \tau)$, d_{men} is the number of dimensions of the diffusion, e.g., in two dimensions, equation 3.18 can be simplified as

$$\left\langle \mathbf{r}^2 \right\rangle = 4D_s\tau \qquad \text{equation 3.19}$$

Instead of the traditional concentration-gradient method, with the help of a correlator, quasi-elastic light scattering spectroscopy (QELSS), which is also known as photon correlation spectroscopy (PCS) or dynamic light scattering (DLS), is widely used to determine the mutual diffusion coefficient. Because of the high spatial coherence of a laser,[51] a "speckle pattern" is present in the solution illuminated by a laser beam. The movement of particles in the solution causes the intensity fluctuation of the speckle pattern. The fluctuation is measured by an autocorrelation function that is related to an electric field autocorrelation function (equation 3.20).

$$g^{(1)}(t) = e^{-\Gamma t} \qquad \text{equation 3.20}$$

where $g^{(1)}(t)$ is the electric-field autocorrelation function; Γ is the decay rate that is reciprocal of decay time τ. D_m can be obtained by using equation 3.21, and here q is the scattering vector, which is defined as equation 3.22.

$$\Gamma = q^2 D_m \qquad \text{equation 3.21}$$

$$q = \frac{4n\pi \sin(\theta/2)}{\lambda_0} \qquad \text{equation 3.22}$$

where n is the refractive index of solvent, θ is the scattering angle, and λ_0 is the wavelength of the incident laser.

Pulsed-field-gradient nuclear magnetic resonance (PFGNMR) is one of the standard techniques to measure the self diffusion of a particle.[52-54] PFGNMR determines the diffusion by measuring the attenuation of a spin echo signal, which corresponds to the combination of the translational motion of the spins and the displacement of gradient pulses.[55] Diffusion-ordered spectroscopy (DOSY) NMR is based on the PFGNMR experiment. A DOSY NMR spectrum (2D) is generated (one axis is for the chemical shift and another axis is for the diffusion coefficient) by separating the PFGNMR signal according to the diffusion coefficient of each component.[56;57] The probe diffusion coefficient D_p is usually mentioned in a ternary system, which has a solvent, background polymers called the matrix, and the probe particles that are the subjective of interest. Normally, the concentration of probes is dilute and the concentration of the matrix varies. QELSS can measure the probe diffusion under either of the following two situations: 1) the polymer matrix has identical refractive index as solvent (only probe particles scatter light) or 2) the refractive index of matrix is very close to that of the solvent (the probe particles dominate the scattering of the solution).[58;59]

Fluorescence photo-bleaching recovery (FPR) [60-62] (it is also called fluorescence recovery after photo bleaching (FRAP)) and fluorescence correlation spectroscopy (FCS) are available to detect the diffusion of probe if the probe molecules can be “labeled”, which actually means chemically bonded with fluorescent groups. FPR has three steps, which are described in Figure3.5. First, the fluorescence of a chosen area of the sample is excited and measured with a weak beam. Second, some fluorescent moieties in the area are bleached /destroyed by a strong beam, which is about 2000 times more intense than the weak beam. Finally the fluorescence is recovered in the selected region because the unbleached molecules, which are limited outside the selected region, can diffuse to this region.

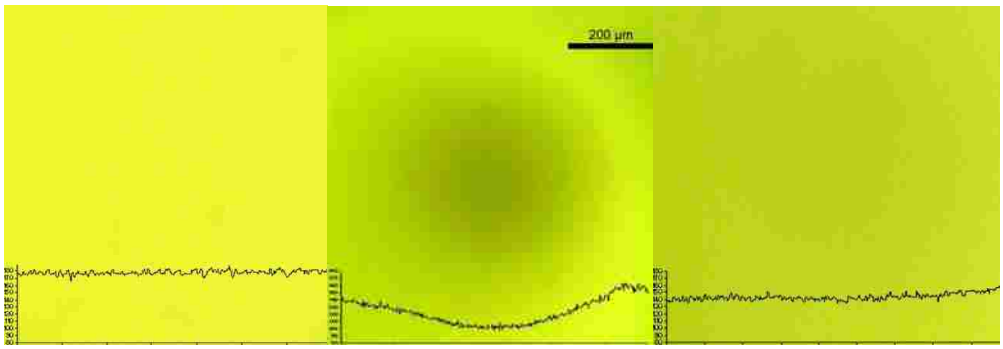

Figure 3.5 Three steps in the FPR process Left: Epifluorescence image acquired with 40× objective. Middle: after 10 minutes illumination, a spot has been bleached in the pattern, now taken with 10× objective. Right: recovery is almost complete after 30 minutes (still 10× objective). Traces show intensity across the middle of the image.

First introduced by Magde, etc., in the early 1970s,[63] FCS has been developed into a powerful tool to determine the diffusion coefficient in solution.[62-64] FCS measures the fluctuation of a fluorescent signal in image volume. (Figure 3.6)

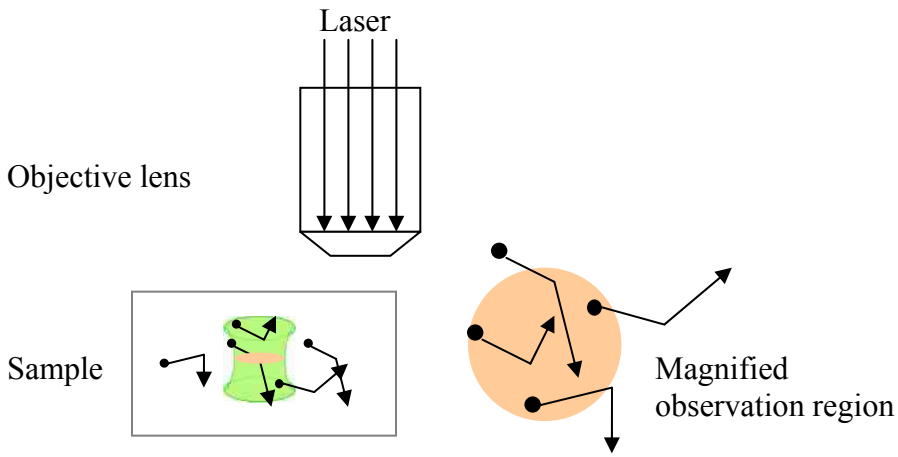

Figure 3.6 Scheme of FCS. The black dots are sample particles. The green part is the focal volume where the sample particles are illuminated by laser. The observation volume (peach-colored part) is the space where the fluorescent particles are detected. (Adapted from Ref. 65)

A selective photosensitive molecule, which changes its refractive index when it absorbs light from a incident beam, is used for forced rayleigh scattering (FRS).[66] Two intense coherent

laser beams generate a interference pattern, which produces reflective index grating, in sample solution. A weak probe beam is then applied to monitor the relaxation of the refractive index grating.

Generally, if the probe is distinguished from matrix polymer in molecular structure or molecular weight besides dye attachment, the diffusion coefficient measured is the *probe diffusion coefficient*. In some cases when the probe and matrix have the same monomer but a different molecular weight, one still defines the coefficient measured as a probe diffusion coefficient.[67] In the system that the probe and matrix are identical polymers except for the presence of "label", the diffusion determined is the *self diffusion coefficient*.[68;69] In a ternary system, which the two polymer components are concentrated, the diffusion characterized is called *interdiffusion* or *cooperative diffusion*.

3.1.2.2 Diffusion of Probe in Matrix Polymer Solution

QELSS has been widely used to determine the diffusion coefficient of a probe in solution, in which the matrix polymer has a matching refractive index as solvent. Tuner and Hallett measured the diffusion of PS latex (PSL) through dextran;[70] while Phillies's group studied the PSL diffusion in the water solution of Hydroxypropylcellulose (HPC).[71-73] Cush *et al.,* investigated the probe diffusion in a dextran aqueous solution by using TMV as a probe, and both translational and rotational diffusion coefficients were measured.[74;75] Hanly, *et al*., [76] and Lodge[77] measured the diffusion of linear polystyrene (PS) through Poly(methyl vinyl ether) (PMVE) in isorefractive solvent *o*-fluorotoluene (oFT), while Martin used toluene as a matching refractive index solvent for PMVE.[78;79] Daivis, *et al*., [80] compared the diffusion of PS through the PMVE matrix in toluene and CCl_4. Surprisingly, the diffusion coefficient of probe PS in CCl_4 is much lower than that in toluene. The true diffusion was not measured, probably because CCl_4 is

a good solvent for PMVE but only a marginal solvent for PS. Diffusion of the dextran probe in the semidilute range ($c > c^*$, the definition of c^* is at section 3.1.2.3) of a water solution, which has polyvinypyrolidone as matrix, was measured by Desbrieres and his coworkers.[46] Three relaxation modes were observed, and the slowest one was the consequence of aggregate formation. As mentioned above, the probe and matrix can be polymers with the same monomer but different M_w. Davis measured the diffusion of high M_w dextran (probe, M_w=864,000) through low M_w dextran (matrix, M_w=20,400) in water. Two distinct modes of decay were observed, and it is believed the fast mode corresponds to the diffusion of the matrix polymer (low M_w dextran) and the slow mode is from the probe polymer (high M_w dextran).[67] A similar two-decay mode was also observed in two different M_w (M_{w1}=7,060,000; M_{w2}=964,000) PS / toluene solutions.[81] The Pecora group investigated the rods/spheres composite, which has SiO_2-coated spheres (probe) and rod-like polymers poly (benzyl glutamate) (matrix). In their experiments, DMF or DMF/pyridine mixture was used as a solvent. They believed that 1) PBLG rods form a network when they are concentrated enough, therefore the solution should be considered as a net with holes instead of a continuum; 2) the network causes local viscosity surrounding the spheres (microviscosity (η_μ)) decreasing to only about half of the viscosity of solution (η), which consequently lets the spheres diffuse faster than expected.[59;82]

By using PFGNMR, Brown and Stilbs investigated the diffusion coefficients of three molecular weights poly (ethylene oxide) (PEO) (probe, M_W = 73,000, 250,000 and 1,200,000) in aqueous solution of three molecular weights of dextran (matrix, M_W = 20,000, 100,000 and 1,200,000). It was observed that the D_p/D_o (D_o is the diffusion coefficient in the solution that is infinitely dilute) depends on the matrix molecular weight but not the size of probe.[83] The PEO in aqueous solution of ethyl hydroxyethyl cellulose was studied by Nyden, *el at*., more complicated

diffusion behaviors were observed in the solution with a large matrix polymer.[84] Russo's group investigated the diffusion of FITC-labeled bovine serum albumin (BSA) in a DNA solution with salt by using FPR. The diffusion coefficient as a function of concentration of both DNA matrix and added salt was studied.[85]

Many studies have been completed to compare diffusion-measurements by using different techniques. Cong, *et al*., compared the diffusion-coefficients of labeled Napps (M_w = 100,000 or M_w = 680,000) in an aqueous solution of unlabeled Napps (M_w = 990,000) with salt by using DLS and FPR. The effect of the molecular weight of the probe was observed.[86] Daivis and Pinder studied the diffusion measurements of PS (probe)/ poly (vinyl methyl ether) (PVME) (matrix)/ toluene by using DLS and PFGNMR. Their results indicate that within experimental error, the diffusion coefficient obtained by DLS is equal to the result from PFGNMR. [87] Chang and Han studied ternary solutions, PS (probe)/ PVME (matrix)/o-fluorotoluene by using DLS and FRS. The results from DLS and FPS are reasonably close, but these two techniques have a distinctly different length scale. For DLS, the length scale is 30 nm $< q^{-1} <$ 100 nm, while for FRS, the scale is 1μm $< q^{-1} <$ 2.5 μm.[88] Tinland and Borsali compared the diffusion-measurements by using FRAP and DLS. The diffusion-behaviors of fluorescently labeled dextran through polyvinypyrolidone with varied concentrations (from very dilute to semidilute, 0.1-10c^*) were studied. The results indicate that the values of D_p from these two methods do agree in the semidilute regime, but the agreement becomes less apparent with decreasing concentration.[89] Scalettar, *et al*., measured the mutual diffusion and probe diffusion of phase λ DNA by using FRAP and FCS. Ethidium monoazide, which bonded with DNA covalently, was used for FPR experiments; and ethidium bromide, which bonded with DNA noncovalently, was used for FCS experiments. It was observed that D_m increased but D_s decreased with increased

concentration (from 17 μg/ml to 305 μg/ml). This is possibly because in this concentrated solution the average volume λ DNA occupied is the same or larger than the inter-DNA spacing and molecules can disturb each other. The hard-core interaction pushes molecules away from each other and accelerates their movement; therefore, D_m increases with a higher concentration. On the other hand, the random motion of molecules are restrained by neighbor particles, so D_s decreases with increased concentration.[62]

3.1.2.3 Two Theoretical Models

Two models are usually used to describe the dependence of D_p, D_s with the molecular weight of the matrix polymer (M), the molecular weight of probe (P), and the concentration of matrix polymer c.

1) Scaling-law model[90]

$$D_s = D_1 M^{\gamma} c^{-x} \qquad \text{equation 3.23}$$

where the D_1 is a scaling prefactor and γ and x are scaling exponents. A transition between the dilute and semidilute regime is suggested in this model, and there are two major transition concentrations: overlap concentration c^* ($c^* = N/V$ at which $(3/4)\pi R_g^3 N/V = 1$, N is number of macromolecules, V and R_g are the volume of the solution and radius of gyration of macromolecules, respectively) and entanglement concentration c_e.

2) Exponential model[91;92]

$$D_s = D_0 \exp(-\alpha c^{\nu}) \qquad \text{equation 3.24}$$

where α is a scaling prefactor and ν is a scaling exponent. Equation 3.24 can be elaborated for probe diffusion as stretched exponential form (equation 3.25)

$$D_p = D_0 P^{-a} \exp(-\alpha c^{\nu} P^{\gamma} M^{\delta}) \qquad \text{equation 3.25}$$

where a, γ and δ are additional scaling exponents.

For most random-coil polymers, dependences of D_s and D_p upon c follow the exponential model (equation 3.24 and 3.25), and when $P >> M$ or $M >> P$, there is molecular weight dependent deviation.[93] Tao and Lodge reported that the data of hydrogenated polybutadiene (hPB)/alkane solution fitted the scaling model very well.[94]

Polymer topology also affects diffusion. Chen noticed that in the CCl_4 solution of linear or star polyisoprenes, star polymers diffused significantly faster than linear polymers with same molecular weight.[95] Ernst, *et al*., observed the star polymers, which had the same number of arms (*f*) with a higher molecular weight, tended to diffuse slower. The tendency was also noticed for star polymers with an increased number of arms, each having the same molecular weight ($M_{arm} \approx 10{,}000$).[96;97] Pecora, *et al.,* measured the diffusion of linear polystyrene from 25 ^{o}C to 75 ^{o}C through matrix poly(n-hexyl isocyanate) in solvent 1,1,2,2-tetracholoethane (as isorefractive solvent at 75 ^{o}C) or toluene (as isorefractive solvent at lower temperature). It is believed that besides the concentration of the polymer matrix, the flexibility (end-to-end distance) of the matrix polymer also affects the diffusion of the PS probe.[98]

3.2 Experiments

3.2.1 Sample Preparation

3.2.1.1 PCBL in *m*-Cresol

PCBL polypeptides with a molecular weight of 480,000 were dissolved in *m*-cresol. Samples with 1 wt % were used for optical rotation measurements at room temperature. High-concentration samples (15-25 wt %) were investigated with cross-polarized microscopy experiments at a temperature range of 21-29 ^{o}C.

3.2.1.2 SiPCPs and PBLG in Pyridine

Dilute PBLG/pyridine samples were prepared by dissolving PBLG with molecular weight 277,000 in pyridine. High-concentration PBLG/pyridine or SiPCPs/pyridine samples were made by concentrating the diluted sample with a vague flow of dried, filtered N_2. The samples were vibrated with a vortex mixer once per 10-15 minutes to homogenize the samples (avoid the dry area on the surface). The final concentrations were calculated by weight.

3.2.1.3 Mixture of SiPCPs and PBLG for Cross-Polarized Microscopy

Dilute PBLG/pyridine and SiPCPs/pyridine were mixed together with the desired SiPCP / PBLG ratio. The mixtures were then concentrated with a vague flow of dried / filtered N_2 to the expected concentration. The samples were vibrated with a vortex mixer once per 10-15 minutes to homogenize the samples. The final concentrations were calculated by weight.

3.2.1.4 Mixture of Labeled SiPCPs and PBLG for Epifluorescence Microscopy

Fluorescein isothiocyanate (FITC)-labeled SiPCPs were used for epifluorescence microscopy experiments. FITC was dissolved in acetone, and then the FITC/acetone solution was mixed with an SiPCPs dichloromethane suspension. The mixture was stirred constantly for 1-2 days before being centrifuged and washed to remove the free dye. Then the FITC-labeled SiPCPs were dispersed in pyridine and used like regular SiPCPs to prepare the SiPCPs/PBLG samples as 3.2.1.3 describes. All samples for microscopy experiments were located in Vitrocom cells with sealed ends or put on microscope slides, which were covered with cover slides and then sealed with vacuum grease.

3.2.1.5 Temperature-Control System

A Mettler FP 80 central processor temperature control system was used to control the temperature for cross-polarized microscopy experiments of PCBL/*m*-cresol solution. The system

was air cooling, and the experiments were performed in the temperature range from 15 °C to 35 °C.

3.2.2 Characterization Techniques

3.2.2.1 Optical Rotatory Dispersion (ORD)

A JASCO Polarimeter DIP-370 was used to measure the optical rotation of PCBL in *m*-cresol. The measurements were performed in a temperature range of 20-30 ^{o}C at wavelength 589 nm.

3.2.2.2 Cross-Polarized Microscopy

An Olympus polarizing microscope (model BHA) was used to visualize the crystal structures of PCBL in *m*-cresol, PBLG, SiPCPs, or their mixtures in pyridine at room temperature.

3.2.2.3 Epifluorescence Microscopy

The crystal structures of FITC-labeled SiPCPs and PBLG mixtures were characterized by using epifluorescence microscopy at room temperature. The experiments were performed by using an Olympus polarizing microscope (the same one as in section 3.2.2.2) except the mercury lamp and blue-light wavelength filter were applied.

3.2.2.4 Fluorescence Photobleaching Recovery

The FPR was used to measure the diffusion coefficients of FITC-labeled SiPCPs through a PBLG matrix. The samples were located in Vitrocom cells, both ends of which were sealed to avoid moisture in air. All experiments were performed at 20 ^{o}C, and the data were collected by Labview software (edition 3.0.1). The collected data were analyzed by fitting to an exponential function (ANSCAN program). The details of the instrument are described in section 4.1 (Ronchi Ruling (RR) FPR).

3.2.2.5 Static Light Scattering

SLS was used to measure the scattering intensity of SiPCPs or PBLG in pyridine. The technique has been outlined in section 2.2.3.2.

3.2.2.6 Dynamic Light Scattering

DLS was used to measure the diffusion coefficients of FITC labeled SiPCPs in pyridine. The technique has been outlined in section 2.2.3.1.

3.3 Results and Discussion

Two categories of samples (PCBL in *m*-cresol and PBLG, PBLG-grafted SiPCPs, or their mixtures in pyridine) were studied. For PCBL/*m*-cresol samples, the optical rotation dispersion and dependence of crystal structures with temperature were studied. For PBLG, PBLG-SiPCPs or their mixtures (in pyridine), the phase behaviors were explored at relatively high concentrations (> 5 wt % for both PBLG and SiPCPs); and at relatively low concentrations, probe diffusions of FITC-SiPCPs (≈ 0.25 wt %) in PBLG matrix (varied from 0– 2 wt%) were investigated.

3.3.1 PCBL in *m*-Cresol (With the help of Amanda Steffens)

Fujita and coworkers studied the coil-helix transition of PCBL in *m*-cresol by using several techniques, such as optical rotation dispersion (ORD), viscosity, heat capacity, and dielectric dispersion. A sharp transition around 27 ^{o}C was observed.[99-101] The helix-coil transition affects the crystal structure of PCBL in solution because only a polymer chain with helical conformation can form an ordered crystal structure, while a random coil chain is expected to form an isotropic phase. In this part, the transition temperature of PCBL with molecular weight 480,000 in *m*-cresol was determined first, and then the dependence of the crystal structures with temperature was investigated.

3.3.1.1 The Coil-Helix Transition of PCBL in *m*-Cresol

Figure 3.7 is the optical rotation measurements of PCBL with molecular weight 480,000 in *m*-cresol in a temperature range of 21-29 ^{o}C. Previous studies in this group by Sibel Turksen-Selcuk[102] showed similar results of optical rotation of Co-SiO_2-PCBL with different wavelengths, so here we only measured the optical rotation at wavelength 589 nm instead of doing wavelength-dependent ORD. One can see that the helix-coil inverse transition occurs at around 26-27 ^{o}C which is very close to the result reported by Fujita's group.

3.3.1.2 The Crystal Structures of PCBL in *m*-Cresol

As explained above, helical conformation is required to form a liquid crystalline structure, but concentration is another factor that affects the crystalline formation. Figure 3.8, 3.9, and 3.10 are the pictures of two concentrations of PCBL (M_w=480,000) / *m*-cresol solution at 35 ^{o}C on 1st day, 4th day, or 5th day.

From Figure 3.8-3.10, one can see the finger-print-pattern crystalline structures which are known for the cholesteric solution were formed in both low- and high-concentration samples. For the 25 wt% sample, it took less than one day to generate the crystal structures, while for the 15 wt% sample, there was no sign of the finger-print-banding until the 5th day.

The samples were then cooled down to room temperature, which was lower than the helix-coil transition temperature in dilute solution. As the PCBL chains were supposed to be random coil status, isotropic structures might have been expected. Surprisingly, after two weeks, some anisotropic structures were still observed. Figure 3.11 and 3.12 are the pictures of 25 wt% and 15 wt % samples (same samples as Figures 3.8 and 3.9) two weeks after they were cooled down to room temperature.

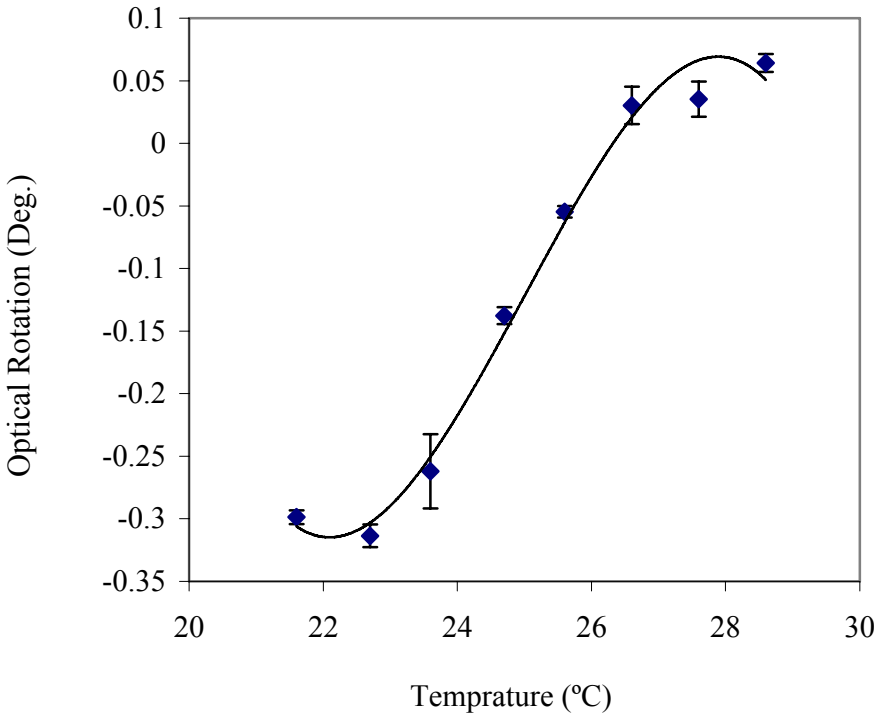

Figure 3.7 The optical rotation at λ = 589 nm of PCBL (M_w = 480,000) *vs*. temperature in *m*-cresol.

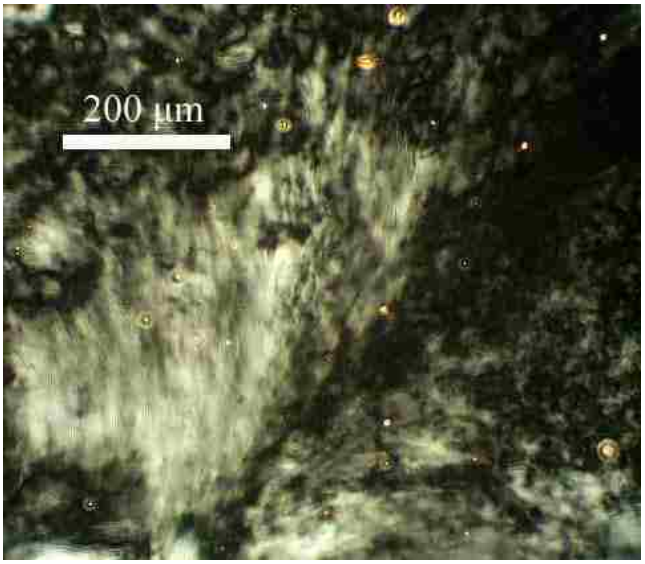

Figure 3.8 Photomicrograph of 25 wt% PCBL/*m*-cresol at 35 °C, first day. (The yellow dots are probably bubbles or dried spots.)

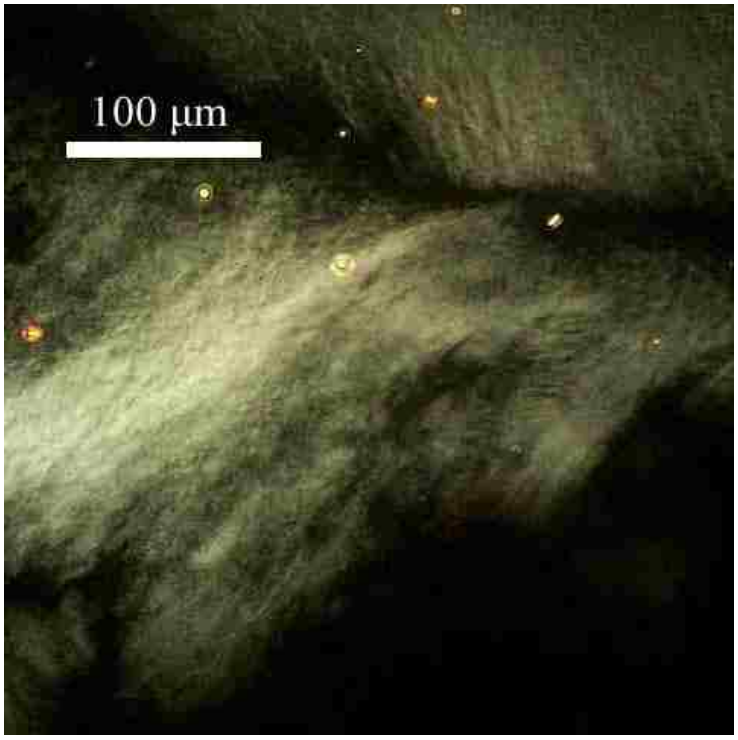

Figure 3.9 Photomicrograph of 15 wt% PCBL/*m*-cresol at 35 °C, fourth day. (The yellow dots are probably bubbles or dried spots.)

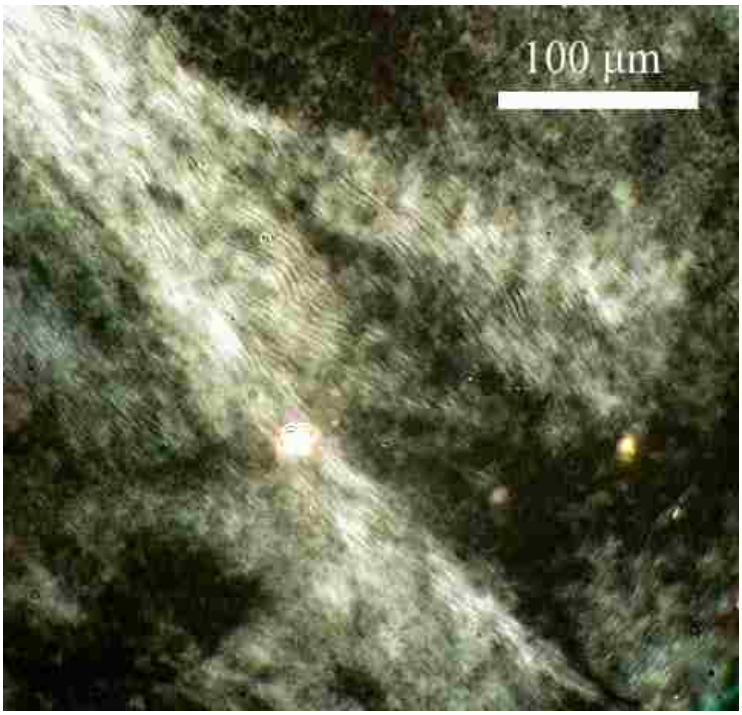

Figure 3.10 Photomicrograph of 15 wt% PCBL/*m*-cresol at 35 °C, fifth day.

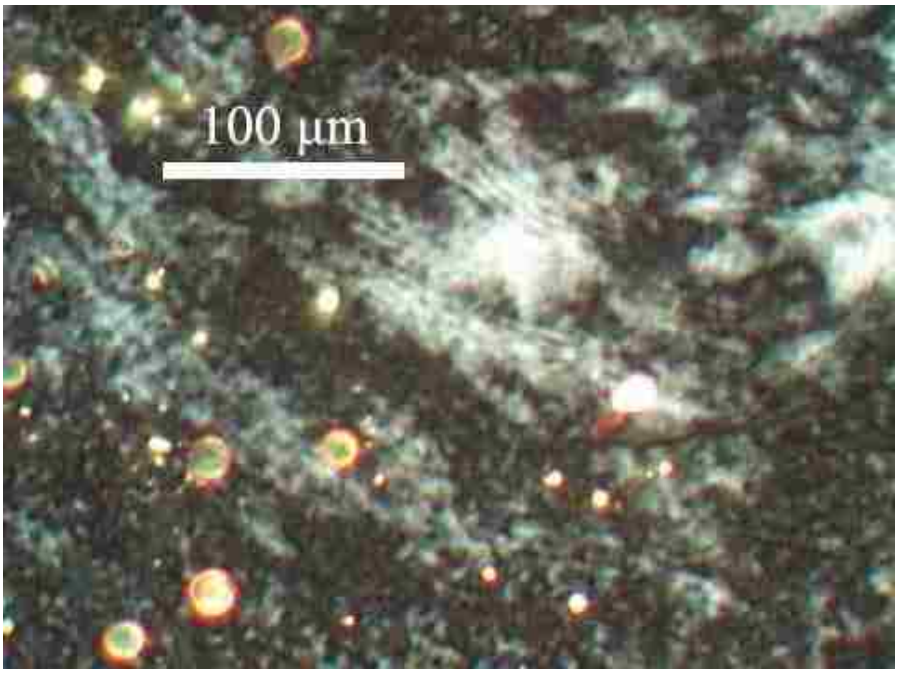

Figure 3.11 Photomicrograph of 25 wt% PCBL/*m*-cresol, two weeks after it was cooled to room temperature. (The yellow dots are probably bubbles or dried spots.)

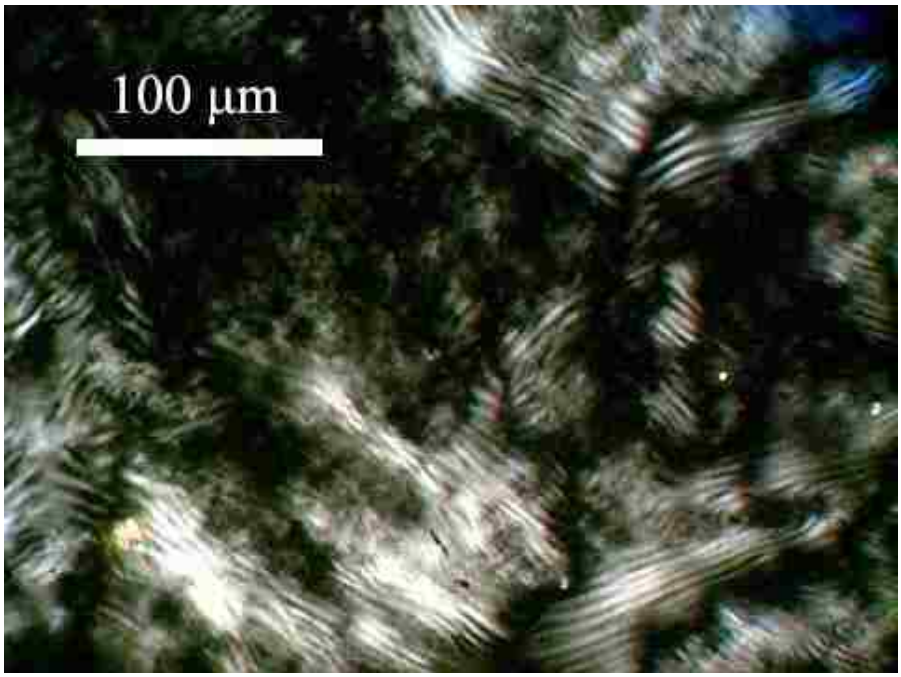

Figure 3.12 Photomicrograph of 15 wt% PCBL/*m*-cresol, two weeks after it was cooled to room temperature.

As Figures 3.11 and 3.12 display, two weeks after the samples were cooled, the area of finger-print bands slowly grew smaller, which indicates the diminishment of the crystalline composition and some crystalline structures still existed probably because of the high molecular weight of the PCBL. It was also observed that more crystalline structures were "frozen" in a 15 wt % sample than in a 25 wt% sample by comparing Figures 3.11 and 3.12. Probably there is competition between hydrogen bonding and crystal formation; and the higher concentration, possibly more crystal formations will disturb the hydrogen-bond network. There are some odd bright yellow dots on pictures 3.8, 3.9 and 3.11. We consider they are bubbles or dried spots.

3.3.2 PBLG and PBLG SiPCPs in Pyridine

3.3.2.1 Crystal Structure of PBLG

Compared to the formation of the PCBL liquid crystal, which is affected by temperature, PBLG is lyotropic, in which liquid crystal formation mostly depends on concentration such as TMV and DNA. These rod-like polymers can form a liquid crystalline structure at a high concentration [103-107] or by mixing with some other flexible polymer[108] at lower concentration. In this part, all samples were prepared and examined under room temperature. We observed that the PBLG started to form liquid crystal when the concentration was over 12 wt%. Figure 3.13 is the picture of PBLG in pyridine at 20.24 wt%. The clear "finger print lines" confirm the cholesteric nature of this liquid crystal, which is expected for PBLG in a good solvent. The width of a pair of neighboring bright and dark lines corresponds to the half turn of the PBLG cholesteric helix, $P/2$ (P is called pitch). Figure 3.14 is the scheme of the cholesteric pitch.

The pitch is normally several tens of micrometers. Robinson, *et al*. observed that the pitch P of PBLG depends on the concentration (higher concentration cholesteric sample has smaller pitch) and the solvent but barely on the molecular weight of PBLG.[109;110] Uematsu

studied the temperature effects on pitch of PBLG in a mixture of dioxane and dichloroethylene, and observed that the pitch increased with a raised temperature until the cholesteric superhelix switched from right hand to left hand and then the pitch decreased.[111]

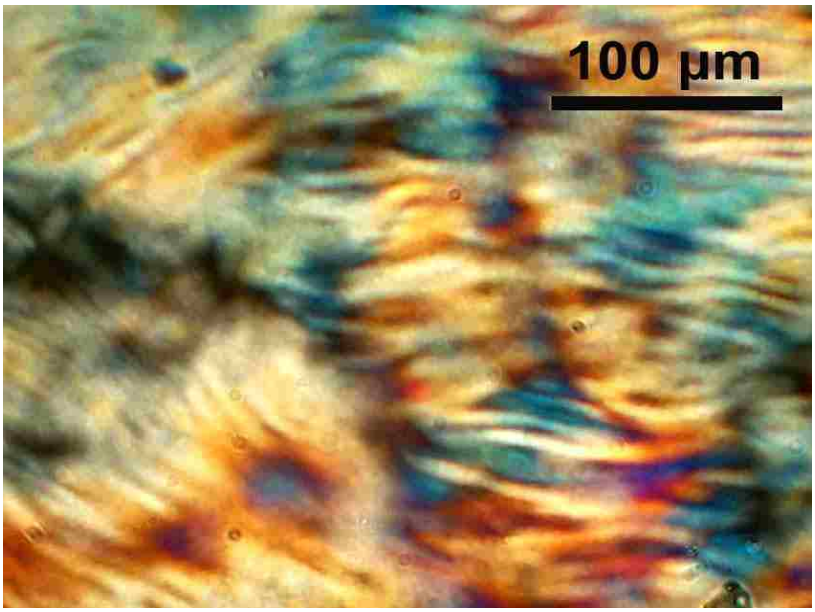

Figure 3.13 Photomicrograph of PBLG (M_w = 277,000) in pyridine at 20.24 wt % at room temperature.

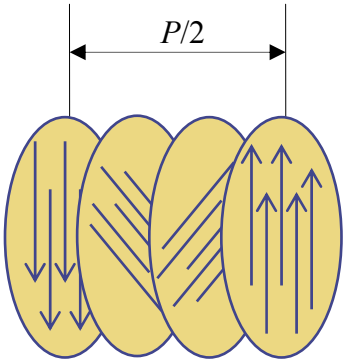

Figure 3.14 Scheme of cholesteric pitch. (Only half turn is shown.)

According to Onsager's theory, the isotropic–nematic transition starts when $\phi = 4\frac{D_{sc}}{L}$, so one can calculate that the volume fraction needed for I-N transition is about 3.4 %, equivalent to 4.3 wt% for PBLG with M_w = 277,000. According to the Flory's prediction[25;26;112], in which the starting point (also called A points) is $\phi_A = (8/x)(1-2/x)$ ($x = L/D_{sc}$), the I-N transition occurs at about $\phi_A = 6.6$ %, corresponding to 8.4 wt %. Bu, *et al.*, compared the experimental results and theoretical expectations of the I-N transition point of PBLG with different M_w in pyridine.[113] It was observed that for low M_w PBLG ($x >\approx 50$, corresponding to M_w = 116,800), Onsager's prediction is closer to the experimental result. The deviation between theories and our results is probably because the high-molecular weight PBLG used has a long semi-flexible polymer chain.

3.3.2.2 Crystal Structure of SiPCPs

It is possible to see the anisotropic structure of SiPCPs at relatively high concentrations. The crystal structure of SiPCPs starts when the concentration is around 43 wt%. A photomicrograph of SiPCPs in pyridine at 43.87 wt% appears as Figure 3.15.

In this case, the finger-print structure is still visible, but seems to be superposed on a globular structure. The vivid colors of slightly smaller colloidal crystalline SiPCPs made with a PCBL shell,[114] when dispersed in DMF, are not visible. One can see the banding is shorter (about 20-30 μm) compared to the one in liquid structures of PBLG/pyridine (around 60-100 μm). In addition, the pitch looks narrower compared to the photomicrograph of PBLG (Figure 3.13). The small domains formed from the aggregation of the SiPCPs may be the reason that the banding looks more "curvy" and lack of long range order. The narrower pitch could be probably because of the high concentration, but more investigations are needed.

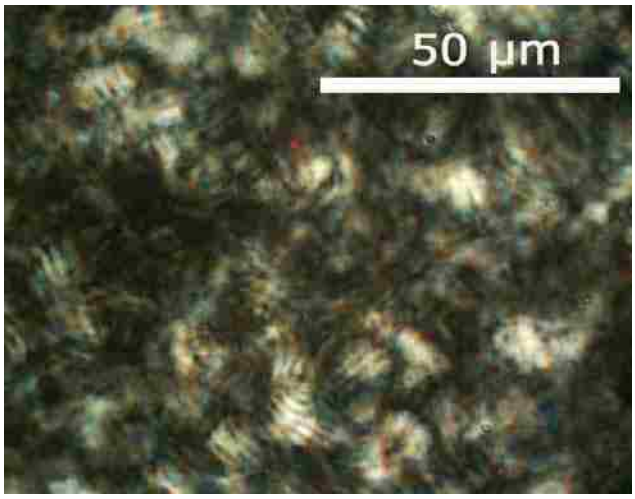

Figure 3.15 P Photomicrograph of SiPCPs (43.87 wt %) in pyridine at room temperature.(R_h of SiO_2 core ≈ 47 nm; R_h of the PBLG-SiPCPs ≈ 408 nm)

The finger-print structures in Figure 3.15 should not be the cholesteric helixes of the PBLG chains, which are already anchored on the SiO_2 spheres. It is also very difficult to understand the assumption, which considers the finger-prints are from stacked SiPCPs. Experiments, such as separating the "aggregated" structure by shearing (if the shearing can take apart the piled particles) and then reinvestigating the crystal structures, can provide some information about the unusual structure. Small angle X-ray scattering (SAXS), which can measure the distance between two particles, can give some ideas about how these particles are located.

3.3.2.3 Crystal Structure of the SiPCPs and PBLG Mixture

The thin, long PBLG rods acted as a strong depletion agent for SiPCPs suspensions in our experiments. Figure 3.16 is the picture of SiPCPs (16.20 wt%) and PBLG (4.80 wt%) in pyridine. A generally similar appearance was found when PBLG and SiPCPs were mixed (Figure 3.16), but the crystalline structures can be observed at lower concentrations than in the solution/suspension, which has only PBLG or SiPCPs. Smaller-globule domains (the diameter is

about 10 μm, and the diameter of the globule domain in Figure 3.15 is about 15 μm) were observed in the mixture. It can be explained as dense, compacted spheres because of the depletion attraction.

Shearing experiments, which are mentioned in section 3.3.2.2, are also desirable here. The experiments may clarify whether the crystalline structures are from piled SiPCPs or cholesteric helixes of PBLG. Consequently, they can tell which component (SiPCPs or PBLG) is more strongly affected by depletion.

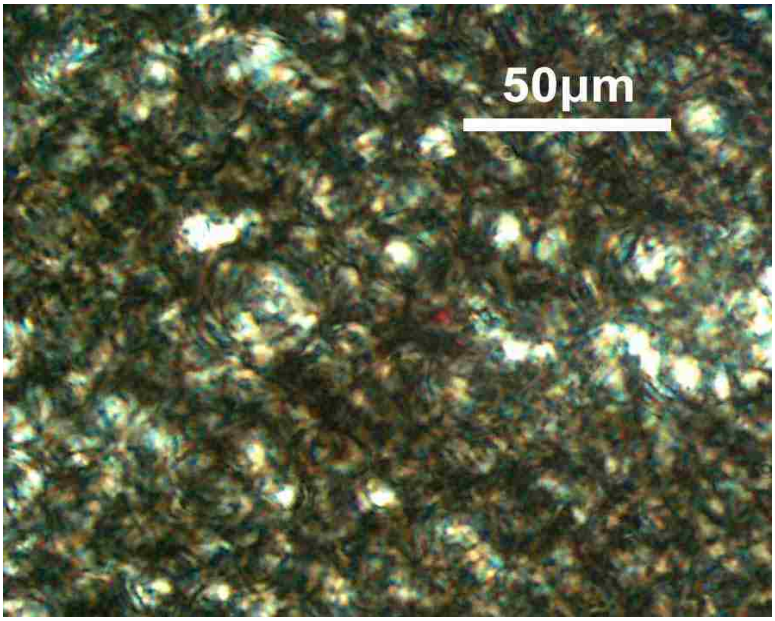

Figure 3.16 Photomicrograph of PBLG (4.80 wt%)/SiPCPs (16.20 wt%) in pyridine at room temperature.(R_h of SiO_2 core ≈ 47 nm; R_h of the PBLG-SiPCPs ≈ 408 nm)

Figure 3.17 shows a phase diagram of PBLG and SiPCPs in pyridine. One can clearly see in the mixture, the concentration of PBLG and SiPCPs needed to form crystal structures (the red and blues dots which are NOT on the x or y axis) is lower than the concentration required in a PBLG solution or in a SiPCPs suspension (for PBLG: the red or blue dots which are on x axis; for SiPCPs: the red or blue dots which are on the y axis). Figure 3.18 is the ternary graph of

PBLG, SiPCPs in pyridine, which also shows the pyridine. The enlarged graph on the upper left corner presents predictions of the I-N transition of PBLG rods by using Onsager's and Flory's theories. Table 3.1 shows the concentration and physical states of PBLG polymer, SiPCPs or mixtures in pyridine.

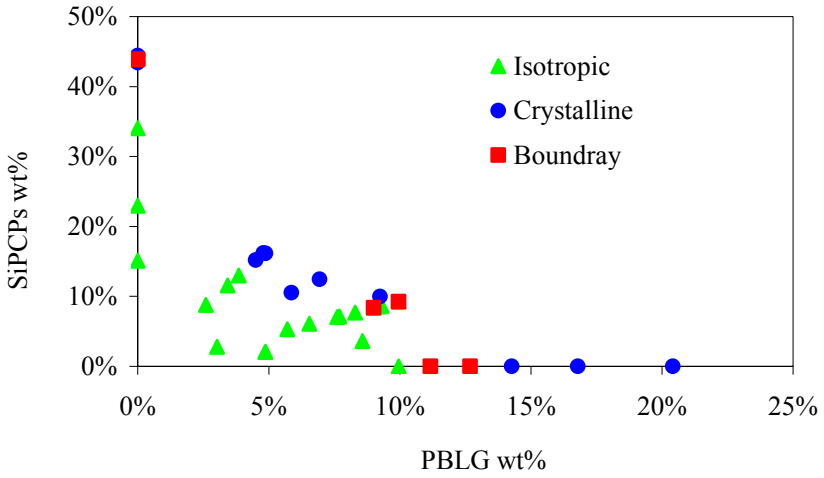

Figure 3.17 The phase diagram of PBLG and SiPCPs in pyridine.

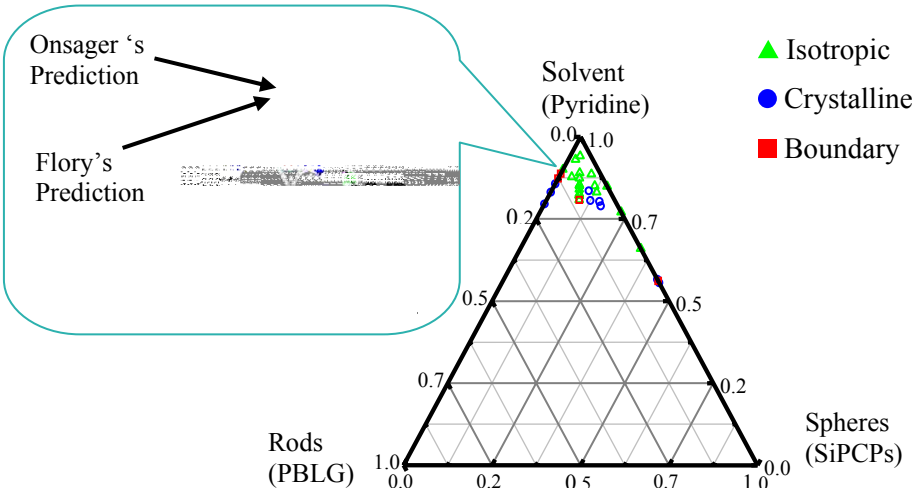

Figure 3.18 Ternary graph of PBLG and SiPCPs in pyridine. The predictions of liquid crystal formation from Onsager and Flory theories are present in the enlarged Figure.

Table 3.1 Physical states of PBLG, SiPCPs, and their mixtures *vs.* concentrations

Components	Wt %		Physical State
PBLG	20.24		LC*
	14.27		LC* starts
	9.95		Isotropic
SiPCPs	43.87		Crystalline
	43.41		Crystalline starts
	34.02		Isotropic
PBLG + SiPCPs	PBLG	SiPCPs	N/A
	3.86	13.10	Isotropic
	8.57	3.63	Isotropic
	4.8	16.2	Crystalline
	5.86	10.52	Crystalline

*LC: liquid crystal

Further investigations for inhomogenization of the anisotropic mixtures were made by mixing fluorescently labeled SiPCPs and PBLG and characterizing the sample with epifluorescence microscopy. Figures 3.19 and 3.20 are the pictures for the exact same area of the FITC- SiPCPs / PBLG sample. The pictures show the mixture is not homogeneous, which suggests that depletion-attraction happens here. Comparing these two figures, one can see the crystalline structures (bright) area in Figure 3.19 is also the bright green area in Figure 3.20, which means the crystalline structure is probably from aggregation of SiPCPs. The two observations:1) higher concentration is required (> 40 wt %) for SiPCPs than for PBLG (>13 wt %) in order to get a crystalline structure; 2) the fact that the crystalline structure comes from SiPCPs in the mixture, may be explained as the depletion-attraction affects SiPCPs more strongly than PBLG rod-like polymers. One can centrifuge the sample (sample has to be loaded in a Vitrocom cell) and reinvestigate the sample with cross-polarized microscopy and epifluorescence microscopy. The results can provide some information about: 1) the stability of the sample and the possibility of phase separation; 2) further evidence about the source (SiPCPs or PBLG) of crystalline structures in the mixture.

If SiPCPs with a cobalt core are available, one can make the mixtures of Co-SiPCPs and PBLG. At high concentrations, the similar structures, which are generated in a mixture of SiPCPs and PBLG (Figure 3.15) are expected. Then, the magnetic field can be applied, and the phase structures may be tuned by moving the external magnetic field. This experiment also can provide some information of the source of crystalline structures since only Co-SiPCPs can respond to the magnetic field.

More information about the detailed structures of SiPCPs and the mixture of PBLG and SiPCPs, which can be obtained by using small angle X-ray scattering or small angle light

scattering, are needed. As mentioned before, the ratio of the size of the spherical particle and the length of the thin rod strongly affects depletion, and consequently influences the structures of their mixture. Polydispersity is another factor even though low-polydispersity samples were used. Variation of SiPCPs and PBLG size and polydispersity is required to complete these investigations. In addition, FITC-labeled PBLG mixed with SiPCPs also can offer some evidence about the inhomogeneity. More information about the detailed structures of SiPCPs and the mixture of PBLG and SiPCPs by using small angle X-ray scattering or small angle light scattering, *etc*., is needed.

3.3.3 Probe Diffusion of FITC SiPCPs through PBLG Matrix

At low concentrations of PBLG, probe (SiPCPs) diffusion results were used to investigate the behaviors of the SiPCPs in SiPCPs / PBLG mixture. As the PBLG (M_w=277,000) is about 190 nm long, and we would like to investigate the diffusion of SiPCPs through a PBLG network, smaller-sized ($D_{SiPCPs} < L$) FITC-labeled SiPCPs were prepared. FITC dye molecules were connected to PBLG polymers (on SiPCPs surface) through the reaction with -NH_2 end groups of PBLG, so at most only one FITC molecule is attached per PBLG polymer chain. Too low fluorescent intensity may cause wrong results from FPR, so the comparison of DLS and FPR measurements of FITC-labeled SiPCPs was made before probe diffusion experiments.

Table 3.2 shows the results of DLS and FPR measurements of FITC-SiPCPs in pyridine at about 0.25 wt % (Batch NO. ES.2.160A). From table 3.2, one can see that the results from DLS and FPR are same in error range. Therefore, the same concentration of the probe (about 0.25%) was kept stable and the concentration of matrix PBLG varied from 0 wt% to 2.0 wt% for probe diffusion experiments.

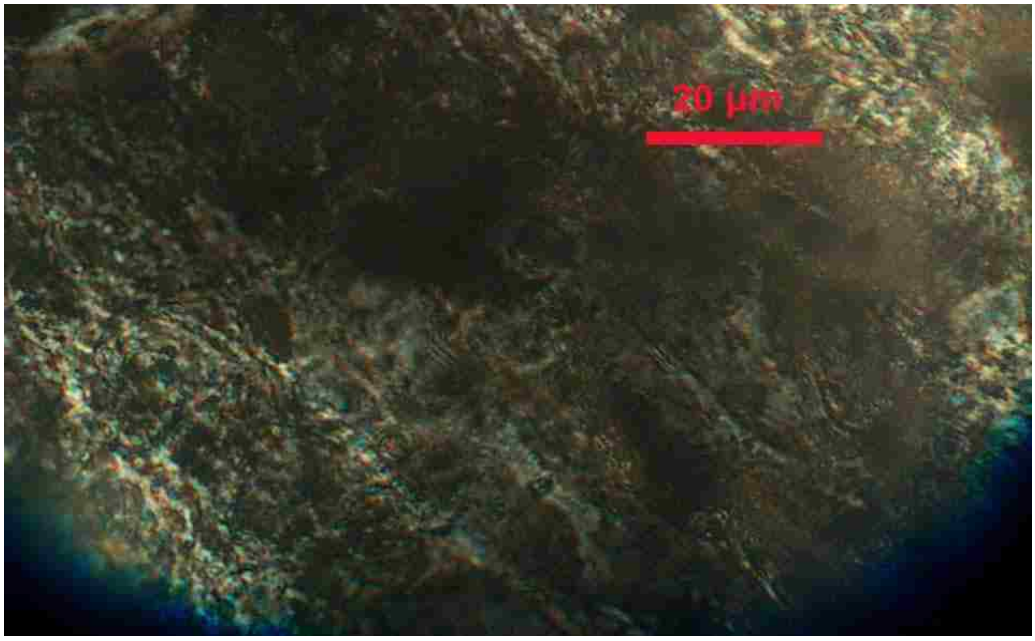

Figure 3.19 Photomicrograph of mixture of FITC-labeled SiPCPs (18.89 wt%) and PBLG (10.04 wt%) in pyridine at room temperature by cross-polarized microscopy.

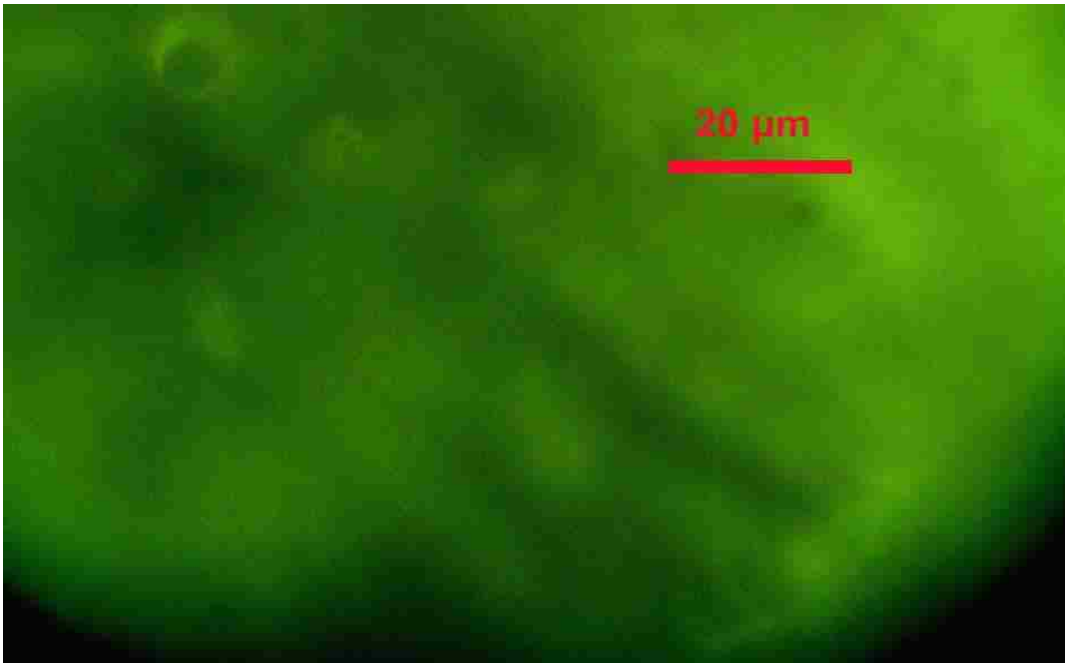

Figure 3.20 Photomicrograph of FITC-labeled SiPCPs (18.89 wt%) and PBLG (10.04 wt%) in pyridine at room temperature by epifluorescence microscopy. (Same spot of sample was examined as in Figure 3.18)

Table 3.2 DLS and FPR measurements of FITC-labeled SiPCPs (≈ 0.25 wt%) in pyridine (ES2.160A, FITC-ES2.160A, both samples were at the same concentration)

method	DLS	FPR
D_{SiPCPs} (cm^2 s^{-1})	3.1E-08 ± 1.1 E-09	3.02E-08 ± 2.1 E-09

Figure 3.21 is the D_{app} *vs.* angle of DLS measurements of 0.25 wt% FITC-SiPCP$_S$ in pyridine. (same DLS measurement as in table 3.2). The almost flat horizontal D_{app} results indicate the particles are quite monodispersed.

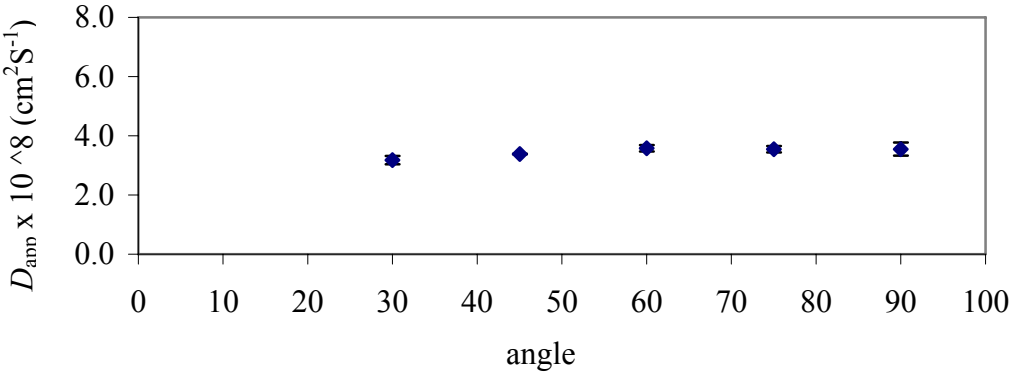

Figure 3.21 The D_{app} *vs.* angle of DLS measurements of 0.25 wt% FITC-SiPCP$_S$ in pyridine. (same DLS measurement as in table 3.2.)

QELSS has been chosen by several groups to measure probe diffusion,[59;82;115-118] while some other groups such as Russo [68;85;119] and Ware [120], selected the self-diffusion method. Compared with self-diffusion, light scattering need fewer steps for preparing the samples, and

the light scattering instruments are more popular, but the light scattering method requires that the matrix and solvent have an identical or very close refractive index, which means only probe scatters light or scatters much stronger than matrix ($I_{probe} / I_{matrix} > 100$). Table 3.3 presents the ratio of scattering intensity of SiPCPs and matrix PBLG at different angles. One can see for our SiPCPs and PBLG mixture sample, light scattering is not always appropriate to measure probe diffusion. Meanwhile, the DLS measurement showed more than one decay on $g^{(1)}(t)$ *vs.* t curve.

The self diffusion technique which traces the diffusion of the probe without being disturbed from the matrix was considered as a suitable method and FPR was chosen for our probe diffusion experiments.

Table 3.3 Scattering intensity of SiPCPs and PBLG in pyridine with different angles

Angle	First trial* (I_{probe} / I_{matrix})	Second trial** (I_{probe} / I_{matrix})
30	128	37
45	95	35
60	73	13
75	79	17
90	66	16

*First trial: Probe (SiPCPs, JQ2.163A): 0.2568 wt%; matrix (PBLG, JQ2.189B): 0.186 wt %
**Second trial: Probe (SiPCPs, JQ2.163A): 0.2568 wt%; matrix (PBLG, JQ2.189C): 0.239 wt %

Figures 3.22 and 3.23 display the raw data (compressed) and the analysis of the compressed data with a 1EXP of sample (JQ.2.174 A) with 0.252 % SiPCPs and 0.097 wt% PBLG in pyridine. Figures 3.24 and 3.25 show the raw data (compressed) and the analysis of the compressed data with a 1EXP of sample (JQ.2.176 A) with 0.244 % SiPCPs and 0.266 wt% PBLG in pyridine. Both raw data and analysis results indicate that the probe diffusion in a higher concentration of the matrix (sample JQ.2.176A, Figure 3.23 and 3.24) is slower. This may be because the solution has a higher viscosity with increased matrix concentration or because of the aggregation of probes (discussed in the following paragraphs).

Figure 3.26 is the diffusion coefficient of the FITC-SiPCPs probe in a PBLG matrix as a function of concentration of PBLG. In Figure 3.26, there is a sharp drop of the diffusion coefficient, which can indicate two possibilities: 1) the PBLG rod-like polymers started to form a network; 2) the SiPCPs become aggregated. Table 3.4 is the comparison of the R_h of SiPCPs in pyridine from DLS and the SLS data of SiPCPs in a PBLG matrix. Data from table 3.4 suggest the aggregation of SiPCPs in PBLG matrix, which is from depletion effect of PBLG rods. But this result can't tell whether there is a PBLG network or not.

Figure 3.27 is the viscosity of PBLG *vs*. concentration of PBLG. The two black lines are the linear fit trend lines for the data. One can see two trend lines are necessary to fit the data. The more-than-one linear fitting also implies the viscosity can not be the first order of the concentration of PBLG.

By Doi's estimation,[121;122] for long thin rods ($L>>d$) solution, v (number density of rods) $>> 1/L^3$ means the rods are *strongly* entangled, while $v << 1/dL^2$ means the solution is very dilute and there are no interactions between rods. It is also can be explained that $1/dL^2$ is the liquid-crystal-formation-minimum limit. As PBLG with M_w=277,000, the concentration range $1/L^3 <<$

$v << 1/dL^2$ corresponds to 0.0067 wt % to 0.8 wt %. The experiment result shows the 1.18wt % PBLG/pyridine solution is a clear, viscous liquid. The characterization by using a cross-polarizing microscope confirms that the sample is isotropic. The discrepancy of Doi's prediction and experimental results is probably because of the diameters of the rods and more importantly the flexibility of the rods especially the high M_w PBLG (M_w=277,000) we used. At high concentrations, the floppy ends of the PBLG chains help the PBLG not to entangle to each other.[123] In addition, if the diameter of rods is comparable to the distance between rods, which is not our situation, the translations diffusion of the rod parallel to the axis is not "free" any more. [124;125] The discrepancy with Doi's estimation is also presented in the result of viscosity of PBLG in pyridine. Figure 3.28 is the viscosity data with 3rd polynomial fit.

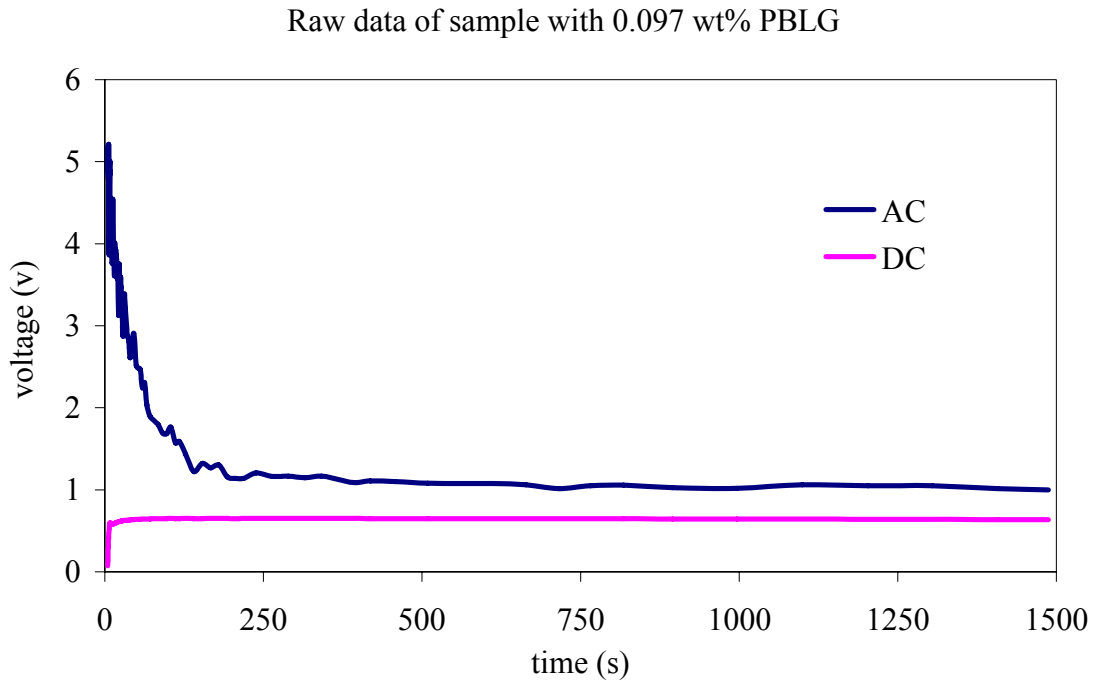

Figure 3.22 The raw FPR data of sample with 0.097 wt% PBLG at 20 °C. (JQ 2.174A. SiPCPs: 0.252 wt%, PBLG: 0.097%; RR = 100 lines per inch; objective = 10×; K = 778 cm^{-1})

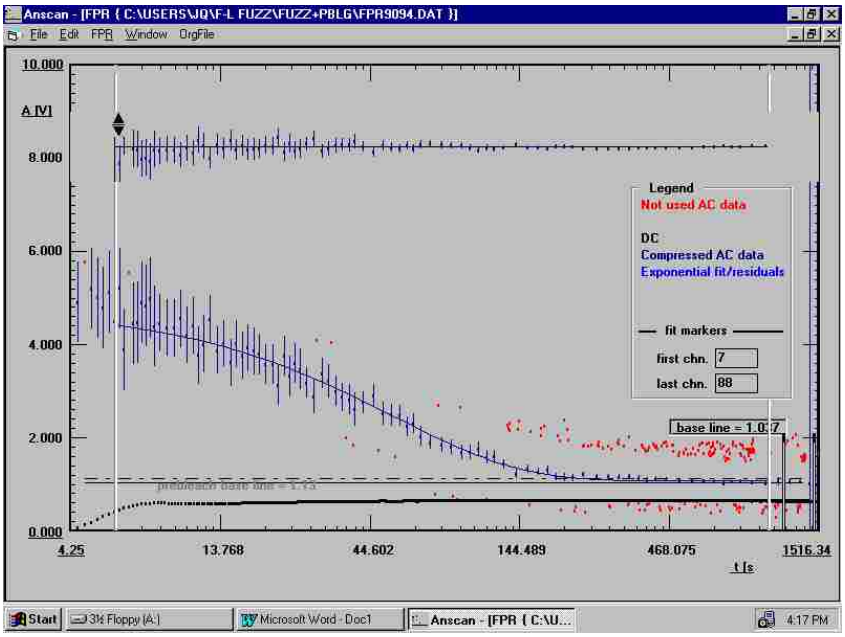

Figure 3.23 The analysis of compressed FPR data of sample with 0.097 wt% PBLG using ANSCAN (1EXP fit). The sample is same as in Figure 3.20. (JQ 2.174A. SiPCPs: 0.252 wt%, PBLG: 0.097 wt%; RR = 100 lines per inch; objective = 10×; K = 778 cm^{-1})

Raw data of sample with 0.266 wt% PBLG

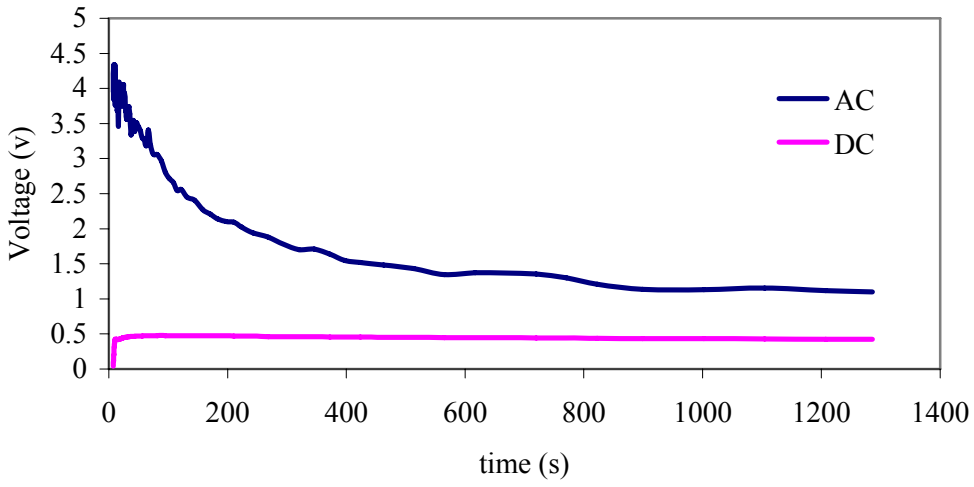

Figure 3.24 The raw FPR data of sample with 0.266 wt% PBLG at 20 °C. (JQ 2.176A. SiPCPs: 0.244 wt%, PBLG: 0.266 wt%; RR = 100 lines per inch; objective = 10×; K = 778 cm^{-1})

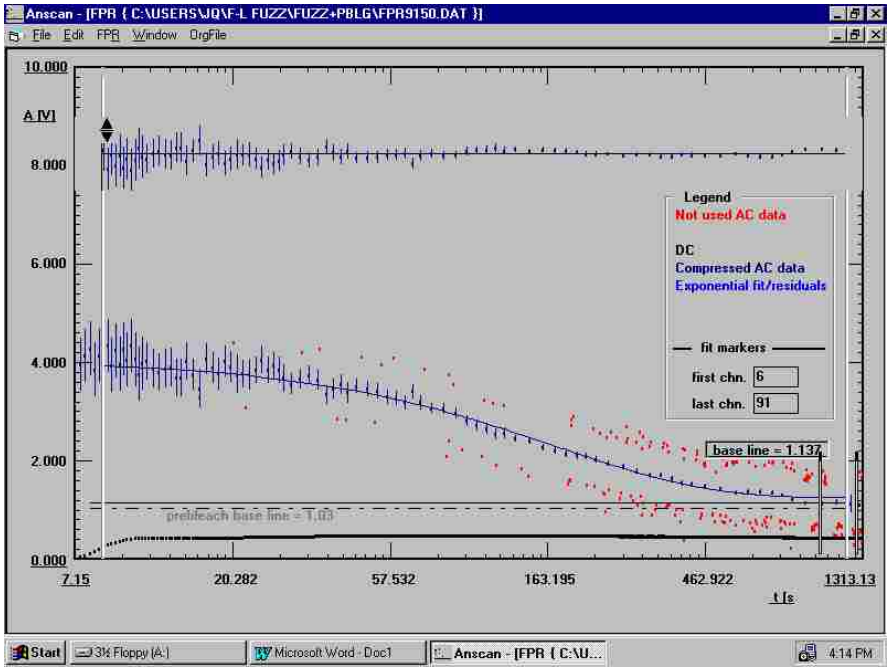

Figure 3.25 The analysis of compressed FPR data of sample with 0.266 wt% PBLG using ANSCAN (1EXP fit). (JQ 2.176A. SiPCPs: 0.244 wt%, PBLG: 0.266 wt%; RR = 100 lines per inch; objective = 10×; K = 778 cm^{-1})

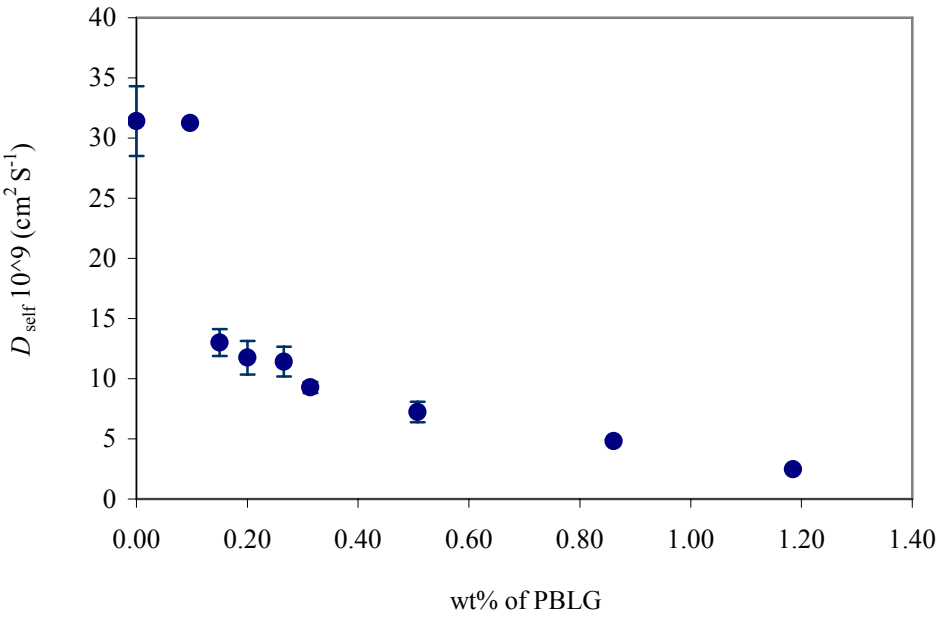

Figure 3.26 The diffusion coefficient (FPR data) of FITC-labeled SiPCPs through PBLG (M_w = 277,000) matrix in pyridine.

Table 3.4 DLS and SLS measurements of SiPCPs in pyridine with or without PBLG matrix (ES2.160 [the core is ES 1.179], JQ 2.176B)

Sample name	R_h from DLS (nm)	Average(R_g/0.775 + $R_{spherical\ fit}$), from SLS (nm)
ES1.179A	50	----------
JQ 2.176B	----------	152

*JQ 2.176 B: Probe (SiPCPs): 0.247 wt%, matrix (PBLG): 0.150 wt %

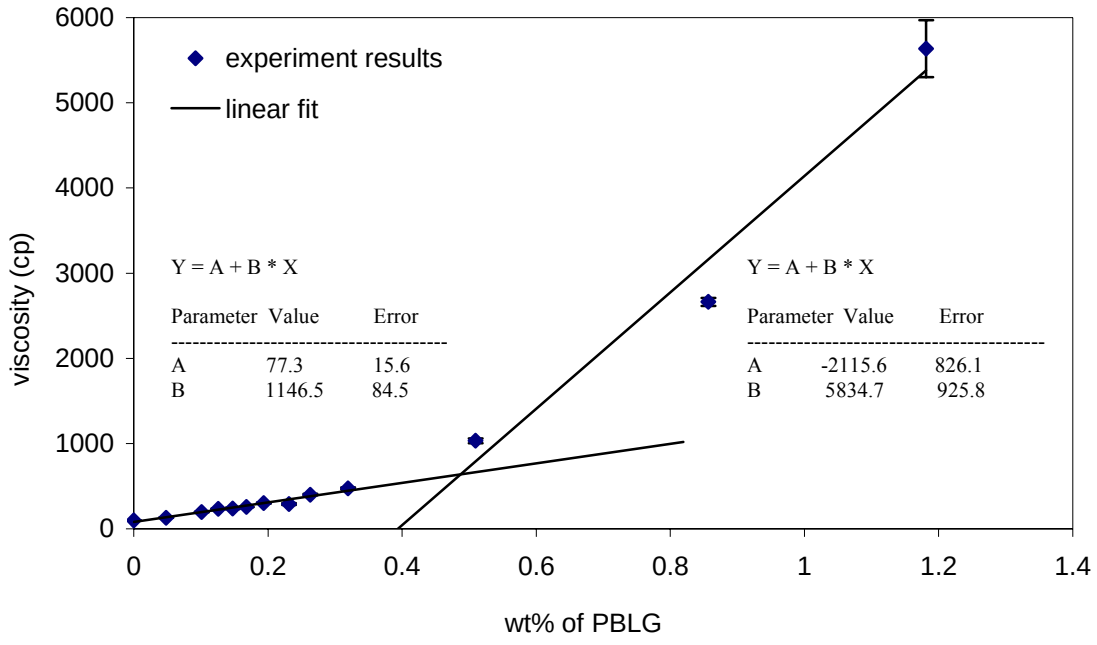

Figure 3.27 Viscosity of PBLG (M_w = 277,000) in pyridine at different concentrations at 20 °C. Linear fit is applied. (The black lines are the linear fit trend lines.)

According to Doi, *et al.*'s prediction,[122]

$$\eta \approx \eta_s (1 + \nu L^3) \quad (\nu << 1/L^3, \text{ very dilute region}) \quad \text{equation 3.26}$$

$$\eta \approx \eta_s \left[1 + (\nu L^3)^3\right] \quad (\nu >> 1/L^3, \text{ concentrated region}) \quad \text{equation 3.27}$$

where η_s is the viscosity of solvent. Equation 3.26 and 3.27 show the viscosity of the solution relates the cube of the length of the rods. In Figure 3.28, the 3rd polynomial trend line, which fits a data much better than the linear model (Figure 3.26), qualitatively agrees Doi's estimation of $\eta \propto L^3$. But quantitatively, as in other studies,[113;123;124] there is a big difference between the experiment and the theory. Figure 3.29 is the comparison of experiment results with Doi's theory for the viscosity of the PBLG solution. Our result is about 5 orders of magnitude lower than predicted. As the diameter of PBLG is only 16 Å, which is quite small compared with the length of the PBLG (L =190 nm), the flexibility and/or hydrodynamic interaction may be responsible.Cush *et al*. investigated the "flexibility" effect by comparing the PBLG with TMV which is almost the perfect colloidal rod in nature.[123] In their study, the PBLG lost about 90% of the diffusion at highest concentration while TMV lost about 50%. Lower molecular weight PBLG behaves more close to theory also suggests the flexibility of PBLG is the most factor here.[113]

As the Stokes-Einstein equation (equation 3.26) shows, $D \propto 1/\eta$ or $D * \eta = \text{constant}$, at steady temperature and radii of the spheres staying constant.

$$R_h = \frac{kT}{6\pi\eta_o D_o} \quad \text{equation 3.26}$$

Figure 3.30 presents the ratio of the diffusion coefficient in a matrix to diffusion coefficient in the pyridine (blue dots) and the reciprocal of the ratio of viscosity of matrix to the viscosity of pyridine.

With the increased concentration of matrix PBLG, the viscosity increases, resulting in reduced diffusion coefficient of the probe. According to the Stokes-Einstein equation, the two series data ([$\eta_{pyridine}/\eta_{matrix}$ *vs*. concentration], and [$D_{probe,\ matrix}/D_{probe,\ pyridine}$ vs. concentration]) should be identical, while in fact there is deviation between the experiment results and the estimation. The diffusion coefficient, therefore, doesn't decrease as much as viscosity increases.

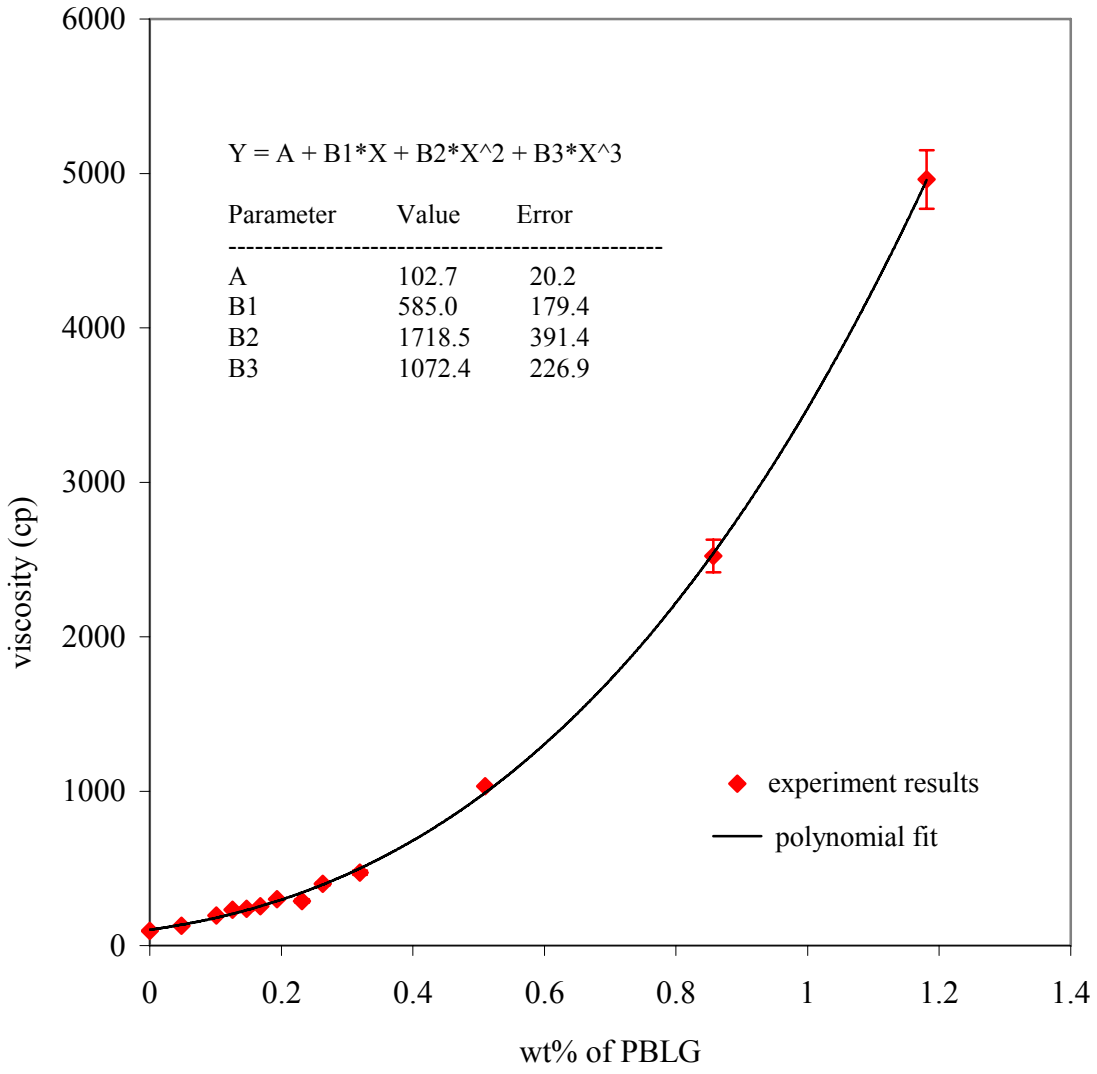

Figure 3.28 Viscosity of PBLG (M_w = 277,000) in pyridine at different concentrations at 20 °C. Third polynomial fit is applied. (The black line is the 3rd polynomial fit trend line.)

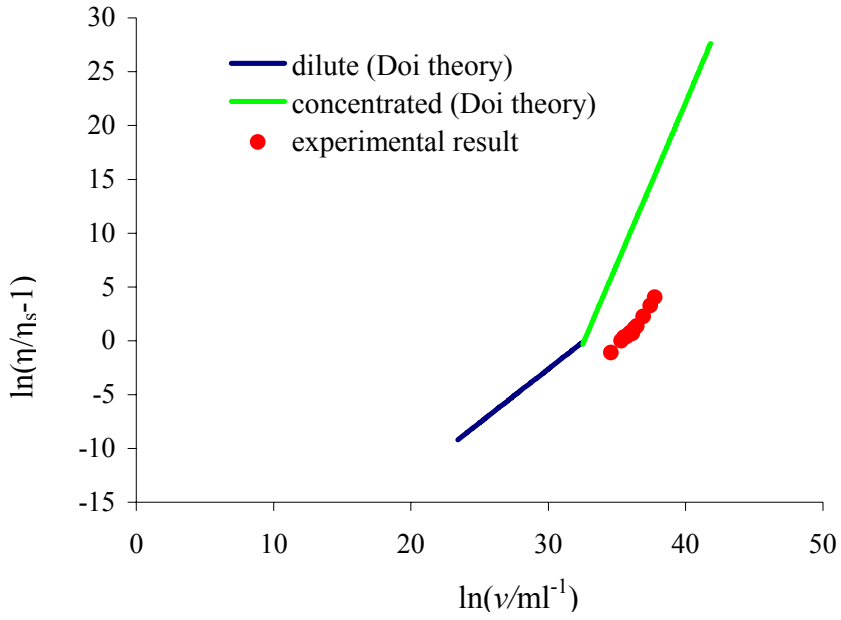

Figure 3.29 Comparison of Doi's estimation and experimental results for viscosity of PBLG in pyridine.

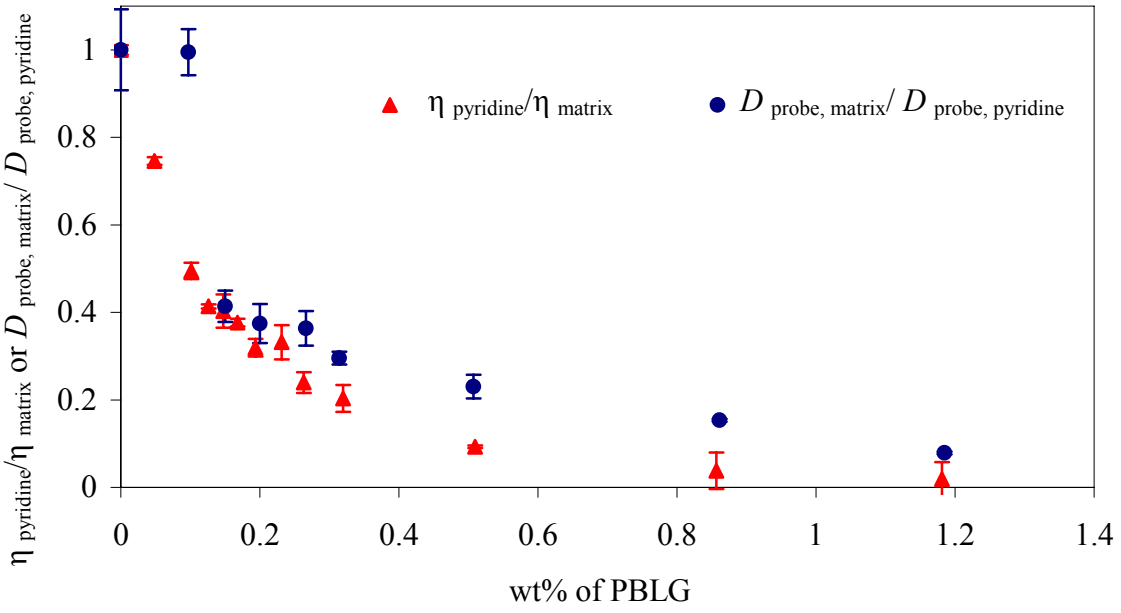

Figure 3.30 $D_{\text{probe, matrix}}/D_{\text{probe, pyridine}}$ or $\eta_{\text{pyridine}}/\eta_{\text{matrix}}$ *vs.* concentration of PBLG in pyridine.

One can also transform equation 3.26 to equation 3.27:

$$\eta D = \frac{kT}{6\pi R_h} \qquad \text{equation 3.27}$$

If there is no aggregation, R_h keeps constant, ηD *vs.* wt% is expected to be a horizontal, straight line. Figure 3.31 is the product of the diffusion coefficient of the SiPCPs probe and the viscosity of the PBLG matrix (in poise) *vs.* the PBLG wt %. The viscosity of PBLG is calculated by using the trend line equation in Figure 3.28:

$$y = (1072.4 \pm 226.9)x^3 + (1718.5 \pm 391.4)x^2 + (585.0 \pm 179.4)x + (102.7 \pm 20.2)$$

where y is viscosity in cp, and x is wt % of PBLG.

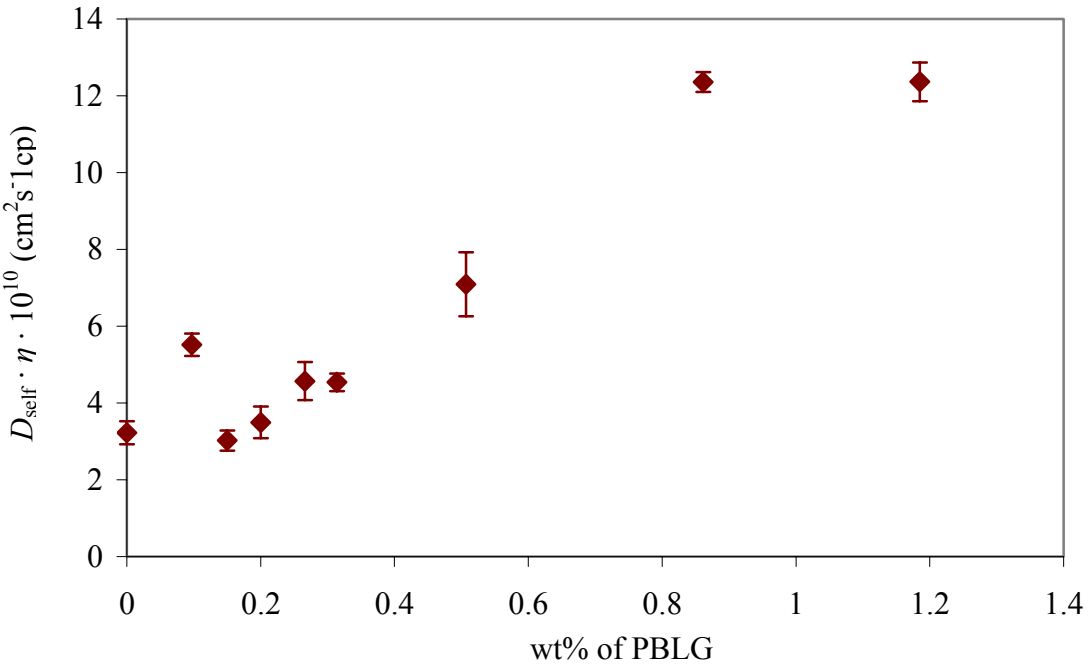

Figure 3.31 Product of D_{self} and viscosity of PBLG matrix *vs.* concentration of PBLG in pyridine. (The viscosity is calculated from the trend line equation in Figure 3.28.)

In Figure 3.31, one can see the product of diffusion coefficient and wt% of PBLG increase when the wt% is above 2% even though the second point is a little bit unusual. This ascending trend was also observed by several studies.[59;82;98;126;127] In 1992, Pecora studied the diffusion of SiO_2 (probe) in PBLG (matrix)/DFM mixture. They observed that the solution-viscosity actually was about *double* the local viscosity surrounding the probe (often called the microviscosity) after the matrix formed a transient network. Consequently the probe diffused faster than expected.[59;82] Probably the same explanation can be applied to our experiment results. However, our results display a slightly higher ratio (about 6-7) of viscosity of solution to local viscosity, possibly because of the different *M*w matrix, the different-sized probe applied, and most importantly the probe SiPCPs have polymer brushes on the surface. Probably the flexibility of matrix, which has been reported by Cantor *et al*.,[98] also affect the probe diffusion. Further studies of probe diffusion with different molecular weight especially high molecular weight PBLG are necessary, and these have been put in our or planned work.

The mixture solution becoming inhomogeneous at a low concentration reminds us that the grafting onto technique, by simply mixing SiO_2 sphere and PBLG, may not lead to SiPCPs with dense surface. In contrast, the aggregation of spheres and network forming from PBLG are not problems for grafting polymer on a *flat* surface.

3.4 Conclusions

In this chapter, the physical properties of the PCBL in *m*-cresol, and the mixture of PBLG-SiPCPs (spheres) and PBLG polypeptides (rods) in pyridine were studied. Optical rotation results prove that the helix-coil transition temperature of PCBL is at about 27 °C. Phase studies of PCBL raise the question of the competition between temperature and concentration in crystalline formation. For the mixture of SiPCPs and PBLG, at high concentrations of SiPCPs

and PBLG, the phase study results confirm the strong depletion interaction. The concentration required to form a crystalline phase in mixture is lower than the concentration needed in a PBLG solution or a SiPCPs suspension. In a low-concentration mixture, the probe diffusion of FITC-labeled SiPCPs through a PBLG matrix was investigated. Diffusion of the probe decreases with the increased PBLG concentration because of the raised viscosity of the matrix solution. However, the decrease of diffusion is less than expected as calculated from the Stokes-Einstein equation. This may be due to the formation of PBLG network, which let the microviscosity be lower than the viscosity of the solution, "drives" the probe particles to move faster than predicted.

3.5 Future work

Since the coil─ helix transition of PCBL is related to the temperature, it will be an interesting topic if we can make a crystal structure of PCBL-SiPCPs or PCBL / SiPCPs mixture, and then investigate the phase behaviors. If the temperature is higher than the coil─ helix transition temperature, PCBL polymer is expected to be rods; consequently, the depletion interaction may exist. So the effects of the temperature, the concentration of each component, and all factors of depletion interaction, such as the size and size distribution of the PCBL and the SiPCPs, can be investigated in one system.

Depletion interaction and probe diffusion in the matrix rely on the size of spheres and rods. Differently sized SiPCPs, especially a large amount of the SiPCPs with varied shell:core ratio, are required. The problem mentioned in chapter 2 emerges again: we need to find a method to synthesize SiPCPs with precise control and in high yields.

Measurements from SAXS or SALS can provide more details about the crystalline structures of concentrated SiPCPs and the mixture of SiPCPs and the polypeptide. Shearing,

which is expected to separate the piled particles, can clarify the crystalline structures of SiPCPs. Stability and the possibility of phase separation of the mixture is expected to be investigated by centrifuging and re-examining with a cross-polarized microscope and an epifluorescence microscope.

Magnetic SiPCPs, which have a cobalt core inside, give the magnetic properties of these particles. For the phase studies, one can mix Co-SiPCPs with normal SiPCPs or PBLG and adjust the external magnetic field. The studies of phase change responding to the external magnetic field will be a very exciting topic, and the novel material with a switchable phase has potential applications in electrical or photonic elements.

3.6 References

1) Russel,W.B.; Saville,D.A.; Schowalter,W.R.*Colloidal Dispersions*; Cambridge University Press , Cambridge: 1989;

2) Schmidt,M.; Denton,A.R. Demixing of colloid-polymer mixtures in poor solvents. *Phys Rev E Stat Nonlin Soft Matter Phys* **2002**, *65*, 061410

3) Ottewill,R.H. Stability of polymer colloids. *NATO ASI Series, Series E: Applied Sciences* **1997**, *335*, 31-48.

4) Hansen,J.P.; McDonald,I.R.*Theory of Simple Liquids. 2nd Ed*; 1986; pp 547

5) Dogic,Z.; Fraden,S. In *Soft Matter: Complex Colloidal Suspensions*; Wiley-VCH Weinheim: 2005. Phase behavior of rod-like viruses and virus-sphere mixtures.

6) Onsager,L. The effects of shapes on the interaction of colloidal particles. *Annals of the New York Academy of Sciences* **1949**, *51*, 627-659.

7) Zocher,H. Spontaneous structure formation in sols; a new kind of anisotropic liquid media. *Z.anorg.allgem.Chem.* **1925**, *147*, 91-110.

8) Lekkerkerker,H.N.W.; Coulon,P.; Van der Haegen,R.; Deblieck,R. On the isotropic-liquid crystal phase separation in a solution of rodlike particles of different lengths. *Journal of Chemical Physics* **1984**, *80*, 3427-3433.

9) Lekkerkerker,H.N.W.; Stroobants,A. Phase behavior of rod-like colloid + flexible polymer mixtures. *Nuovo Cimento della Societa Italiana di Fisica, D: Condensed Matter, Atomic, Molecular and Chemical Physics, Fluids, Plasmas, Biophysics* **1994**, *16D*, 949-962.

10) Mao,Y.; Cates,M.E.; Lekkerkerker,H.N.W. Depletion stabilization by semidilute rods. *Physical Review Letters* **1995**, *75*, 4548-4551.

11) Mao,Y.; Cates,M.E.; Lekkerkerker,H.N.W. Theory of the depletion force due to rodlike polymers. *Journal of Chemical Physics* **1997**, *106*, 3721-3729.

12) Adams,M.; Dogic,Z.; Keller,S.L.; Fraden,S. Entropically driven microphase transitions in mixtures of colloidal rods and spheres. *Nature (London)* **1998**, *393*, 349-352.

13) Dogic,Z.; Purdy,K.R.; Grelet,E.; Adams,M.; Fraden,S. Isotropic-nematic phase transition in suspensions of filamentous virus and the neutral polymer Dextran. *Physical Review E: Statistical, Nonlinear, and Soft Matter Physics* **2004**, *69*, 051702-1-051702/9.

14) Maier,W.; Saupe,A. A simple molecular theory of the nematic crystalline-liquid state. *Zeitschrift fuer Naturforschung* **1958**, *13a*, 564-566.

15) Luckhurst,G.R.; Zannoni,C. Why is the Maier-Saupe theory of nematic liquid crystals so successful? *Nature (London, United Kingdom)* **1977**, *267*, 412-414.

16) Maier,W.; Saupe,A. A simple molecular statistical theory of the nematic crystalline-liquid phase. I. *Zeitschrift fuer Naturforschung* **1959**, *14a*, 882-889.

17) Straley,J.P. Third virial coefficient for the gas of long rods. *Molecular Crystals and Liquid Crystals* **1973**, *24*, 7-20.

18) Frenkel,D. Structure of hard-core models for liquid crystals. *Journal of Physical Chemistry* **1988**, *92*, 3280-3284.

19) Kayser,R.F., Jr.; Raveche,H.J. Bifurcation in Onsager's model of the isotropic-nematic transition. *Physical Review A: Atomic, Molecular, and Optical Physics* **1978**, *17*, 2067-2072.

20) Chen,Z.Y. Nematic ordering in semiflexible polymer chains. *Macromolecules* **1993**, *26*, 3419-3423.

21) Khokhlov,A.R.; Semenov,A.N. Liquid-crystalline ordering in the solution of long persistent chains. *Physica A: Statistical Mechanics and Its Applications (Amsterdam, Netherlands)* **1981**, *108A*, 546-556.

22) Khokhlov,A.R.; Semenov,A.N. Liquid-crystalline ordering in a solution of partially flexible macromolecules. *Physica A: Statistical Mechanics and Its Applications (Amsterdam, Netherlands)* **1982**, *112A*, 605-614.

23) Purdy,K.; Varga,S.; Galindo,A.; Jackson,G.; Fraden,S. Nematic phase transitions in mixtures of thin and thick colloidal rods. *Los Alamos National Laboratory, Preprint Archive, Condensed Matter* **2004**, 1-11, arXiv.

24) Shundyak,K.; Van Roij,R.; Van der Schoot,P. Phase behavior and interfacial properties of nonadditive mixtures of Onsager rods. *Journal of Chemical Physics* **2005**, *122*, 094912-1-094912/8.

25) Flory,P.J. Phase equilibriums in solutions of rodlike particles. *Proc.Roy.Soc.(London)* **1956**, *A234*, 73-89.

26) Flory,P.J. Statistical thermodynamics of semiflexible chain molecules. *Proc.Roy.Soc.(London)* **1956**, *A234*, 60-73.

27) Cotter,M.A.; Wacker,D.C. Van der Waals theory of nematogenic solutions. I. Derivation of the general equations. *Physical Review A: Atomic, Molecular, and Optical Physics* **1978**, *18*, 2669-2675.

28) Asakura,S.; Oosawa,F. Interaction between particles suspended in solutions of macromolecules. *Journal of Polymer Science* **1958**, *33*, 183-192.

29) Ping,G.; Yang,G.; Yuan,J.M. Depletion force from macromolecular crowding enhances mechanical stability of protein molecules. *Polymer* **2006**, *47*, 2564-2570.

30) Gast,A.P.; Hall,C.K.; Russel,W.B. Phase separations induced in aqueous colloidal suspensions by dissolved polymer. *Faraday Discussions of the Chemical Society* **1983**, 189-201.

31) Gast,A.P.; Hall,C.K.; Russel,W.B. Polymer-induced phase separations in nonaqueous colloidal suspensions. *Journal of Colloid and Interface Science* **1983**, *96*, 251-267.

32) Lekkerkerker,H.N.W.; Poon,W.C.K.; Pusey,P.N.; Stroobants,A.; Warren,P.B. Phase behavior of colloid + polymer mixtures. *Europhysics Letters* **1992**, *20*, 559-564.

33) Lebowit,J.L. Thermodynamic properties of mixtures of hard spheres. *J.S.Rowlinson.J.Chem.Phys.* **1964**, *41*, 135-138.

34) Biben,T.; Hansen,J.P. Phase separation of asymmetric binary hard-sphere fluids. *Physical Review Letters* **1991**, *66*, 2215-2218.

35) Koenderink,G.H.; Vliegenthart,G.A.; Kluijtmans,S.G.J.M.; van Blaaderen,A.; Philipse,A.P.; Lekkerkerker,H.N.W. Depletion-Induced Crystallization in Colloidal Rod-Sphere Mixtures. *Langmuir* **1999**, *15*, 4693-4696.

36) Oversteegen,S.M.; Wijnhoven,J.G.E.J.; Vonk,C.; Lekkerkerker,H.N.W. Crystallization Kinetics and Morphology in Phase Separating and Sedimenting Mixtures of Colloidal Spheres and Rods. *Journal of Physical Chemistry B* **2004**, *108*, 18158-18163.

37) Tracy,M.A.; Garcia,J.L.; Pecora,R. An investigation of the microstructure of a rod/sphere composite liquid. *Macromolecules* **1993**, *26*, 1862-1868.

38) Dogic,Z.; Frenkel,D.; Fraden,S. Enhanced stability of layered phases in parallel hard spherocylinders due to addition of hard spheres. *Physical Review E: Statistical Physics, Plasmas, Fluids, and Related Interdisciplinary Topics* **2000**, *62*, 3925-3933.

39) Kwon,H.J.; Gong,J.P. Negatively charged polyelectrolyte gels as bio-tissue model system and for biomedical application. *Current Opinion in Colloid & Interface Science* **2006**, *11*, 345-350.

40) Vera,M.; Puiggali,J.; Coudane,J. Microspheres from new biodegradable poly(ester amide)s with different ratios of L- and D-alanine for controlled drug delivery. *Journal of Microencapsulation* **2006**, *23*, 686-697.

41) Levy,Y.; Zilberman,M. Novel bioresorbable composite fiber structures loaded with proteins for tissue regeneration applications: microstructure and protein release. *Journal of Biomedical Materials Research, Part A* **2006**, *79A*, 779-787.

42) Pfohl,O.; Dohrn,R. Thermodynamic properties of polymer systems for industrial applications. *Fluid Phase Equilibria* **2004**, *217*, 189-199.

43) Howley,R.; MacCraith,B.D.; O'Dwyer,K.; Kirwan,P.; McLoughlin,P. A study of the factors affecting the diffusion of chlorinated hydrocarbons into polyisobutylene and polyethylene-co-propylene for evanescent wave sensing. *Vibrational Spectroscopy* **2003**, *31*, 271-278.

44) Roy,S. Hygrothermal modeling of polymers and polymer matrix composites. *ASTM Special Technical Publication* **2000**, *STP 1357*, 338-352.

45) McCabe,M. Diffusion coefficients in polymer solutions. *Biochemical Journal* **1967**, *104*, 8P

46) Desbrieres,J.; Borsali,R.; Rinaudo,M.; Milas,M. cF Interaction parameter and the single-chain diffusion coefficients of dextran/poly(vinylpyrrolidone)/water: dynamic light scattering experiments. *Macromolecules* **1993**, *26*, 2592-2596.

47) Klein,J. Dynamics of entangled linear, branched, and cyclic polymers. *Macromolecules* **1986**, *19*, 105-118.

48) Fick,A.*Poggendorff's Annel.Physik.* **1855**, *94*,

49) Vink,H. Mutual diffusion and self-diffusion in the frictional formalism of nonequilibrium thermodynamics. *Journal of the Chemical Society, Faraday Transactions 1: Physical Chemistry in Condensed Phases* **1985**, *81*, 1725-1730.

50) Gero,V. Diffusion and brownian Motion analogies in the migration of atoms, animals, men and ideas. *Internat.conference "Diffusion Fundamentals I"* **2005**,

51) Varma,B.K.; Fukita,Y.; Takahashi,M.; Nose,T. Hydrodynamic radius and intrinsic viscosity of polystyrene in the crossover region from q to good-solvent conditions. *Journal of Polymer Science, Polymer Physics Edition* **1984**, *22*, 1781-1797.

52) Wagner,J.; Hartl,W.; Walderhaug,H. Long time self-diffusion in suspensions of highly charged colloids: A comparison between pulsed field gradient NMR and Brownian dynamics. *Journal of Chemical Physics* **2001**, *114*, 975-983.

53) Hadden,D.A.; Rill,R.L.; McFaddan,L.; Locke,B.R. Oligonucleotide and Water Self-Diffusion in Systems of Pluronic Triblock Copolymers and in Buffer Solutions by Pulsed Field Gradient Nuclear Magnetic Resonance. *Macromolecules* **2000**, *33*, 4235-4248.

54) Callaghan,P.T.; Le Gros,M.A.; Pinder,D.N. The measurement of diffusion using deuterium pulsed field gradient nuclear magnetic resonance. *Journal of Chemical Physics* **1983**, *79*, 6372-6381.

55) Price,W.S. Pulsed-field gradient nuclear magnetic resonance as a tool for studying translational diffusion: Part 1. Basic theory. *Concepts in Magnetic Resonance* **1997**, *9*, 299-336.

56) Cabrita,E.J.; Berger,S.; Braeuer,P.; Kaerger,J. High-Resolution DOSY NMR with Spins in Different Chemical Surroundings: Influence of Particle Exchange. *Journal of Magnetic Resonance* **2002**, *157*, 124-131.

57) Huo,R.; Wehrens,R.; Van Duynhoven,J.; Buydens,L.M.C. Assessment of techniques for DOSY NMR data processing. *Analytica Chimica Acta* **2003**, *490*, 231-251.

58) Pecora,R. Dynamics in rod-sphere composite liquids. *NATO Science Series, Series C: Mathematical and Physical Sciences* **2002**, *568*, 47-81.

59) Tracy,M.A.; Pecora,R. Synthesis, characterization, and dynamics of a rod/sphere organoceramic composite liquid. *Materials Research Society Symposium Proceedings* **1992**, *274*, 109-114.

60) De Smedt,S.C.; Lauwers,A.; Demeester,J.; Engelborghs,Y.; De Mey,G.; Du,M. Structural information on hyaluronic acid solutions as studied by probe diffusion experiments. *Macromolecules* **1994**, *27*, 141-146.

61) Smith,B.A.; Mumby,S.J.; Samulski,E.T.; Yu,L.P. Concentration dependence of the diffusion of poly(propylene oxide) in the melt. *Macromolecules* **1986**, *19*, 470-472.

62) Scalettar,B.A.; Hearst,J.E.; Klein,M.P. FRAP and FCS studies of self-diffusion and mutual diffusion in entangled DNA solutions. *Macromolecules* **1989**, *22*, 4550-4559.

63) Magde,D.; Elson,E.; Webb,W.W. Thermodynamic fluctations in a reacting system. Measurement by fluorescence correlation spectroscopy. *Physical Review Letters* **1972**, *29*, 705-708.

64) Aragon,S.R.; Pecora,R. Fluorescence correlation spectroscopy as a probe of molecular dynamics. *Journal of Chemical Physics* **1976**, *64*, 1791-1803.

65) Haustein,E.; Schwille,P. Ultrasensitive investigations of biological systems by fluorescence correlation spectroscopy. *Methods (San Diego, CA, United States)* **2003**, *29*, 153-166.

66) Kim,H.; Chang,T.; Yohanan,J.M.; Wang,L.; Yu,H. Polymer diffusion in linear matrixes: polystyrene in toluene. *Macromolecules* **1986**, *19*, 2737-2744.

67) Daivis,P.; Snook,I.; Van Megen,W.; Preston,B.N.; Comper,W.D. Dynamic light scattering measurements of diffusion in polymer-polymer-solvent systems. *Macromolecules* **1984**, *17*, 2376-2380.

68) Bu,Z.; Russo,P.S. Diffusion of Dextran in Aqueous (Hydroxypropyl)cellulose. *Macromolecules* **1994**, *27*, 1187-1194.

69) Bu,Z.; Tipton,D.L.; Poche,D.S.; Negulescu,I.; Daly,W.H.; Russo,P.S. Self diffusion of semiflexible polymers. *Polymer Preprints (American Chemical Society, Division of Polymer Chemistry)* **1993**, *34*, 632

70) Turner,D.N.; Hallett,F.R. A study of the diffusion of compact particles in polymer solutions using quasi-elastic light scattering. *Biochim Biophys Acta* **1976**, *451*, 305-312.

71) Phillies,G.D.J.; Lacroix,M. Probe Diffusion in Hydroxypropylcellulose-Water: Radius and Line-Shape Effects in the Solutionlike Regime. *Journal of Physical Chemistry B* **1997**, *101*, 39-47.

72) Streletzky,K.A.; Phillies,G.D.J. Probe diffusion in high molecular weight hydroxypropylcellulose. Solutionlike and meltlike regimes. *Book of Abstracts, 216th ACS National Meeting, Boston, August 23-27* **1998**, MSE-183

73) Streletzky,K.A.; Phillies,G.D.J. Relaxational mode structure for optical probe diffusion in high molecular weight hydroxypropylcellulose. *Journal of Polymer Science, Part B: Polymer Physics* **1998**, *36*, 3087-3100.

74) Cush,R.; Russo,P.S.; Kucukyavuz,Z.; Bu,Z.; Neau,D.; Shih,D.; Kucukyavuz,S.; Ricks,H. Rotational and translational diffusion of a rodlike virus in random coil polymer solutions. *Macromolecules* **1997**, *30*, 4920-4926.

75) Cush,R.; Dorman,D.; Russo,P.S. Rotational and Translational Diffusion of Tobacco Mosaic Virus in Extended and Globular Polymer Solutions. *Macromolecules* **2004**, *37*, 9577-9584.

76) Hanley,B.; Tirrell,M.; Lodge,T. The behavior of the tracer diffusion coefficient of polystyrene in isorefractive \"solvents\" composed of poly(vinyl methyl ether) and o-fluorotoluene. *Polymer Bulletin (Berlin, Germany)* **1985**, *14*, 137-142.

77) Lodge,T.P. Self-diffusion of polymers in concentrated ternary solutions by dynamic light scattering. *Macromolecules* **1983**, *16*, 1393-1395.

78) Martin,J.E. Polymer self-diffusion: dynamic light scattering studies of isorefractive ternary solutions. *Macromolecules* **1984**, *17*, 1279-1283.

79) Martin,J.E. Polymer self-diffusion in bimodal semidilute solutions. *Macromolecules* **1986**, *19*, 922-925.

80) Daivis,P.J.; Pinder,D.N. Dynamic light scattering experiments on poly(vinyl methyl ether) (PVME)-polystyrene-toluene and PVME-polystyrene-carbon tetrachloride solutions. *Macromolecules* **1993**, *26*, 3381-3390.

81) Corrotto,J.; Ortega,F.; Vazquez,M.; Freire,J.J. Dynamic Light Scattering from Mixtures of Two Polystyrene Samples in Dilute and Semidilute Solutions. *Macromolecules* **1996**, *29*, 5948-5954.

82) Tracy,M.A.; Pecora,R. Synthesis, characterization, and dynamics of a rod/sphere composite liquid. *Macromolecules* **1992**, *25*, 337-349.

83) Brown,W.; Stilbs,P. Self-diffusion of poly(ethylene oxide) in aqueous dextran solutions measured using FT-pulsed field gradient NMR. *Polymer* **1983**, *24*, 188-192.

84) Nyden,M.; Soederman,O.; Karlstroem,G. A PFG NMR self-diffusion investigation of probe diffusion in an ethyl hydroxyethyl cellulose matrix. *Macromolecules* **1999**, *32*, 127-135.

85) Wattenbarger,M.R.; Bloomfield,V.A.; Bu,Z.; Russo,P.S. Tracer diffusion of proteins in DNA solutions. *Macromolecules* **1992**, *25*, 5263-5265.

86) Cong,R.; Temyanko,E.; Russo,P.S. Diffusion of Labeled Polyelectrolyte Probes in Unlabeled Polyelectrolyte Matrix Solutions. *Macromolecules* **2005**, *38*, 10627-10630.

87) Daivis,P.J.; Pinder,D.N.; Callaghan,P.T. Dynamic light scattering and pulsed gradient spin-echo NMR measurements of diffusion in polystyrene-poly(vinyl methyl ether)-toluene solutions. *Macromolecules* **1992**, *25*, 170-178.

88) Chang,T.; Han,C.C.; Wheeler,L.M.; Lodge,T.P. Comparison of diffusion coefficients in ternary polymer solutions measured by dynamic light scattering and forced Rayleigh scattering. *Macromolecules* **1988**, *21*, 1870-1872.

89) Tinland,B.; Borsali,R. Single-Chain Diffusion Coefficient of F-Dextran in Poly(vinylpyrrolidone)/Water: Fluorescence Recovery after Photobleaching Experiments. *Macromolecules* **1994**, *27*, 2141-2144.

90) De Gennes,P.G. In 1979; pp 324. Scaling Concepts in Polymer Physics

91) Adler,R.S.; Freed,K.F. On dynamic scaling theories of polymer solutions at nonzero concentrations. *Journal of Chemical Physics* **1980**, *72*, 4186-4193.

92) Phillies,G.D.J. Dynamics of polymers in concentrated solutions: the universal scaling equation derived. *Macromolecules* **1987**, *20*, 558-564.

93) Phillies,G.D.J. Self and tracer diffusion of polymers in solution. *Los Alamos National Laboratory, Preprint Archive, Condensed Matter* **2004**, 1-53, arXiv.

94) Tao,H.; Lodge,T.P.; von Meerwall,E.D. Diffusivity and Viscosity of Concentrated Hydrogenated Polybutadiene Solutions. *Macromolecules* **2000**, *33*, 1747-1758.

95) Xuexin,C.; Zhongde,X.; Von Meerwall,E.; Seung,N.; Hadjichristidis,N.; Fetters,L.J. Self-diffusion of linear and 4- and 18-armed star polyisoprenes in tetrachloromethane solution. *Macromolecules* **1984**, *17*, 1343-1348.

96) Von Meerwall,E.; Tomich,D.H.; Hadjichristidis,N.; Fetters,L.J. Phenomenology of self-diffusion in star-branched polyisoprenes in solution. *Macromolecules* **1982**, *15*, 1157-1163.

97) Von Meerwall,E.; Tomich,D.H.; Grigsby,J.; Pennisi,R.W.; Fetters,L.J.; Hadjichristidis,N. Self-diffusion of three-armed star and linear polybutadienes and polystyrenes in tetrachloromethane solution. *Macromolecules* **1983**, *16*, 1715-1722.

98) Cantor,A.S.; Pecora,R. Dynamics of Flexible Coils in an Isorefractive Rod/Coil Composite Liquid. 2. Ternary Solutions. *Macromolecules* **1994**, *27*, 6817-6833.

99) Matsuoka,M.; Norisuye,T.; Teramoto,A.; Fujita,H. Solution properties of synthetic polypeptides. XV. Helix-coil transition in poly(ε-carbobenzyloxy-*L*-lysine). *Biopolymers* **1973**, *12*, 1515-1532.

100) Nakamoto,K.; Suga,H.; Seki,S.; Teramoto,A.; Norisuye,T.; Fujita,H. Solution properties of synthetic polypeptides. XIX. Heat capacity measurements on the system of poly(ε-carbobenzyloxy-*L*-lysine) and m-cresol in the helix-coil transition region. *Macromolecules* **1974**, *7*, 784-788.

101) Omura,I.; Teramoto,A.; Fujita,H. Dielectric dispersion of polypeptide solutions. II. Helix-coil transition of poly(ε-carbobenzoxy-*L*-lysine) in m-cresol. *Macromolecules* **1975**, *8*, 284-290.

102) Sibel Turksen. Synthesis and characterization of superparamagnetic silica-homopolypeptide composite particles. 2005.

103) Monzen,K.; Hiraoka,K.; Uematsu,Y.; Date,M. Banded texture induced by an electric field in polymeric liquid crystalline solution. *Polymer Journal (Tokyo)* **1998**, *30*, 499-507.

104) Tadmor,R.; Khalfin,R.L.; Cohen,Y. Reversible Gelation in Isotropic Solutions of the Helical Polypeptide Poly(γ-benzyl-*L*-glutamate): Kinetics and Formation Mechanism of the Fibrillar Network. *Langmuir* **2002**, *18*, 7146-7150.

105) Tanaka,K.; Oiwa,Y.; Kiguchi,T.; Akiyama,R. Simultaneous optical observation of anisotropic texture for a concentrated solution of poly(γ-benzyl-*L*-glutamate) under transient stress response in shear flow. *Colloid and Polymer Science* **2000**, *278*, 1211-1215.

106) Urano,T.I.; Machida,S.; Sano,K. A new variable orienting force for liquid crystals which has its origin in the electric property of poly(γ-benzyl-*L*-glutamate) CRA film. *Journal of the Chemical Society, Chemical Communications* **1994**, 231-232.

107) Wang,Y.; Chang,Y.C. Alignment of rigid-rod polypeptide chains by solvent quenching. *Materials Research Society Symposium Proceedings* **2003**, *771*, 345-350.

108) Yamamoto,S.; Tsujii,Y.; Fukuda,T. Characteristic phase-separated monolayer structure observed for blends of rodlike and flexible polymers. *Polymer* **2000**, *42*, 2007-2013.

109) Robinson,C. Liquid crystalline structures in polypeptide solutions. *Tetrahedron* **1961**, *13*, 219-234.

110) Robinson,C.; Ward,J.C.; Beevers,R.B. Liquid crystalline structure in polypeptide solutions. II. *Discussions of the Faraday Society* **1958**, *No. 25*, 29-42.

111) Toriumi,H.; Yahagi,K.; Uematsu,I.; Uematsu,Y. Cholesteric structure of lyotropic poly(γ-benzyl *L*-glutamate) liquid crystals. *Molecular Crystals and Liquid Crystals* **1983**, *94*, 267-284.

112) Flory,P.J. Molecular theory of liquid crystals. *Advances in Polymer Science* **1984**, *59*, 1-36.

113) Bu,Z.; Russo,P.S.; Tipton,D.L.; Negulescu,I.I. Self-Diffusion of Rodlike Polymers in Isotropic Solutions. *Macromolecules* **1994**, *27*, 6871-6882.

114) Fong,B.; Turksen,S.; Russo,P.S.; Stryjewski,W. Colloidal Crystals of Silica-Homopolypeptide Composite Particles. *Langmuir* **2004**, *20*, 266-269.

115) Phillies,G.D.J.; Clomenil,D. Probe diffusion in polymer solutions under Q and good conditions. *Macromolecules* **1993**, *26*, 167-170.

116) Richtering,W.; Berend,K. Dynamics of monodisperse and bidisperse polymer latexes. *Progress in Colloid & Polymer Science* **1995**, *98*, 79-84.

117) Tracy,M.A.; Garcia,J.L.; Pecora,R. An investigation of the microstructure of a rod/sphere composite liquid. *Macromolecules* **1993**, *26*, 1862-1868.

118) Tracy,M.A.; Pecora,R. Application of probe diffusion models to sphere diffusion in a rod/sphere composite liquid. *Proceedings of SPIE-The International Society for Optical Engineering* **1993**, *1884*, 88-99.

119) Mustafa,M.; Russo,P.S. Diffusion of spherical probes in aqueous systems containing the semiflexible polymer, hydroxypropylcellulose. *Proceedings of SPIE-The International Society for Optical Engineering* **1991**, *1430*, 132-141.

120) Gorti,S.; Ware,B.R. Probe diffusion in an aqueous polyelectrolyte solution. *Journal of Chemical Physics* **1985**, *83*, 6449-6456.

121) Doi,M.; Edwards,S.F. Dynamics of rod-like macromolecules in concentrated solution. Part 1. *Journal of the Chemical Society, Faraday Transactions 2: Molecular and Chemical Physics* **1978**, *74*, 560-570.

122) Doi,M.; Edwards,S.F. Dynamics of rod-like macromolecules in concentrated solution. Part 2. *Journal of the Chemical Society, Faraday Transactions 2: Molecular and Chemical Physics* **1978**, *74*, 918-930.

123) Cush,R.C.; Russo,P.S. Self-Diffusion of a Rodlike Virus in the Isotropic Phase. *Macromolecules* **2002**, *35*, 8659-8662.

124) Zero,K.M.; Pecora,R. Rotational and translational diffusion in semidilute solutions of rigid-rod macromolecules. *Macromolecules* **1982**, *15*, 87-93.

125) DeLong,L.M.; Russo,P.S. Thermodynamic and dynamic behavior of semiflexible polymers in the isotropic phase. *Macromolecules* **1991**, *24*, 6139-6155.

126) Phalakornkul,J.K.; Gast,A.P.; Pecora,R. Rotational and Translational Dynamics of Rodlike Polymers: A Combined Transient Electric Birefringence and Dynamic Light Scattering Study. *Macromolecules* **1999**, *32*, 3122-3135.

127) Jamil,T.; Russo,P.S.; Negulescu,I.; Daly,W.H.; Schaefer,D.W.; Beaucage,G. Light scattering from random coils dispersed in a solution of rodlike polymers. *Macromolecules* **1994**, *27*, 171-178.

CHAPTER 4 CONSTRUCTION OF HOLOGRAPHIC FPR INSTRUMENT

Fluorescence Photobleaching Recovery (FPR) has been applied in many scientific and industrial fields. It is a very useful tool to monitor a molecule's diffusion in membranes,[1-7] dense systems (gels [8-13] and liquid crystals[14-17]) concentrated solutions[18] or mixtures of two or more solutes,[19-22] (rods, spheres, or their mixture). FPR has three main steps: exciting, bleaching and recovering. According to the styles of the bleaching patterns, two kinds of FPR are available: spot FPR [23;24] and fringe FPR.[25] Spot FPR is easier to operate but the results are not as accurate as the results from the fringe FPR because of the edge effect.[23] Koppel used multipoint scanning to reduce the uncertainty and insensitivity.[24] The periodic-pattern photobleaching was introduced by Smith and McConnell in 1978.[25] In their experiment the laser beam traveled through a Ronchi Ruling (RR, a glass with equal clear and black stripes) before it passed the microscope objective and finally reached the sample. Lanni and Ware improved the pattern photobleaching technique with modulation.[26] The RR was able to move at a constant speed with the help of a modified phonograph turntable. The RR FPR for our probe diffusion experiments is similar to Lanni's system, except that the RR was moved by the vibration of low-frequency loudspeakers. The holographic FPR under construction is also fringe FPR which the pattern is created by the interference of two crossed beams and the modulation is controlled by the electro-optic modulator (EOM).

The mixture of SiPCPs and PBLG can be very viscous even at low concentrations. Consequently, the diffusion of the probe particles is very slow. The RR FPR instrument being used in our experiments (details are in the next section) creates the fringe pattern by imaging a RR, which is not efficient in this situation. It is impossible to get a RR with a fringe pattern

narrower than one micrometer. A narrower down-to-nanometer fringe pattern is needed and a new holographic FPR instrument is being developed to satisfy such a specific condition. The major differences between the holographic FPR under construction and the RR FPR currently used are: 1) In holographic FPR, a spatial pattern is produced from the interference of two crossed beams as an alternative by illuminating a Ronchi Ruling in RR FPR;[27;28] 2) the oscillating pattern is generated by an EOM in holographic FPR instead of two opposing low-frequency loudspeakers that vibrate the Ronchi ruling back and forth; 3) a lock-in amplifier, which can detect weakly oscillating signals, is employed in holographic FPR.

4.1 Ronchi Ruling (RR) FPR

Figure 4.1 is the schematic of Ronchi Ruling FPR instrument currently being used. As Laser beam at 488 nm supplied by an Innova 90 passes an acousto-optic modulator (AOM, made by NEOS Inc., detail is in next paragraph) where the laser beam is split, and all other diffracted beams, except the first-order diffracted beam, are blocked by a pin hole. The AOM alternates the first-order diffractive beam at low intensity for reading or at high intensity (2000 times stronger than low intensity) for bleaching. After the beam is detoured by two mirrors (mirror 1 and 2), it passes the Ronchi Ruling that is located between the two low-frequency speakers. The speakers can create vibrations with the desired frequency. Finally, the beam is reflected from a dichroic mirror, illuminates the sample, and goes through a microscope objective.

The illuminated fluorescent light ($\lambda = 514.5$ nm) enters the photomultiplier tube (PMT) by passing through the dichroic mirror and a shutter. The signal generated from PMT is fed to a Low Noise preamplifier (Stanford Research Systems, Model SR560), followed with an amplifier built by the LSU electronic shop. The signal from the amplifier is transferred to an analog-digital card

(National Instruments, #AT-MIO-16D Part #320489-01) which communicates with a computer through LabView 6.0 software.

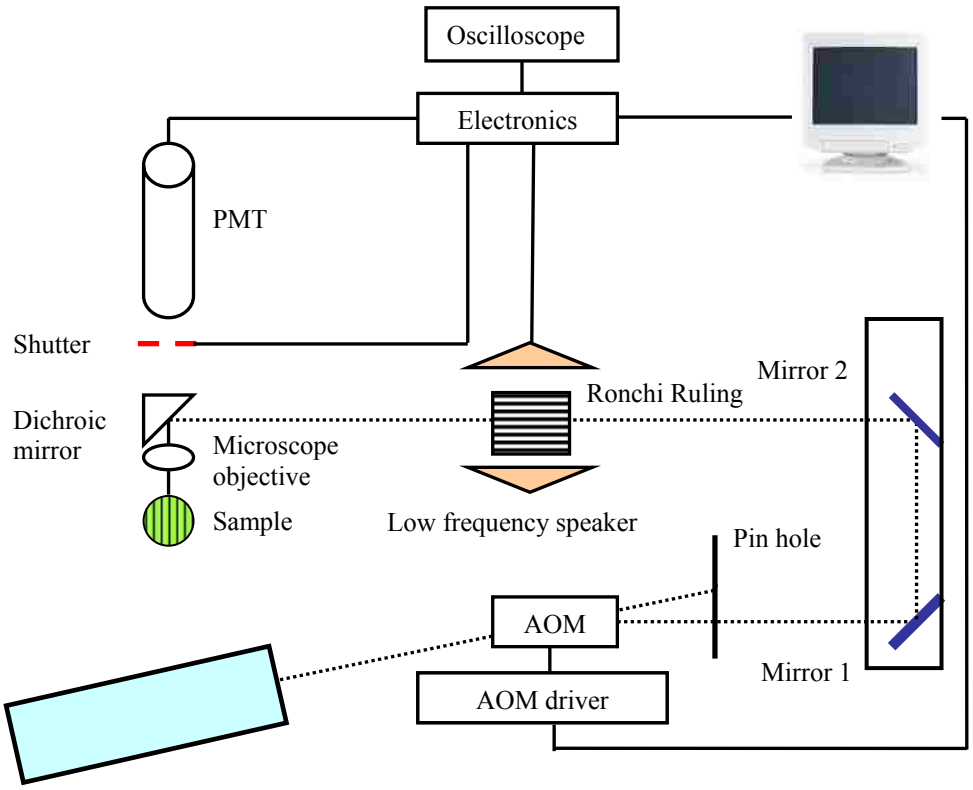

Figure 4.1 Schematic graph of RR FPR instrument. (Adapted from Refs. 29 and 30, Dotted line is the light path.)

An oscilloscope is connected with a preamplifier that is used to monitor the sinusoidal wave generated. Finally, the signal is translated to a DC voltage that represents the contrast of the pattern, *C*. The diffusion coefficient of a sample can be calculated by equations 4.1 to 4.3

$$C(t) = B + Ae^{(-\Gamma t)} \qquad \text{equation 4.1}$$

$$\Gamma = D_s K^2 \qquad \text{equation 4.2}$$

$$K = 2\pi/L \qquad \text{equation 4.3}$$

where B is the baseline, t is the time since photobleaching has occurred; Γ is the decay rate (reciprocal of decay time); D_s is the self diffusion coefficient; L is the repeat pattern in the sample, and it is determined by the number of stripes of Ronchi Ruling and the objective; K is a spatial frequency which depends on L. It is difficult to make RR with very fine lines. The finest one available in our lab is 200 lines/in, with 10 X objective the L could be as small as 12 μm.

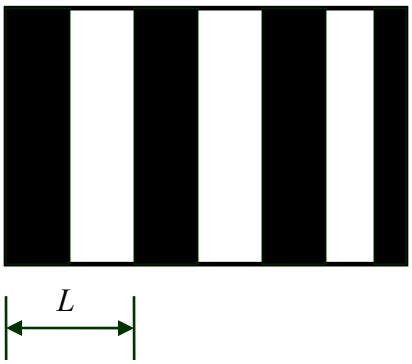

Figure 4.2 Scheme of the Ronchi Ruling pattern on sample

The AOM in Figure 4.1 is also called a Bragg cell. It is a piece of transparent material (e.g., glass) with an attached piezoelectric transducer. This piezoelectric transducer is driven by an RF signal source, and it can produce acoustic waves in the glass. The acoustic wave generates a moving spatially periodic variation of index of refraction in the glass, which can be treated as moving planes of compression (with a higher refractive index) and extension (with a lower refractive index). The incident light is diffracted by these planes just like Bragg diffraction in crystals. For Bragg diffraction, the atomic plane is stationary, whereas for acousto-optic diffraction, the acoustic wave planes travel at the speed of sound. A laser beam passes through the AOM, which is adjusted to diffract about 85-90% intensity of the incident light into the 1st order diffracted beam. The pin hole blocks all other diffracted beams except for the 1st order one.

The 1st order diffracted light in "phase" (agrees with the Bragg diffraction condition) is used for breaking the chemical bond of the florescent dye attached with the sample particles and the thousands-time-weaker intensity (out of "phase") beam light that is for reading. A shutter is necessary for protecting PMT in the bleaching processor.

4.2 Holographic FPR

Figure 4.3 is the schematic graph of the holographic FPR. Similar to RR FPR, the laser light supplied by Lexel model 95 passes through AOM (NEOS 35085-3). With the help of AOM, the laser beam is able to be high intensity for bleaching and low intensity for reading. The AOM is connected with the AOM driver (NEOS modal N38085-6DS) which is controlled by the LabView 8.1 program through data acquisition (DA board, NI USB-6221). The laser beam is split to beam1 and beam 2 after it is detoured by mirror 1 and passes through a beam splitter. Beam 1 passes through the beam splitter and then is reflected by mirror 2. Beam 2 is reflected by the beam splitter and then goes through EOM (Con Optics M302), which controls the phase change of beam 2 (detail is in the EOM section). The two beams meet each other at a sample cell. The signal is collected by PM (photosensor modules H7826, brand: Hamamatsu) and sent to lock in amplifier (SR850 DSP (digital signal processing)), which distinguishes the weak signal from noise (detail is in lock in amplifier section); finally the noise-eliminated signal goes to the computer where the data are processed.

The wideness of a pair of dark-bright lines of the interface pattern (d, it is L in RR FPR) from beam 1 and beam 2 can be calculated by using equation 4.4.[27]

$$d = \frac{2\pi}{q} = \frac{\lambda}{2\sin(\theta/2)} \qquad \text{equation 4.4}$$

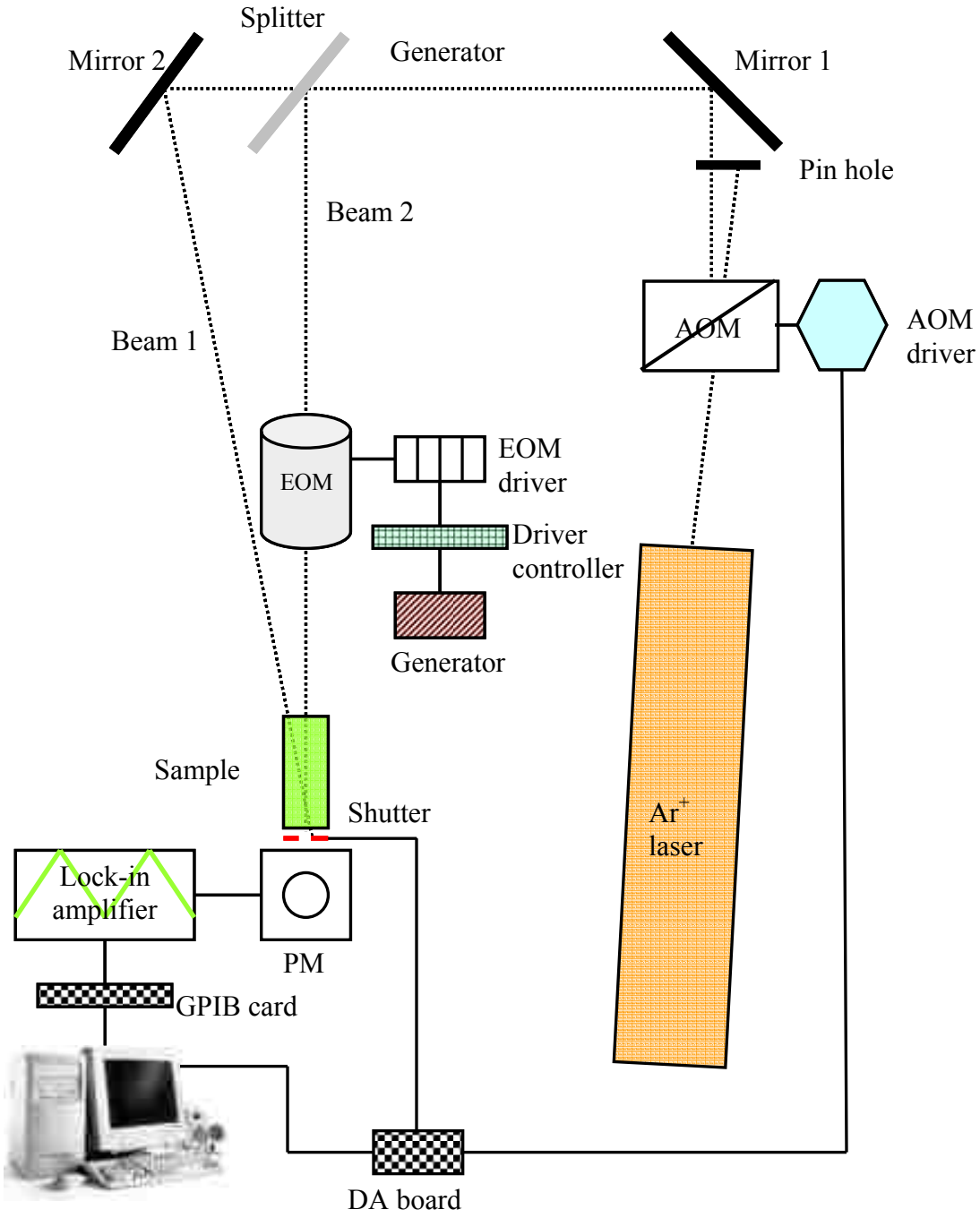

Figure 4.3 Schematic graph of holographic FPR. Dotted line is the light path

where λ is the wavelength of the laser beam, (λ = 488 nm in this setup); θ is the angle between two cross beams, and d can be varied by adjusting θ. If the θ is 60°, the d is 488 nm, which is almost 1/25 of the repeat pattern of RR FPR with 200 lines/in RR and 10X objective. This means this holographic FPR (θ = 60°) can measure the recovery more than six hundred times faster.

Figure 4.4 is the picture of the interfere pattern of our holographic FPR. The sample is FITC labeled gelatin, and here the angle θ is about 0.5 ^{o}. The black dots are dust. The extreme small angle is chosen just for alignment and taking a picture. In real experiments, the angle should be much larger than this.

4. 2.1 Electro-Optic Modular (EOM)

The Linear Electro-Optic Effect (LEOE) lets the EOM act to change phase. LEOE was first described by F. Pockels in 1906. It occurs in crystals lacking a symmetric center, such as lithium niobate or gallium aresnide. These kinds of crystals slightly change the refractive index when subjected to an alterable electronic field and the small change is enough to change the spatial-phase condition of in-coming light. In order to use this effect, the EOM is rotated, rolled and tilted to make sure the incident light propagates through the crystal in the direction that is normal with respect to the direction that the reflective index can change. Figure 4.5 gives the scheme of the EOM. Beams A and B are the outgoing beams before and after the electronic field is switched. In this set-up, the EOM is connected with the EOM driver, which is also linked to a controller (Con Optics M302). The J1 and J2 plugs of the driver connect with the EOM and the J3 plug connects with the function generator (Heath 1274). The function generator manages the frequency of the electronic field, and consequently manages the frequency of the phase change of the outgoing light. The LabView software can also be used to generate a wave signal besides the function generator.

LabView sends the wave signal to a DA (data acquisition) board. By connecting the DA board with the J3 plug of the EOM driver, the wave signal is able to be delivered to EOM.

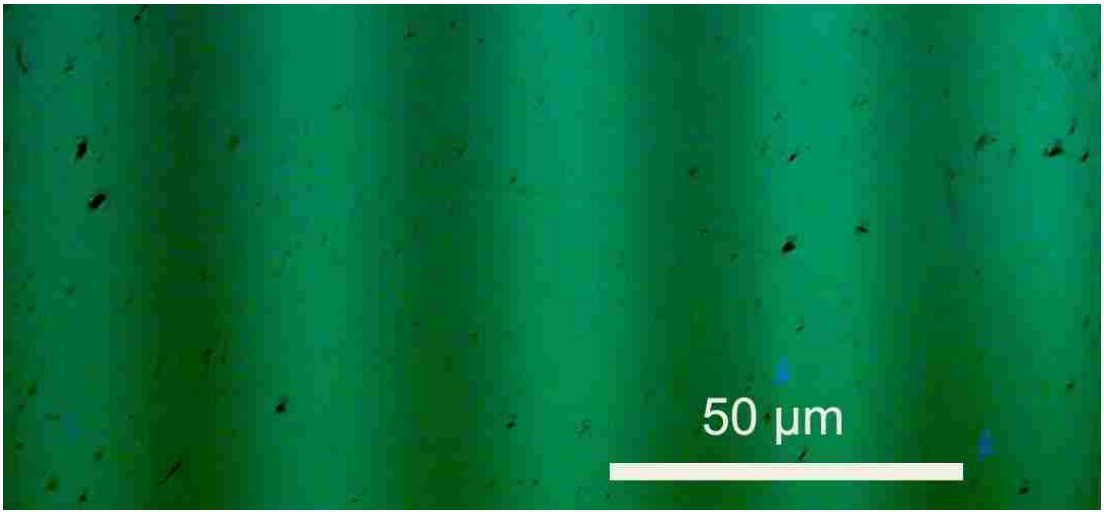

Figure 4.4 The pattern of interference of two crossed-beams at about 0.5 ^{o}.

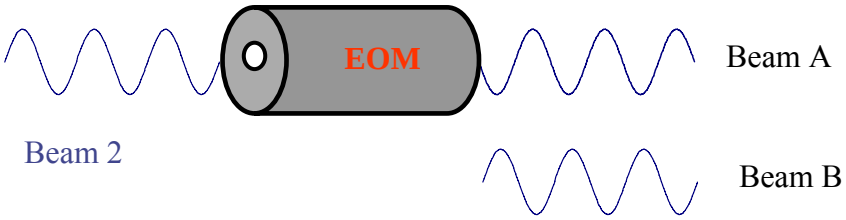

Figure 4.5 Scheme of EOM.

Since our laser source is polarized, EOM can be adjusted by following three steps: 1) Turn on the laser, let the laser pass through EOM; 2) Put a polarizer before EOM, adjust the polarizer to make sure there is no light going through the polarizer; 3) Put the same polarizer after the EOM and adjust the EOM to make sure there is no light passing through the polarizer.

4.2.2 Lock-in Amplifier

A lock-in amplifier is employed to detect weakly oscillating signals. The lock-in amplifier filters the noise from the real signal based on the frequency, not the intensity. Picture 4.6 is a picture of the SR850 DSP amplifier. “Reference in” plug is connected with a function generator or DA board when a wave signal is generated from the LabView software. “Signal in” plug is connected with PM, and “signal out” plug joins with the oscilloscope if necessary. The amplifier is connected with the computer through GPIB card. All functions of the lock-in amplifier can be executed by computer through the LabView software. The software of the SR850 DSP amplifier is available to download from NI.com and can be customized. Figure 4.7 is the front panel of SR850 DSP on the computer.

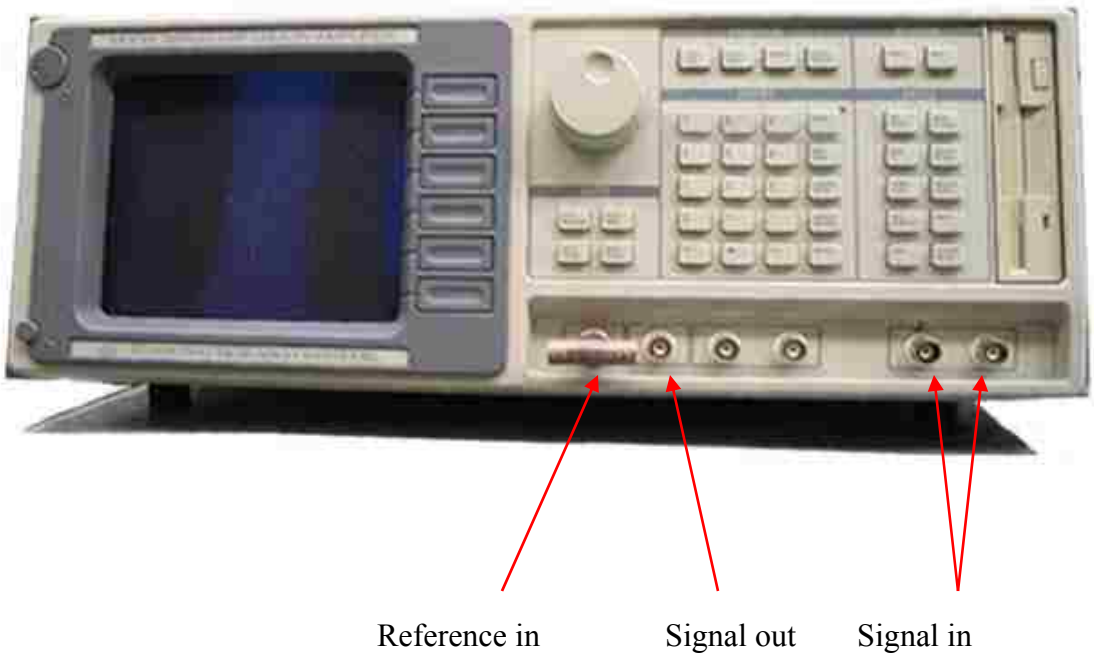

Figure 4.6 Picture of model SR850 DSP Lock-in amplifier.

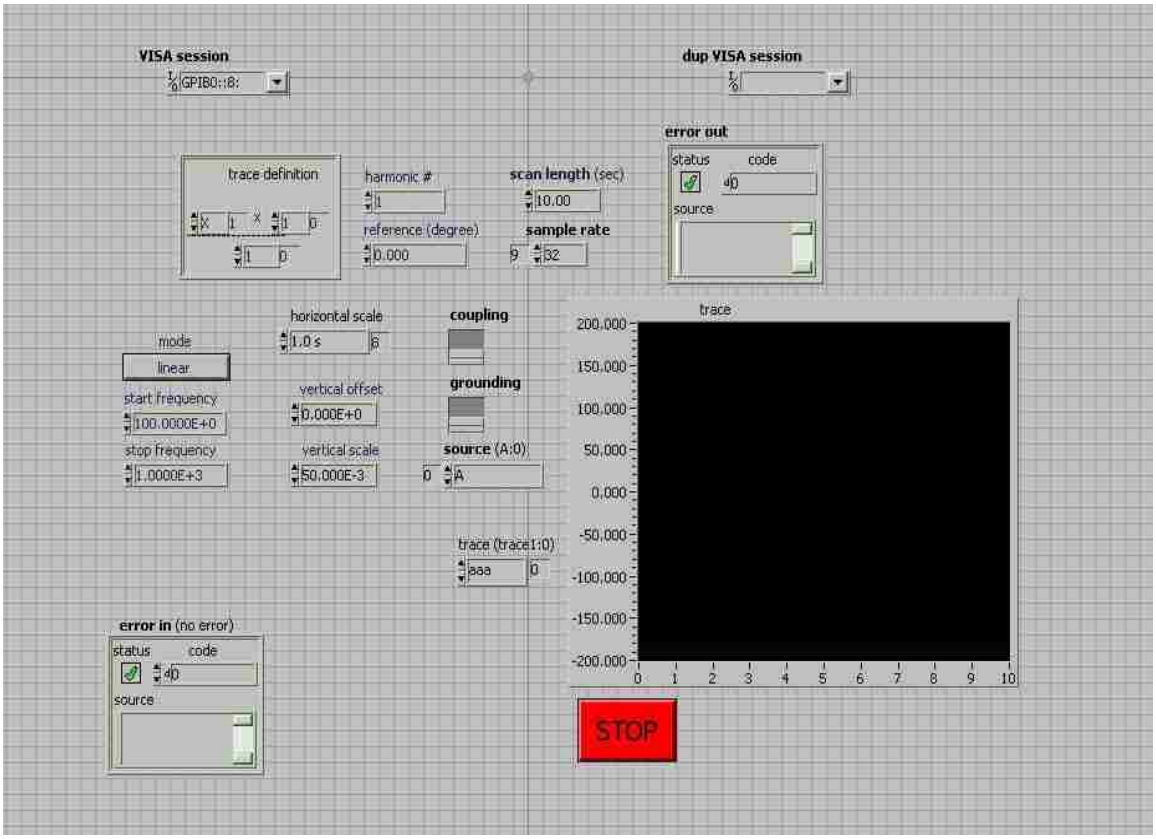

Figure 4.7 The front panel of lock-in amplifier on computer

4.2.3 Controlling AOM, PM and Shutter

Acousto-optic modulator (AOM), photosensor modules (PM), and shutter (powered by Heath 2718) can also be controlled through LabView. Shutter and PM are connected with the DA board (detail see Figure 4.11). When the "AOM on" is chosen for bleaching, the shutter is automatically closed to protect the PM; while in the reading process, the AOM is off, the shutter is opened and the illuminated signal is able to be send to PM. Figure 4. 8 is the front panel of shutter/AOM control testing (program "05 Collecting while sawtoothing-stand alone.vi"). One is highly recommended to do this test before running a real experiment.

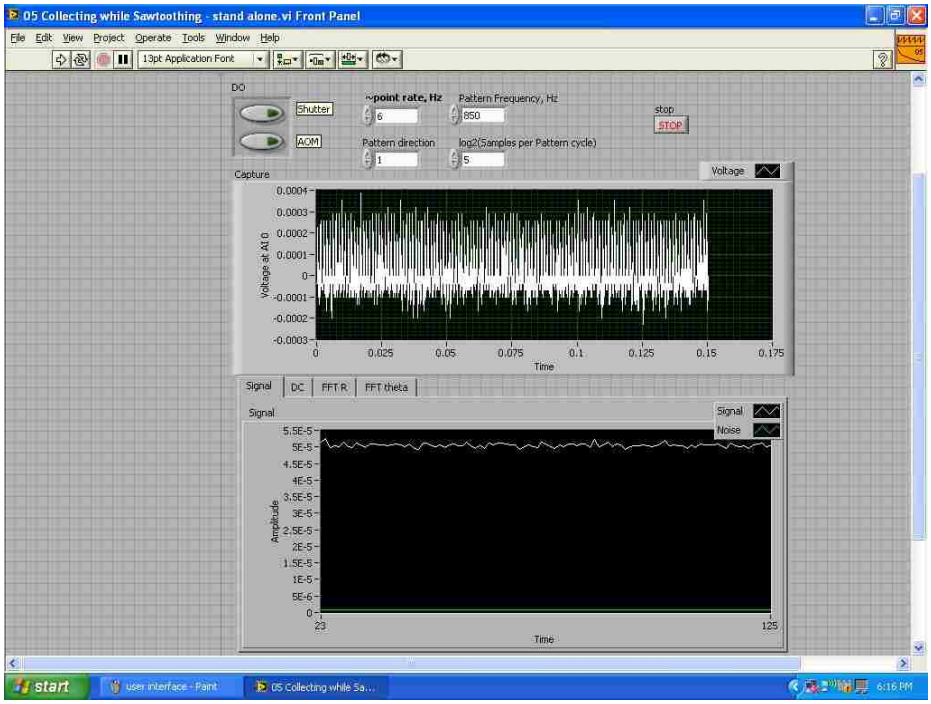

Figure 4.8 The front panel of testing program for controlling shutter and AOM.

Figure 4.9 is the picture of the shutter and PM. They are located in a customized aluminum case. In RR FPR, the microscope used a fairly high N.A. objective, which helps to collect the signal, and the PM is located above the image. The PM (H7826 modal) for holographic FPR has a much smaller size, and the optical fiber bundle was used to feed the signal to PM (see picture 4.10).

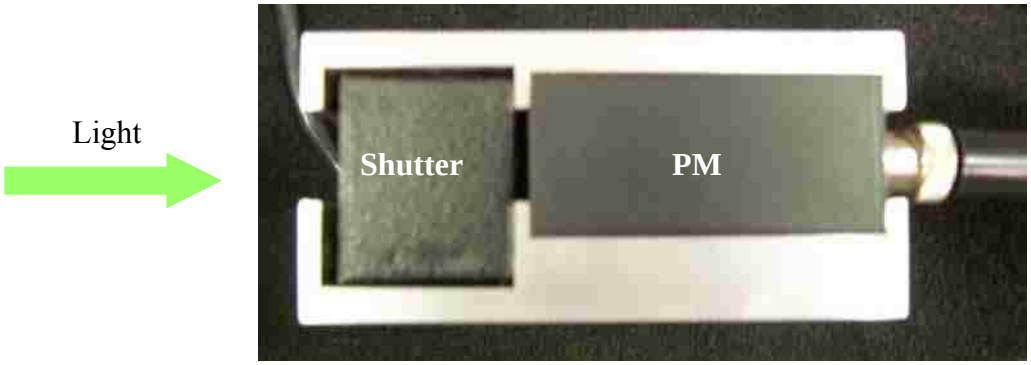

Figure 4.9 Picture of shutter and PM.

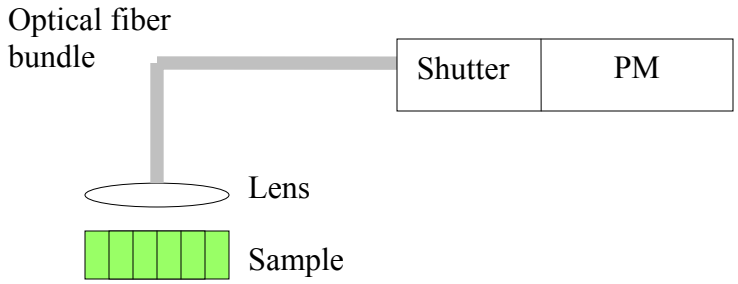

Figure 4.10 Scheme of collecting signal and feeding to PMT.

Figure 4.11 is scheme of the DA board pin structure. It gives the information on how the computer communicates with the AOM, shutter, PMT, etc.

	#66 to ground			#94 to (-) of shutter power supply
# 65 to shutter controller	#66 to AOM Modulator			
#1 to PM	#3 to PM		#16 to EOM driver	

Figure 4.11 DA board pin structure

4.2.4 Pictures of the Set-Up

Below are pictures of the holographic FPR. There are some optional modifications which are discussed in section 4.2.6. Figure 4.12 is the picture of the whole set-up. The picture is taken from the opposite side as the sample is located. Microscope is used to check the interference pattern.

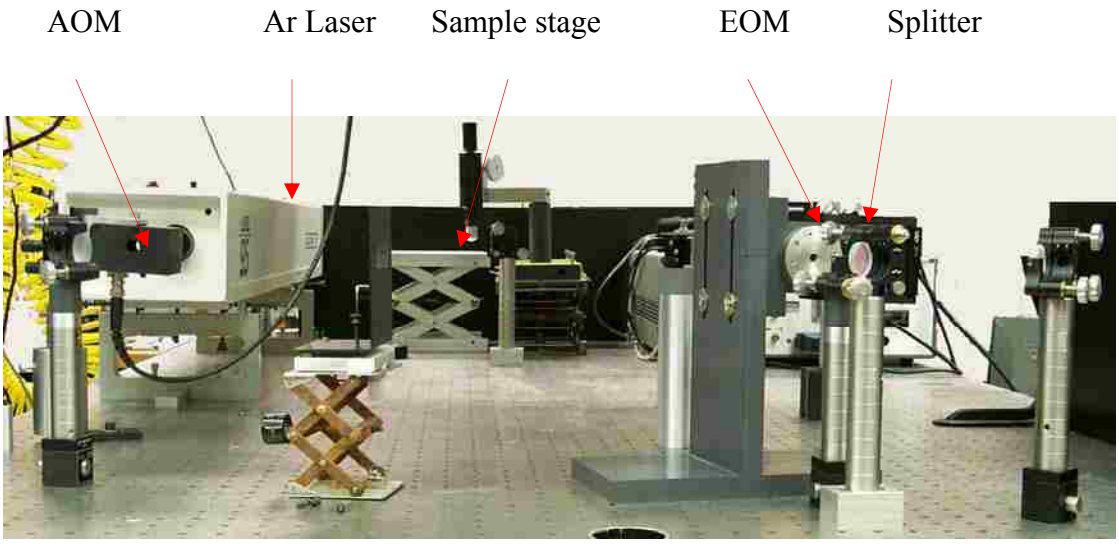

Figure 4.12 Picture of set-up of holographic FPR.

Figure 4.13 is the close-up picture of AOM. The pinhole is used to block all diffractive beams except the 1st one.

Figure 4.13 Close view of AOM, pinhole and mirror.

4.2.5 Run Experiments with LabView

The Labview program was obtained with a big contribution from Dr. Grigor Bantchev. After the testing of the shutter and PMT has been done, one can start the measurement. The main program is "00hFPR GB.vi", which has the front panel, as Figure 4.14 shows. Three values are collected: signal, stage and noise. The signal is a DC signal and it indicates the contrast. "Stage" here means the 3 steps of "prebleach, bleach, and recovery". Click the star key " ⇒ " on the top (the key in red cysle), the "20 users input .vi" window will pop up as Figure 4.15 presents. In this subvi, one is able to choose the time range for prebleach, bleach and recovery, the address to save the data, the pattern frequency, the point rate, and the number of testing per pattern cycle. There are two choices to save data, "save all data points" and "save compressed data points". "Save compressed data points" function uses less space for storing data, and it is very useful when the experiment needs a long recovery stage. Click the "ready, start" button when it is ready. The data are save as .txt file, and one needs transfer the data to the Excel file and analyze the data with the Excel program.

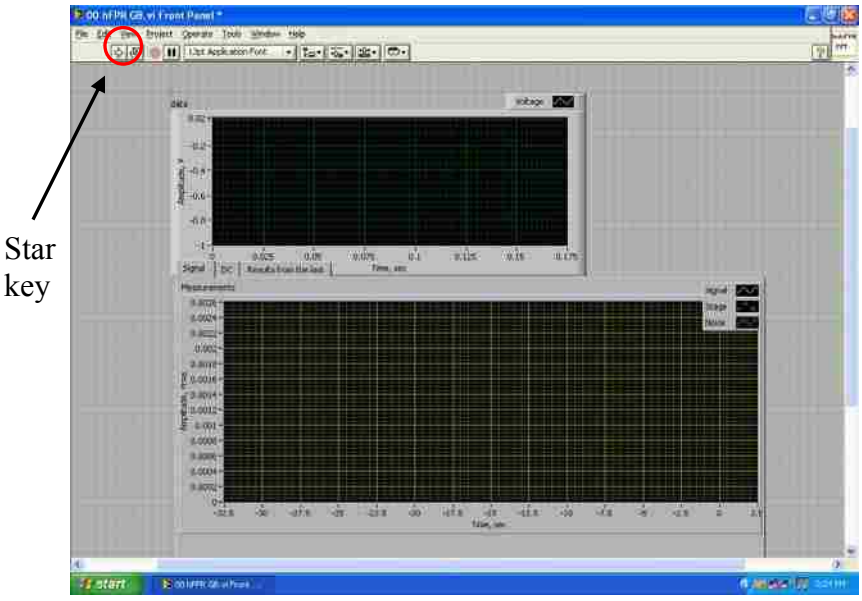

Figure 4.14 Front panel of the main program.

4.2.6 Some Optional Modifications

The voltage controller of PMT: The working voltage for PMT is 11.5 -15.5 V, and one can add one voltage control for PMT in order to get optimum working power. The controller basically is an adjustable resistance with 0-100K Ω.

Intensity filter: Beam 1 and beam 2 may not have same intensity after one goes through EOM and the other is reflected by mirror 2. An intensity filter can be used to make the two beams are the same strength before they meet at the sample cell.

Concave lens: Strong laser beams are required for the bleaching step and a concave lens helps to maximize the intensity of the laser beams. A concave lens placed before EOM can converge the wide light before it enters the EOM.

More mirrors and pinholes: Since the laser is not perfect, more mirrors are used to prolong the light path and separate the stray light which has a wavelength beyond 488 nm. Pinholes are then applied to stop these stray lights and pass only beams with 488 nm.

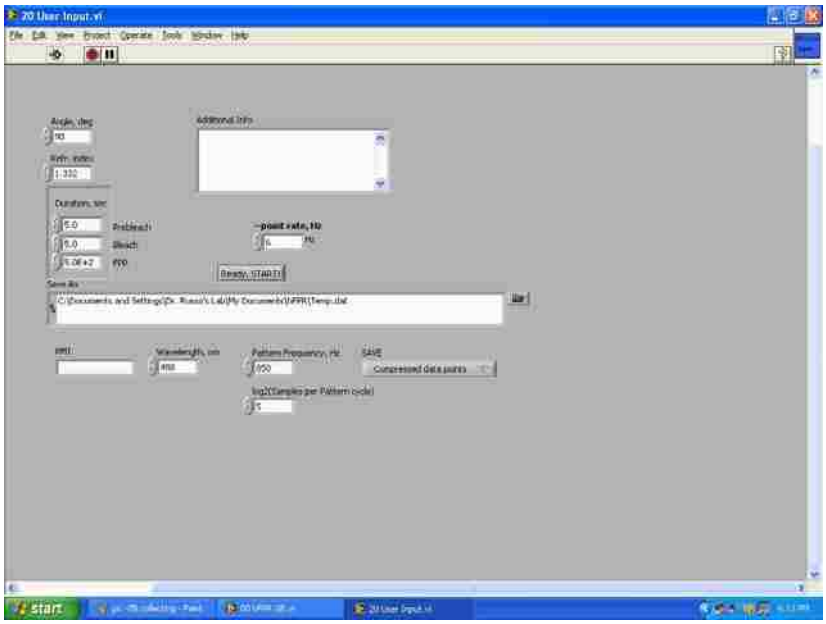

Figure 4.15 The pop up window of "20 user input.vi".

4.3 Conclusions and Future Work

In this chapter, the construction of a holographic FPR was described. The holographic FPR takes advantage of the interference of two cross beams to get a fine grating which can be as narrow as the wave length of the incoming laser. The set-up and the LabView software controlling the lock-in amplifier were explained. Some optional modifications of the system were also presented.

In order to test the system, bleaching the sample is necessary. In this holographic FPR, the intensity of laser beam "hitting" the sample is weaker than the one in RR FPR. In RR FPR, the laser light passes through an objective before it meets the sample. Therefore, placing convex lenses in front of the sample (let the beams pass the lenses before they reach the sample) may solve the problem. Meanwhile, we placed a an RR pattern in front of the sample and tried to use the single beam (by blocking one of the two beams) of holographic FPR to bleach the RR pattern on the sample. The bleached pattern was observed when the RR pattern was large, e.g., 50 lines/in, and this bleaching procedure could not achieved when small patterns like 200 lines/in were used. This phenomenon may be due to vibration. A solution can lie in acquiring a better air floats system for the table and covering the whole system with a heavy case.

The program is still not perfect; some improvements such as simplifying the reading and analyzing process are also anticipated.

4.4 References

1) Szyk,L.; Schaaf,P.; Gergely,C.; Voegel,J.C.; Tinland,B. Lateral Mobility of Proteins Adsorbed on or Embedded in Polyelectrolyte Multilayers. *Langmuir* **2001**, *17*, 6248-6253.

2) Tanaka,K.; Yu,H. Polymer-modulated, diffusion-controlled enzyme kinetics on monolayers. *ACS Symposium Series* **2003**, *840*, 57-64.

3) Verkman,A.S. Diffusion in cells measured by fluorescence recovery after photobleaching. *Methods in Enzymology* **2003**, *360*, 635-648.

4) Yang,Z.; Galloway,J.A.; Yu,H. Protein Interactions with Poly(ethylene glycol) Self-Assembled Monolayers on Glass Substrates: Diffusion and Adsorption. *Langmuir* **1999**, *15*, 8405-8411.

5) Mullineaux,C.W. FRAP analysis of photosynthetic membranes. *Journal of Experimental Botany* **2004**, *55*, 1207-1211.

6) Richert,L.; Boulmedais,F.; Lavalle,P.; Mutterer,J.; Ferreux,E.; Decher,G.; Schaaf,P.; Voegel,J.C.; Picart,C. Improvement of stability and cell adhesion properties of polyelectrolyte multilayer films by chemical cross-linking. *Biomacromolecules* **2004**, *5*, 284-294.

7) Tseng,K.C.; Turro,N.J.; Durning,C.J. Tracer diffusion in thin polystyrene films. *Polymer* **2000**, *41*, 4751-4755.

8) Mustafa,M.B.; Tipton,D.; Russo,P.S. Temperature ramped fluorescence photobleaching recovery for the direct evaluation of thermoreversible gels. *Macromolecules* **1989**, *22*, 1500-1504.

9) Mustafa,M.B.; Russo,P.S. Dye diffusion in aqueous hydroxypropylcellulose solutions. *Polymer Preprints (American Chemical Society, Division of Polymer Chemistry)* **1990**, *31*, 580-581.

10) Weiss,A.M.; Saraidarov,T.; Reisfeld,R. Confocal microscopy for characterization of porous sol-gel glasses incorporating luminescent dyes. *Optical Materials (Amsterdam, Netherlands)* **2001**, *16*, 15-20.

11) De Smedt,S.C.; Meyvis,T.K.L.; Demeester,J.; Van Oostveldt,P.; Blonk,J.C.G.; Hennink,W.E. Diffusion of Macromolecules in Dextran Methacrylate Solutions and Gels As Studied by Confocal Scanning Laser Microscopy. *Macromolecules* **1997**, *30*, 4863-4870.

12) Tinland,B.; Pernnodet,N.; Weill,G. Field and pore size dependence of the electrophoretic mobility of DNA: a combination of fluorescence recovery after photobleaching and electric birefringence measurements. *Electrophoresis* **1996**, *17*, 1046-1051.

13) Johnson,E.M.; Berk,D.A.; Jain,R.K.; Deen,W.M. Hindered diffusion in agarose gels: test of effective medium model. *Biophysical Journal* **1996**, *70*, 1017-1026.

14) Russo,P.S.; Baylis,M.; Bu,Z.; Stryjewski,W.; Doucet,G.; Temyanko,E.; Tipton,D. Self-diffusion of a semiflexible polymer measured across the lyotropic liquid-crystalline-phase boundary. *Journal of Chemical Physics* **1999**, *111*, 1746-1752.

15) Cush,R.C.; Russo,P.S. Self-Diffusion of a Rodlike Virus in the Isotropic Phase. *Macromolecules* **2002**, *35*, 8659-8662.

16) Mustafa,M.B.; Tipton,D.L.; Barkley,M.D.; Russo,P.S.; Blum,F.D. Dye diffusion in isotropic and liquid-crystalline aqueous (hydroxypropyl)cellulose. *Macromolecules* **1993**, *26*, 370-378.

17) Constantin,D.; Oswald,P. Diffusion coefficients in a lamellar lyotropic phase: Evidence for defects connecting the surfactant structure. *Physical Review Letters* **2000**, *85*, 4297-4300.

18) Yang,Z.; Underwood,S.M.; Yu,H. PMMA nanoparticle diffusion: Dependence on colloidal phase composition. *Polymeric Materials Science and Engineering* **1995**, *73*, 107-108.

19) Kluijtmans,S.G.J.M.; Philipse,A.P. First in Situ Determination of Confined Brownian Tracer Motion in Dense Random Sphere Packings. *Langmuir* **1999**, *15*, 1896-1898.

20) Imhof,A.; Dhont,J.K.G. Phase behavior and long-time self-diffusion in a binary hard sphere dispersion. *Colloids and Surfaces, A: Physicochemical and Engineering Aspects* **1997**, *122*, 53-61.

21) Kluijtmans,S.G.J.M.; Koenderink,G.H.; Philipse,A.P. Self-diffusion and sedimentation of tracer spheres in (semi)dilute dispersions of rigid colloidal rods. *Physical Review E: Statistical Physics, Plasmas, Fluids, and Related Interdisciplinary Topics* **2000**, *61*, 626-636.

22) Michel,E.; Cipelletti,L.; d'Humieres,E.; Gambin,Y.; Urbach,W.; Porte,G.; Appell,J. Self-diffusion and collective diffusion in a model viscoelastic system. *Physical Review E: Statistical, Nonlinear, and Soft Matter Physics* **2002**, *66*, 031402-1-031402/7.

23) Munnelly,H.M.; Roess,D.A.; Wade,W.F.; Barisas,B.G. Interferometric fringe fluorescence photobleaching recovery interrogates entire cell surfaces. *Biophysical Journal* **1998**, *75*, 1131-1138.

24) Koppel,D.E. Fluorescence redistribution after photobleaching. A new multipoint analysis of membrane translational dynamics. *Biophysical Journal* **1979**, *28*, 281-291.

25) Smith,B.A.; McConnell,H.M. Determination of molecular motion in membranes using periodic pattern photobleaching. *Proceedings of the National Academy of Sciences of the United States of America* **1978**, *75*, 2759-2763.

26) Lanni,F.; Ware,B.R. Modulation detection of fluorescence photobleaching recovery. *Review of Scientific Instruments* **1982**, *53*, 905-908.

27) Cicerone,M.T.; Blackburn,F.R.; Ediger,M.D. Anomalous Diffusion of Probe Molecules in Polystyrene: Evidence for Spatially Heterogeneous Segmental Dynamics. *Macromolecules* **1995**, *28*, 8224-8232.

28) Davoust,J.; Devaux,P.F.; Leger,L. Fringe pattern photobleaching, a new method for the measurement of transport coefficients of biological macromolecules. *EMBO journal* **1982**, *1*, 1233-1238.

29) Bu,Z.; Russo,P.S. Diffusion of Dextran in Aqueous (Hydroxypropyl)cellulose. *Macromolecules* **1994**, *27*, 1187-1194.

30) Garrett John Doucet. Dynamics of complex polymer solutions: Putting diffusion to work and exploring rigid rod diffusion. 2004.

CHAPTER 5 CHARACTERIZATION OF COBALT MAGNETIC NANOPARTICLES

5.1 Magnetism and Magnetic Particles

5.1.1 Introduction of Magnetism

Even though, the first magnetism experiment was reported 200 years ago, the history of magnetic materials is more than 2500 years old. Oersted and Sturgeon discovered in the 1800's that electricity and magnetism are related. Overall, magnetic force is generated from the movement of electron(s). Such movement can arise from the motion of electrons in an electric current, resulting "electromagnetism", or it can be from the quantum-mechanical spin and orbital motion of electrons, leading to "permanent magnets". The Biot-Savart law (equation 5.1) describes the relationship between the differential elements of current and the corresponding magnetic field.

$$d\mathbf{B} = K_m \frac{Id\mathbf{l} \times \hat{r}}{r^2} \qquad \text{equation 5.1}$$

Here, $d\mathbf{B}$ is the differential element of the magnetic field; I is the current; $d\mathbf{l}$ the differential length vector of the current element; $\hat{r}$ is the unit displacement vector from the current element to the field point; r is the distance from the current element to the field point; K_m is a constant which is defined as $K_m = \mu_0 / 4\pi$, and μ_0 is the magnetic constant (explained further in the following graph). A responding magnetic field called magnetization (M) is produced when a magnetic or electric field (called applied field H) is applied to a material. The magnetic susceptibility (χ) is a unitless parameter which demonstrates the response of the material to an applied magnetic field.

$$\chi = \frac{M}{H} \qquad \text{equation 5.2}$$

The magnetic induction, also called magnetic flux density B, is the total amount of the magnetic flux through the unit area of a section, which is perpendicular to the direction of the flux. Equation 5.3 describes the dependence of *B*, *H,* and *M* in a centimeter-gram-second system (CGS).

$$B = H + 4\pi M \qquad \text{equation 5.3}$$

In equation 5.3, the unit for *B* is Gauss (G), Oersted (Oe) for *H*, and emu/cm^3 for *M*. Magnetic permeability (μ) represents how easily the material can be magnetized. It is defined as the proportionality between magnetic induction *B* and magnetic field *H* (equation 5.4). In the SI unit system, magnetic permeability in vacuum (μ_0) is approximately 1.257 x 10^{-6} Henry per meter (H/m or m.kg.A^{-2}.sec^{-2}). Different types of magnetic material show different magnetic permeability behaviors, e.g., diamagnetic material decreases the magnetic flux density, paramagnetic material concentrates the magnetic flux more than one but less than ten times, while ferromagnetic materials intensify the magnetic flux by a factor of ten or more. For some materials, the permeability factor varies with the temperature and the intensity of applied field.

$$B = \mu H = \mu_0 (H + M) = \mu_0 (1 + \chi) H \qquad \text{equation 5.4}$$

Here (SI unit system) the unit for *B* is tesla (T), A/m for *H* and *M*. In engineering applications, relative permeability (μ_r), a unitless constant defined as the ratio of permeability of a specific medium to the permeability of vacuum, is often mentioned.

$$\mu_r = \mu \big/ \mu_0 \qquad \text{equation 5.5}$$

The spin motion of the electrons in a material creates a magnetic field. When an external magnetic field is applied, the motion of the electrons tends to be aligned in such a way that the

created magnetic field is in an opposite direction from the external magnetic field. This is called diamagnetism. Depending on the behavior of the material after the release of the external magnetic field, the material can be distinguished as paramagnetic or ferromagnetic. For paramagnetic material, the magnetization is proportional to the external magnetic field and there is not any magnetization retained after the external magnetic field is released. As a contrast, ferromagnetic material such as iron, nickel, and cobalt tends to “memorize” and keep the ordering. This tendency of "remembering the magnetic history" is so called hysteresis. Magnetic hysteresis is a phenomenon that a magnetic material can’t relax back to zero magnetization even if the magnetic field is removed. In order to get zero magnetization, the opposite-direction magnetic field is needed.

Figure 5.1 shows the typical hysteresis loop for ferromagnetic material. The magnetization starts from point “s”, and reaches a maximum at point “a”. At point “a” all of the magnetic domains are aligned and the material reaches the magnetic saturation. Then, the magnetic field is reduced to zero (point “b”) and there is still some magnetization remaining. The value at point “b” is called retentivity; it indicates the remaining magnetization. At point “c”, the magnetic field H has been reversed and the magnetic induction B is reduced to zero. The negative value of H is called coactivity. The material becomes magnetically saturated at negative direction (compare with point “a”) at point “d”. Then the reversed magnetic field is reduced to zero (point “e”), the material has remaining magnetization the same as at point “c” but with contrary direction. Finally, the magnetization is increased in the positive direction to point “f” where the B returns back to zero. Material with a wide hysteresis loop is good for permanent magnets and memory devices, whereas the one with a narrow hysteresis loops is normally used for transformer and motor cores.

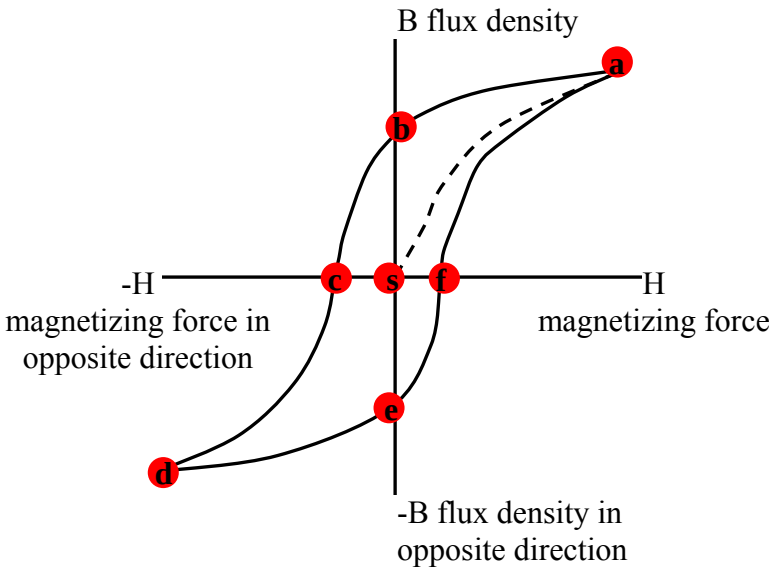

Figure 5.1 Hysteresis loop of a ferromagnetic material.

The magnetic domain is the region in which all of the atomic dipoles are coupled together in a preferential direction. For ferromagnetic material, each domain has a high degree of magnetization, even though the bulk material doesn't show any sign of magnetism without any external magnetic field because domains are randomly oriented to each other. When an external magnetic field is applied, magnetic domains within the material are aligned, and the more domains are aligned, the stronger magnetization the material has. Figure 5.2 shows how domains respond to the applied magnetic field in the hysteresis loop.

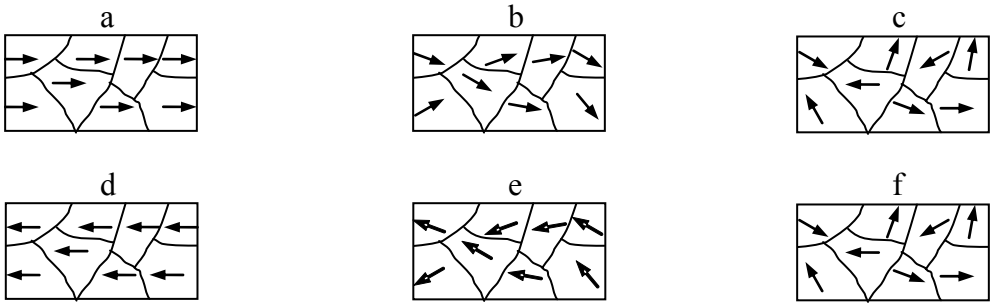

Figure 5.2 Scheme of domain behavior in hysteresis loop.

The alignment can be broken by increased temperature, and the net magnetization can also be reduced to zero at the Curie temperature. The Curie temperature indicates how much thermal energy is needed to break the long-range ordering in the material. Above the Curie point, the material is paramagnetic. Table 5.1 is the Curie temperature of some ferromagnetic materials.

Table 5.1 Curie temperature of some ferromagnetic materials[1;2]

Material	Curie temperature (K)
Fe	1043
Co	1388
Ni	627
Gd	293
CrO_2	387
Cu_2MnAl	630
Cu_2MnIn	500
Sr_2FeReO_6	500
Sr_2FeMoO_6	400-430

Superparamagnetism normally occurs in very small particles (1-10 nm) of material that would be ferromagnetic in bulk; The particle's behavior is similar to paramagnetism even though the temperature is far below the Curie temperature.

5.1.2 Magnetic Nanoparticles

Magnetic nanoparticles have been applied in many areas such drug delivery,[3-6] data storage,[7-10] biomedicine,[11-13] contrast enhancement in resonance imaging,[14;15] magnetic refrigeration systems[16], and catalysis.[17;18] In most of the applications, it is desirable for the

particles to be superparamagnets when the temperature is above the so-called blocking temperature, which is mainly affected by the particles' size. A large magnetic particle has a multidomain structure, and these domains are separated by domain walls. The formation of domain walls is dominated by the competition of magnetostatic energy (ΔE_{MS}) and domain wall energy (E_{dw}). Magnetostatic energy increases with domain size, while domain wall energy increases with more interfacial area between domains, which means E_{dw} increases with decreasing size. The critical diameter of a spherical particle is the size when the particle is as small as in a single domain state where $\Delta E_{MS} = E_{dw}$. Table 5.2 is the estimated critical (single domain) size for some spherical particles.[19] The critical diameter estimation is only valid for spherical and non-interacting particles. The anisotropic shape particles have a larger critical diameter.

Superparamagnetism can be considered as the behavior of particles with one or more isolated single small domains. The energy to hold the magnetic moment of the particle in a certain direction is called magnetic anisotropic energy. Meanwhile, the thermal energy (k_BT) of the particle fights the alignment. When the thermal energy exceeds the magnetic anisotropic energy, the magnetization can be easily turned over, and the temperature is called blocking temperature. Above the blocking temperature, a superparamagnetic material behaves like paramagnetic material.

ZFC and FC (zero field cooling and field cooling) are the simple ways to detect domain structure and interparticle coupling. Briefly, the sample is cooled down from room temperature with (FC) or without (ZFC) external magnetic field; then the sample is warmed up with an applied small magnetic field and magnetization is recorded at the same time. In the warming-up step of the ZFC experiment, the moments are aligned to the direction of the applied field, while

the thermal energy tries to break the ordering. For superparamagnetic material, the thermal energy overcomes the barrier height of magnetization at the blocking temperature. In other words, for superparamagnetic material, the magnetization reaches a maximum at the blocking temperature. The blocking temperature shifts to a higher temperature with increased interparticle interaction. FC data gives us the information about coupling between particles. With a small applied field, uncoupled particles present a large increase with temperature, while strongly coupled particles show a much smaller increase.[20-22]

Table 5.2 Estimated critical diameter for some spherical particles [19]

material	D_c (nm)
hcp Co	15
fcc Co	7
Fe	15
Ni	55
$SmCo_5$	750
Fe_3O_4	128

Figure 5.3 is the ZFC/FC curve for Co-SiO_2 nanoparticles without /with interaction. Figure 5.3.a shows the ZFC/FC (zero field cooled/field cooled) magnetization curve of dilute Co-oleic acid (for protection) particles without interaction. The low blocking temperature (about 90K) and the large increment of magnetization with decreased temperature in FC data reveal there is no interaction between these Co particles. The ZFC/FC magnetization of concentrated Co-oleic acid particles is presented in Figure 5.3.b. ZFC data show the blocking temperature is raised to around 250K and that there is only a little amount of increment in the FC magnetization cause. Both of these indicate a strong interaction between particles.

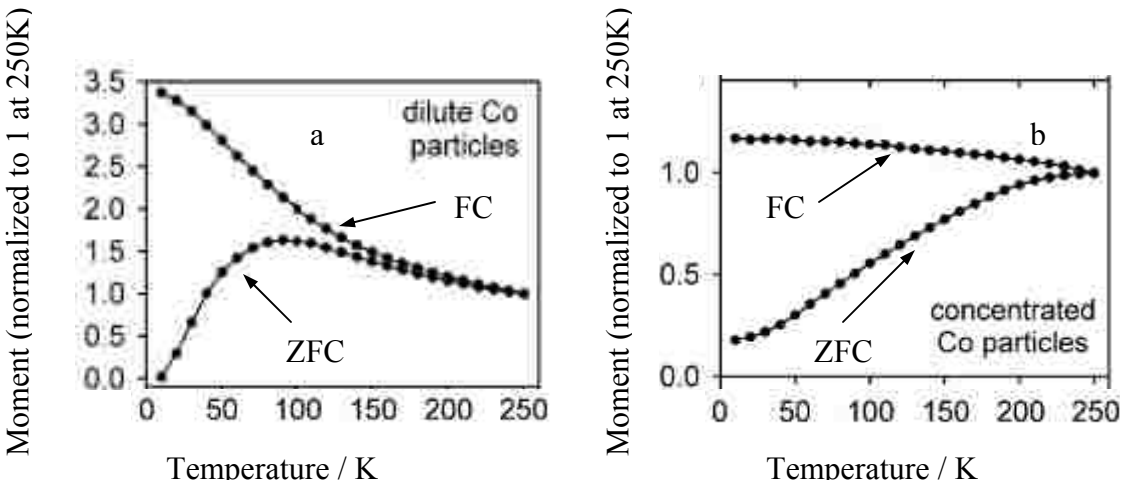

Figure 5.3 The ZFC/FC magnetization curve for Co-oleic acid (for protection) particles. a) Diluted particles in dodecane. There is no interaction between particles. b) Concentrated particles. The increased blocking temperature (around 250K) and much smaller increment of FC data with decreased temperature indicate the strong interaction between particles. (Copied from Ref. 21)

Decreasing particle size causes more surface anisotropy and more oxidized surface area. Thus, protective coating of the magnetic nanoparticles is crucial to the procedure. The coating material can be categorized as organic shell,[23-25] which includes surfactant, polymer, or inorganic shell[26;27] which has SiO_2, carbon, oxides of the bulk material of the particle, and precious metal (gold, platinum or silver).[28-31] Surfactant coating stabilizes the magnetic particles by electrostatic repulsion, whereas polymer coating takes advantage of steric repulsion. The choices of polymers for coating include poly(aniline), poly(alkylcyanoacrylates), poly(methylidene malonate), poly(pyrrole) poly(glutaraldehyde), poly(methacrylic acid) and poly(ethylene oxide),[32-37] etc. The organic coating could be damaged in an acid solution, organic solvent or high temperature. As the coating is usually a single or double layer, organic coating is not good for protecting very active magnetic nanoparticles. An inorganic coating normally forms a thicker "shell" to protect the magnetic metal nanoparticle "core". Forming an oxidation layer of core metal can be

achieved by exposing the particles to oxygen plasma[38] or utilizing a plasma-gas-condensation-type cluster deposition.[39] The key to such an approach is the controlling of the oxide thickness to get the best protection with the least loss of magnetization of the nanoparticles. Silica coating has been applied on Fe_2O_3,[40-42] iron,[43] cobalt,[27] and ferrofluids[44] and the coating can be achieved through Stöber or sol-gel method.[44-47] The thickness of the silica coating is adjustable by changing the concentration of ammonia and TEOS, and the silica "shell" can be functionalized for further purpose. The silica layer is porous so air or small molecules may diffuse throughout. Moreover, the layer is not stable in either a high- or low-pH solution.

In this dissertation, APS/TEOS (3-amino propyltrimethoxy/tetraethylorthosilicate) is used as a silica precursor for synthesizing silica-coated cobalt particles.[48;49] The silica shell is further functionalized with APS, which reacts with the NCA monomer; finally, the polypeptide-silica-cobalt composite particle is formed.

As discussed above, for the critical size of the magnetic nanoparticles, there are several important issues for the synthesis of magnetic particles: particle size and size distribution; crystallinity and crystal structure; and the shape of the particles and alignment. Competition between nucleation and growth determines the size of the product nanoparticle, while fast nucleation followed by slow growth is crucial for making monodisperse nanoparticles.[50] The two most popular preparation strategies are microemulsion synthesis at low temperature and thermal-decomposing organometallic compound [51-54] or metal salt[55] at high temperatures (100-300 ^{o}C).[56] The nanoparticles made from microemulsion synthesis have a relatively wide distribution of size, and the yield is low compared with other methods. By contrast, the thermal-decomposing method can have a well-controlled size /size distribution and relatively high yield.[51]

5.2 Experiments

5.2.1 Sample Preparation

5.2.1.1 Superparamagnetic Co Particles Coated with SiO_2 Shell

The synthesis of Co-SiO_2 was prepared by follwing the process of making gold-SiO_2 nanoparticles by Luis, *et al*.[48] Figure 5.2 is the scheme of synthesis Co-SiO_2 nano particles. The particles were provided by Erick Soto-Cantu.

5.2.1.2 PBLG Grafted Co-Sio_2 Nano Particles

The process is the same as preparing PBLG-grafted SiO_2 particles. For both Co-SiO_2 and PBLG-grafted Co-SiO_2 particles, magnetite was used to collect particles, while the centrifuge method was used for collecting Stöber spheres and SiPCPs.

5.2.2 Instruments

5.2.2.1 Applied Magnetic Field

Two kinds of magnetic field were used: the magnetic field from simple permanent magnets and the electric-magnetic field from a hand crafted solenoid. It is easy to control the magnetic field force and direction of the magnetic field by using solenoid. Figure 5.5 is the scheme of solenoid with a one-dimension magnetic field. The power supply is a 24 V battery; resistance varies from 0-100 Ω; the iron wire inserted is to increase the magnetic force; and there is a hole in the middle of the plate so the sample can be observed by a microscope.

5.2.2.2 Microscope

An Olympus polarizing microscope (model BHA) was used to observe the alignment and disorder of magnetic nano particles under a magnetic field. The sample was filled in a Vitrocom cell, and both ends of the cell were sealed. All experiments were under room temperature.

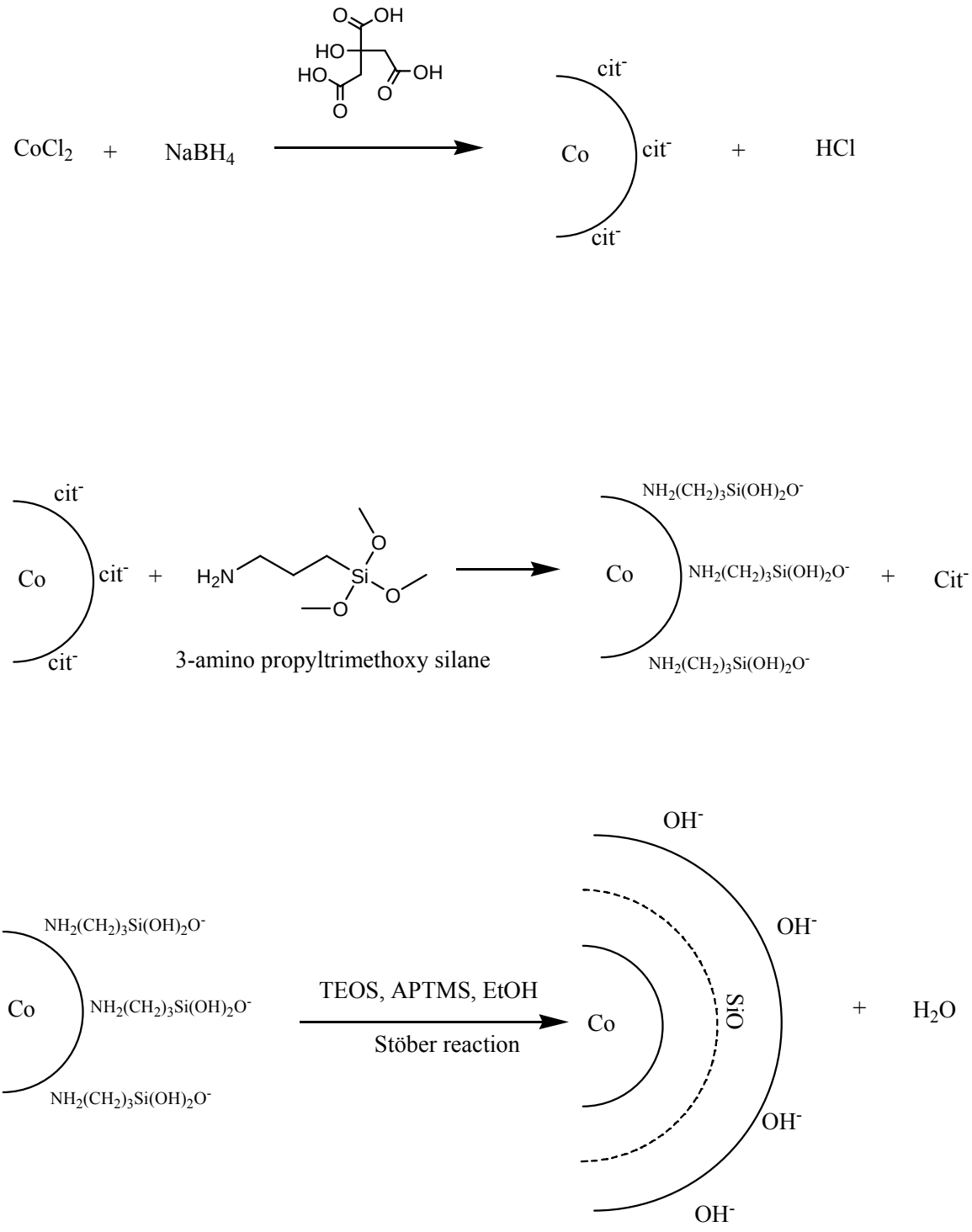

Figure 5.4 Scheme of synthesis of Co-SiO_2 nano particles.

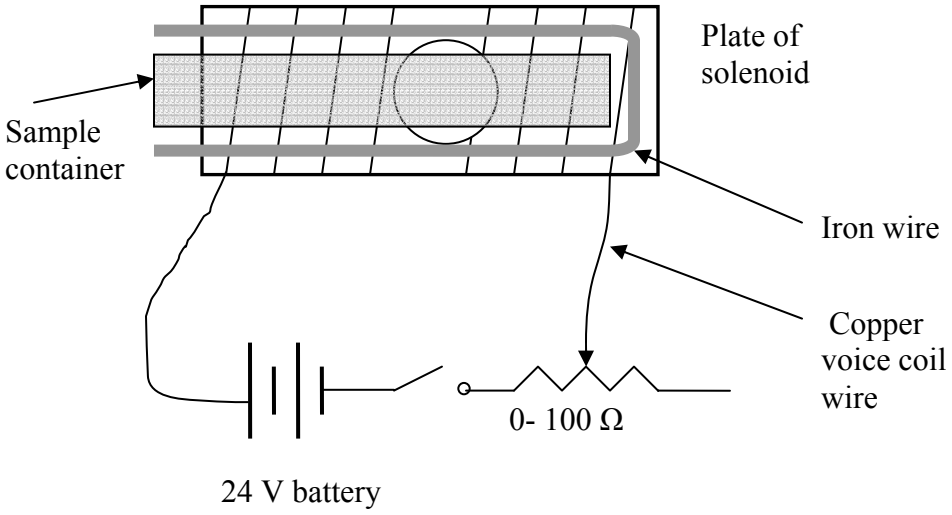

Figure 5.5 Scheme of solenoid with a one dimension magnetic field.

5.2.2.3 Transmission Electron Microscopy (TEM)

JEOL 100 CX TEM was used to visualize the Co-SiO_2 particles. The experiment was performed by Erick Soto-Cantu.

5.3 Results and Discussion

Figure 5.6 is the TEM picture of Co-SiO_2 particles. The darker color core is a Co core, which is 10-15 nm in diameter. Unlike surfactant-coated Co particles,[20;51] our particles have a very thick shell which is about 80-100 nm.

Previous results in Russo's group[57] show SiO_2-coated cobalt particles had magnetic properties similar to those of commercial superparamagnetic Fe_3O_4 latex. After the polypeptide PCBL was coated on the surface, the Co-SiO_2-PCBL particles showed some magnetic hysteresis and dramatically reduced specific magnetization (*M* / mass of sample). Chang *et al.* characterized morphologies of Co-SiO_2 particle assemblies in solution by using an optical

microscope. Five stages were presented for this reversible process of magnetic-field-induced assemble / disarrangement.[20] The idea was adopted for preliminary characterization of our Co-SiO_2 particles and Co-SiO_2-PBLG particles in different solvent. Figure 5.7 is the scheme of the five stages of magnetic field induced assembly.

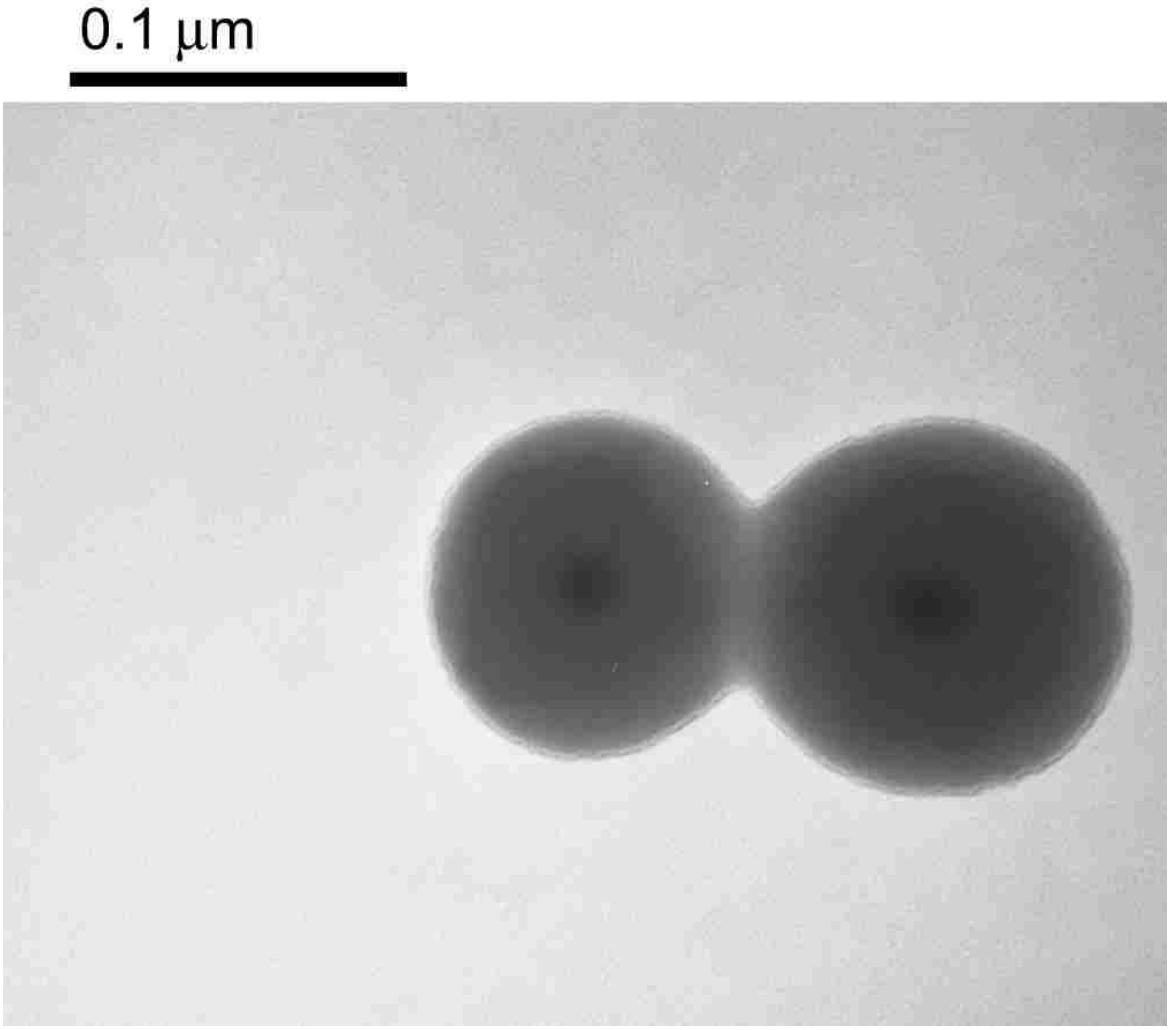

Figure 5.6 TEM picture of Co-SiO_2 particles. (ES3.114A) (TEM picture is provided by Erick Soto-Cantu)

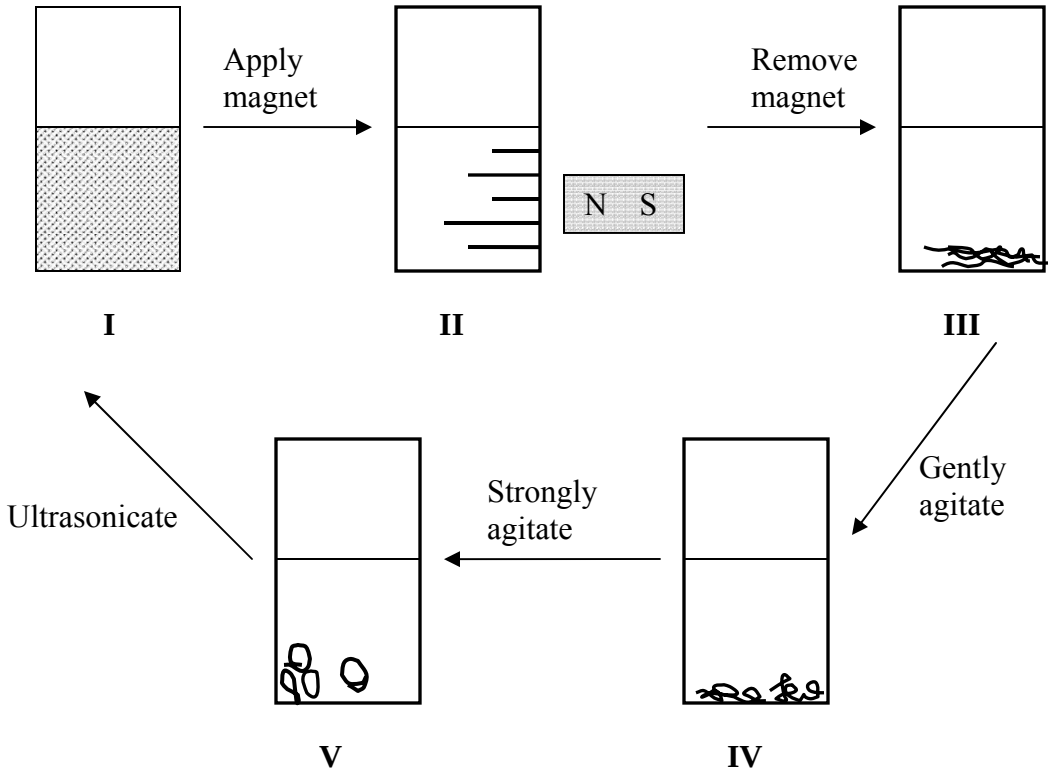

Figure 5.7 Scheme of magnetic field induced assembly (see text).

A magnetic nanoparticle dispersion was ultrasonically agitated and the particles were dispersed in solvent very well as shown in stage I. At stage II, after a bar magnet was applied near the side wall of the vial, nanoparticles formed about centimeter long chains perpendicular to the side wall of the vial. These chains dropped to the bottom of the vial and aggregated together after the magnet was removed (stage III). Mildly agitating the dispersion made these chains form 3D coiled structures (stage IV). These coiled structures were broken down, and micro-sized loop structures were formed after they were vigorously agitated (stage V). The particle suspension went back to stage I from stage V after it was ultrasonicated. Stage I→II→III→ I gives the most information of the assembly and disarrangement of magnetic particles. More accurate examination, such as measuring the hysteresis curve and ZFC/FC experiments, are necessary to

investigate behaviors of magnetic nanoparticles with an applied magnetic field. A superconducting Quantum Interference Device (SQUID) normally takes a solid sample, but for our special case, the behavior of Co-SiO_2-PBLG may change since the polymer shell collapses after the sample is dried. At the same time, for a liquid sample, the signal is too weak and the noise from the solvent background is strong. Our collaborators, in the LSU Physics Department, are still researching about hysteresis of our Co-SiO_2 and Co-SiO_2-PBLG in liquid. Here I will present some results *only* by using a microscope, and these results provide some information about how solvent affects the performance of Co-SiO_2-PBLG by interacting with the polymer shell.

5.3.1 Co-SiO_2 in Ethanol

Figure 5.8 shows Co-SiO_2 particles with a magnet in ethanol (ES3.114A). One can see the particles are easy to be aligned and dispersed again. Three minutes after the magnetic field was applied, there were some short chains formed (figure 5.8). Long, well-aligned chains were formed after 16 minutes, and the distance between two lines is about 10-20 μm (Figure 5.9). Then the sample was shaken by hand and the long chains were broken (Figure 5.10). A few short chains remain, maybe because the hand shaking is not strong enough to break the chains to individual particles. These small-particle blocks contain particles whose magnetic elements are larger than the critical size, so they are not superparamagnetic and they still interact to each other after the magnetic field is cancelled. The magnet was left at the same position as in Figure 5.11 and the sample was observed by using microscopy again two hours later. The picture shows the sample looks almost the same as in Figure 5.11. After ultrasonicated, these magnetic particles were well re-dispersed to solvent (picture is not shown). This visual result shows that there is no or very little hysteresis in these particles. These re-dispersed particles could be re-aligned after a

magnet was reapplied (Figure 5.11). This order-disorder procedure could be repeated many times.

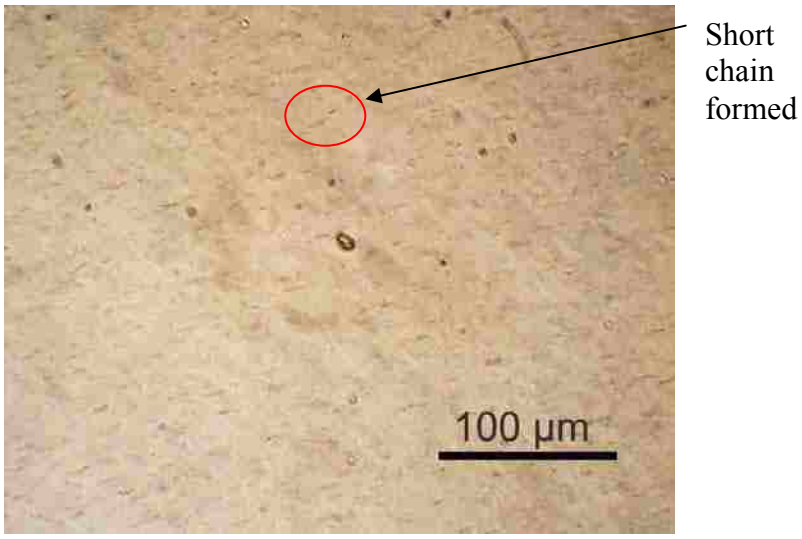

Figure 5.8 Co-SiO_2 in ethanol. Short chains were formed 2-3 minutes after magnetic field applied. (ES.2.105)

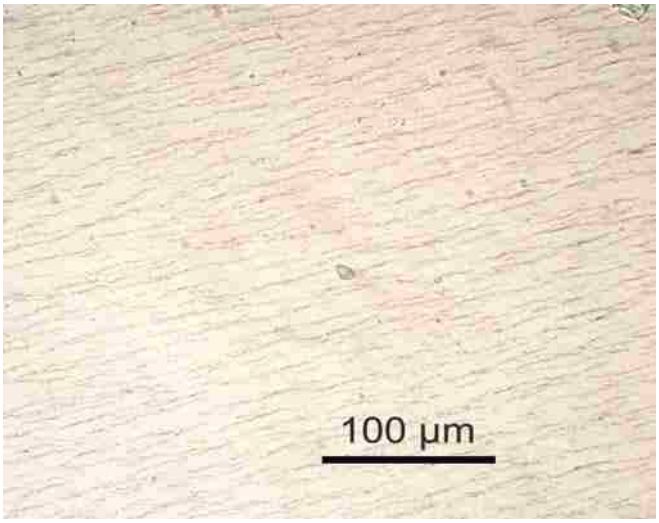

Figure 5.9 Co-SiO_2 in ethanol. Long chains were formed 16 minutes after magnetic field was applied. (same sample as in Figure 5.8)

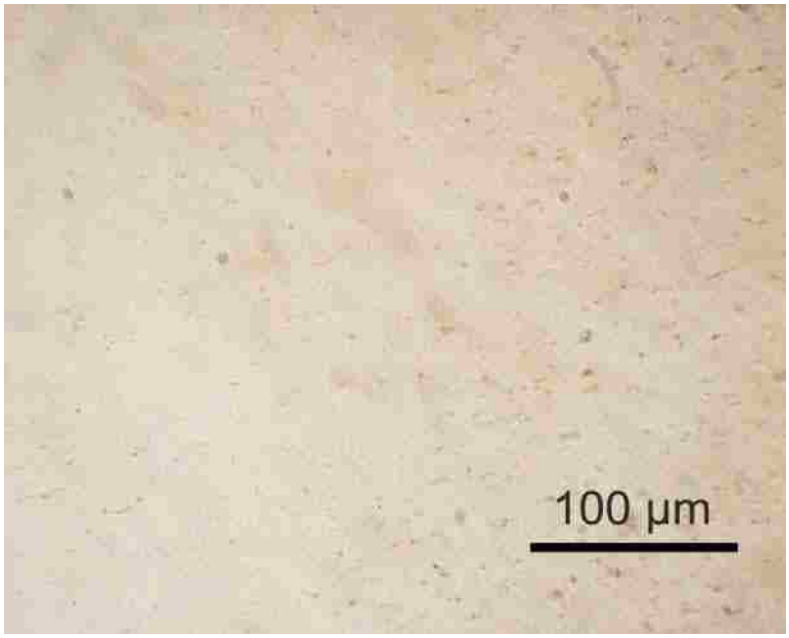

Figure 5.10 Co-SiO_2 in ethanol. After the magnet was removed and the sample was shaken by hand, the long chains were broken. (same sample as in Figure 5.8 and Figure 5.9)

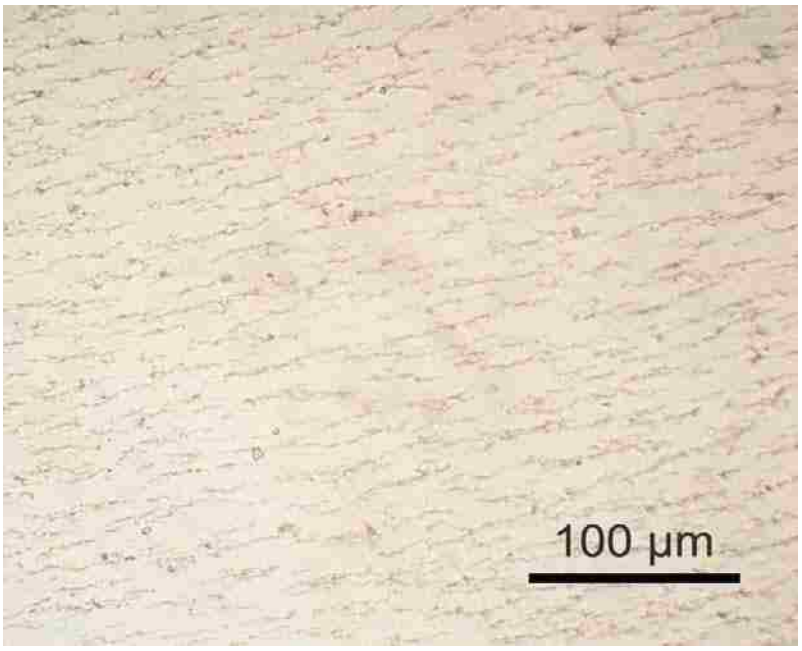

Figure 5.11 Co-SiO_2 in ethanol. Long chains were formed again 16 minutes after the magnet was reapplied. (same sample as in Figure 5.8, Figure 5.9 and Figure 5.10)

5.3.2 Co-SiO_2-PBLG in 1,4-dioxane

After the PBLG chains were grafted onto the surface of the particles, different results were observed. Figure 5.12 shows the alignment of Co-SiO_2-PBLG in 1,4-dioaxne which is a poor solvent for PBLG.

Grafted with PBLG, the particles could still be aligned (Figure 5.12) with an applied magnet and they responded to the rotation of the magnetic field, but the aligned lines were shorter than the ones of Co-SiO_2. Perhaps the PBLG shell reduces the specific magnetization, which also happened for PCBL grafted Co-SiO_2 particles.[57] After several repetitions of applying and removing the magnetic field, the particles tended to aggregate.

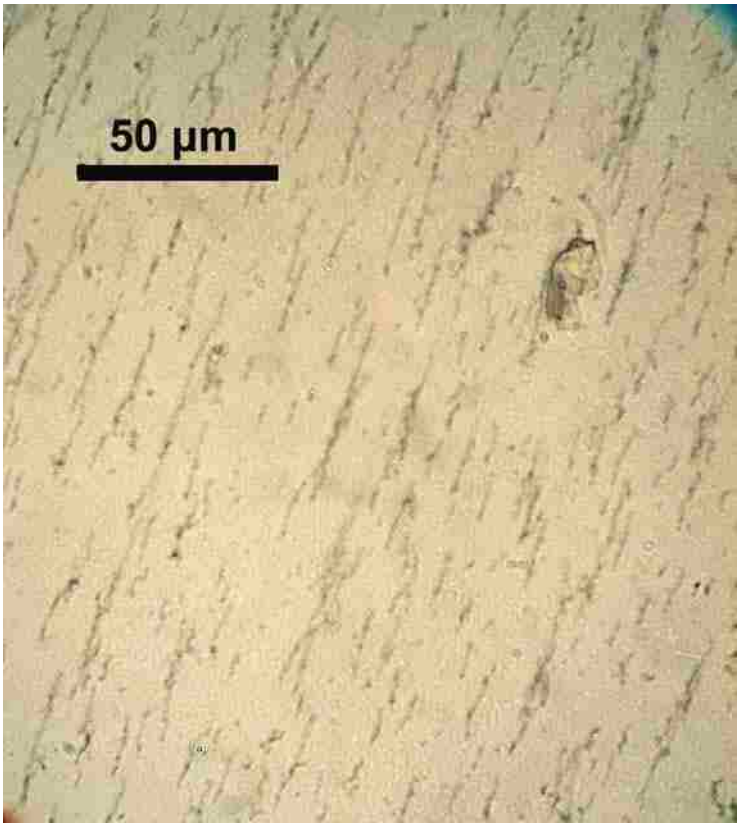

Figure 5.12 Co-SiO_2-PBLG particles in 1,4- dioxane. Chains were formed 20 minutes after magnet was applied. (ES2.113)

5.3.3 Co-SiO_2-PBLG in *m*-cresol

Figure 5.13 and Figure 5.14 are the Co-SiO_2-PBLG in *m*-cresol with a rotated magnetic field. Figure 5.13 is the picture of the alignment in *m*-cresol 1 hour after the magnetic field was applied.

It takes a longer period to align the particles, possibly because of the high viscosity of *m*-cresol at room temperature. On the other hand, one can see the aligned line is even shorter and the aligned lines are much fewer compared with those in dioxane. The chains are fuzzy compared to Figure 5.9. It can be speculated that in good solvent *m*-cresol, the non-aggregated polymer chains "straighten up" from the particle surface, which behaves like thicker shell and consequently reduces magnetization more dramatically. Figure 5.14 shows how the particles have lost their alignment after the magnet was cancelled.

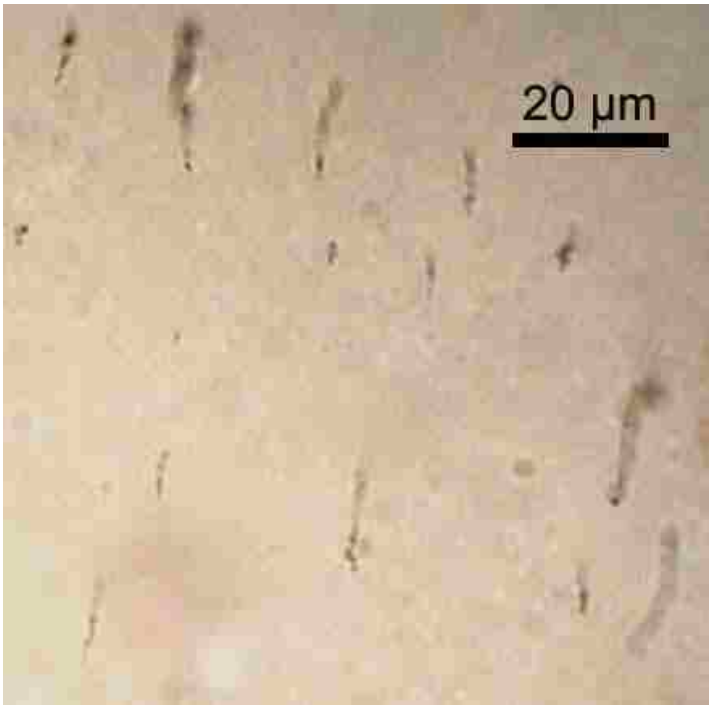

Figure 5.13 Co-SiO_2-PBLG in *m*-cresol. Several short chains were formed one hour after magnet was applied. (ES 2.113)

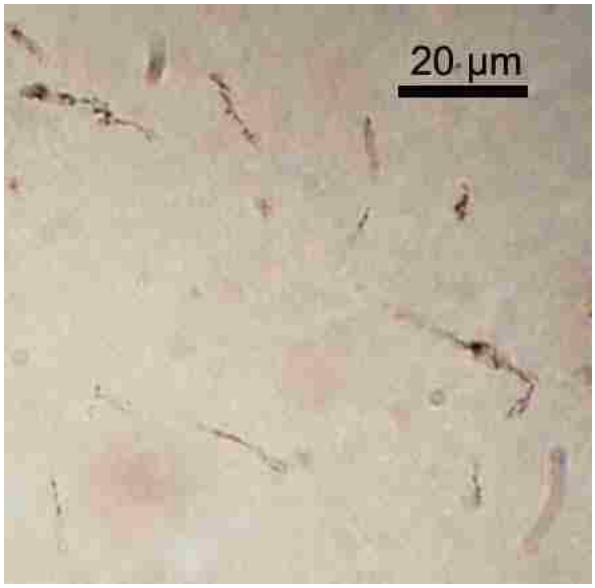

Figure 5.14 Co-SiO_2-PBLG in *m*-cresol. The aligned chains lost the alignment after magnetic field was cancelled. (same sample as in figure 5.13)

5.3.4 Co-SiO_2-PBLG in Pyridine

It is very difficult to see the assembled lines of Co-SiO_2-PBLG particles dispersed in pyridine, which is a good solvent for PBLG polypeptide. Big pieces of aggregates were observed and they were very difficult to be broken down (Figure 5.15).

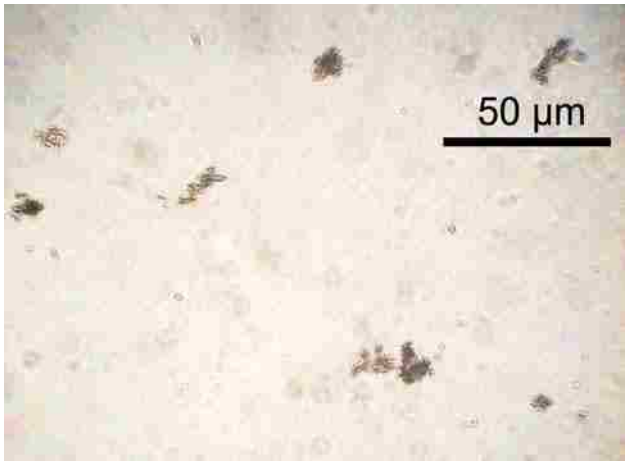

Figure 5.15 Aggregations of Co-SiO_2-PBLG in pyridine. (ES 2.113)

5.3.5 Polymer Shell and Solvent Effects

Comparing to the behavior of these magnetic particles with or without PBLG polymer in different solvents, one can notice first, after the PBLG polymer shell is grafted, the particles are more difficult to be aligned, apparently, the grafted PBLG polymer shell (or the process of placing the shell on the silica core) reduces the particle's magnetization and the same phenomenon was observed for PCBL-grafted Co-SiO_2 particles.[57] It seems that Co-SiO_2-PBLG particles do not behave as superparamagnets any more after the magnetic field is removed, the particles can't move freely and particles tend to aggregate after several repetitions of applying and removing the magnetic field. This is may be because polymer brushes (from different particles) entwine and there are more inter-twists with more repetitions. The reduction of magnetization after polymer addition remains mysterious, because the SiO_2 is very thick (about 80-100 nm) and the microscope observations showed that the Co-SiO_2 sample behaved almost the same long period of time after it was prepared.

The way that solvent affects these particles mainly comes from the effect on grafted polymer. In the good solvent pyridine, the polymer chains should be extended and form rigid rods. The particles move together after the particles' response to the magnetic field. As long as the particles meet each other, they enmesh, and the particles can't adjust their positions to align themselves. For a poor solvent like 1,4-dioxane, the polymer chains collapse on the surface and a solid-like polymer shell is formed. The shell decreases the magnetic property of the Co-SiO_2, but helps these particles stay separated, so the particles still can get parallel aligned lines and the lines are just shorter than the one that Co-SiO_2 particles form. Pyridine and *m*- cresol both are good solvents for PBLG, but *m*-cresol (17.296 cp, 20 °C) has a much higher viscosity than pyridine (0.954 cp, 20 °C), and this is also can be described by saying that Co-SiO_2-PBLG

particles "diffuse" in *m*-cresol much slower than in pyridine. So, after a magnetic field is applied, the particles in *m*-cresol have some time to be arranged before they get together.

As mentioned before, all of these are preliminary results. More quantitative data e.g., the hysteresis loop, the ZFC/FC curve, are needed to be investigated and explained about what really happens between these particles.

In order to verify the effect of a polypeptide shell, the best way is 1) compare the magnetic properties of Co-SiO_2 particles with Co-SiO_2-polypeptpide particles; 2) remove the polypeptide shells; 3) compare the particles (the shells have been removed) with Co-SiO_2 particles. If the particles (after the polypeptide shells are removed) behave *not* the same as the Co-SiO_2 particles, one has to do further investigation whether the change of magnetic properties is from aging of the particles or other factors.

5.4 Conclusions

SiPCPs with nano-sized (in this case it is 10-15 nm) cobalt core gives magnetic properties to these particles. Based on microscope observations, Co-SiO_2 particles in ethanol are easily aligned with the external magnetic field and can be dispersed again after the magnetic field is removed and subsequently ultrasonicated. The particles present a different magnetic behavior after the polypeptides are grafted and then are dispersed in different solvents. The Co-SiO_2-PBLG particles still can be aligned with a magnetic field in poor solvent of PBLG (1,4- dioxane), but the aligned lines are shorter than the ones of those lined formed by Co-SiO_2 particles. In the good but very viscous solvent *m*-cresol, it is more difficult to align these particles, and the aligned lines are even shorter. These particles always form a large aggregation before they get aligned in the good solvent pyridine. It seems possible that the solvent affects the polypeptide shell and consequently changes the magnetic behavior of the Co-SiO_2-PBLG particles, but a

detail study in which polypeptide-coated and bare core particles are aged under identical condition has yet to be completeted.

5.5 Future Work

More magnetic property measurements such as hysteresis loop and FC/ZFC experiments are needed to provide more details. In addition, since the polypeptide shell is one of the most important factors, the effect of the shell thickness, the surface density, the polypeptide conformation and the different types of polypeptide shell can all be interesting topics and are worth being studied further.

5.6 References

1) Keffer,F. In Anonymous1966; *Ch.* 2. Handbuch der Physik

2) Heller,P. Experimental investigations of critical phenomena. *Reports on Progress in Physics* **1967**, *30*, 731-826.

3) Fernandez-Pacheco,R.; Marquina,C.; Gabriel Valdivia,J.; Gutierrez,M.; Soledad Romero,M.; Cornudella,R.; Laborda,A.; Viloria,A.; Higuera,T.; Garcia,A.; Garcia de Jalon,J.A.; Ricardo Ibarra,M. Magnetic nanoparticles for local drug delivery using magnetic implants. *Journal of Magnetism and Magnetic Materials* **2007**, *311*, 318-322.

4) Primo,F.L.; Michieleto,L.; Rodrigues,M.A.M.; Macaroff,P.P.; Morais,P.C.; Lacava,Z.G.M.; Bentley,M.V.; Tedesco,A.C. Magnetic nanoemulsions as drug delivery system for Foscan: Skin permeation and retention in vitro assays for topical application in photodynamic therapy (PDT) of skin cancer. *Journal of Magnetism and Magnetic Materials* **2007**, *311*, 354-357.

5) Zhang,J.L.; Srivastava,R.S.; Misra,R.D.K. Core-shell magnetite nanoparticles surface encapsulated with smart stimuli-responsive polymer: synthesis, characterization, and LCST of viable drug-targeting delivery system. *Langmuir* **2007**, *23*, 6342-6351.

6) Ibarra,M.R.; Fernandez-Pacheco,R.; Valdivia,J.G.; Marquina,C.; Gutierrez,M. Magnetic nanoparticle complexes for drug delivery, and implanted magnets for targeting. *AIP Conference Proceedings* **2007**, *898*, 99-105.

7) Sun,S. Self-assembled FePt nanoparticle arrays as potential high-density recording media. *Springer Series in Materials Science* **2007**, *94*, 15-28.

8) Reiss,G.; Huetten,A. Magnetic nanoparticles: Applications beyond data storage. *Nature Materials* **2005**, *4*, 725-726.

9) Calderon-Ortiz,E.; Perales-Peres,O.; Gutierres,G.; Rinaldi,C. Size-control and size-selection of CoFe2O4 and MnxZn1-xFe2O4 ferrite nanoparticles for data storage and magnetocaloric applications. *Abstracts of Papers, 229th ACS National Meeting, San Diego, CA, United States, March 13-17, 2005* **2005**, IEC-033

10) Yu,A.C.C.; Mizuno,M.; Sasaki,Y.; Kondo,H. Atomic composition effect on the ordering of solution-phase synthesized FePt nanoparticle films. *Applied Physics Letters* **2004**, *85*, 6242-6244.

11) Bae,S.; Lee,S.W.; Takemura,Y. Applications of NiFe2O4 nanoparticles for a hyperthermia agent in biomedicine. *Applied Physics Letters* **2006**, *89*, 252503-1-252503/3.

12) Lecommandoux,S.; Sandre,O.; Checot,F.; Perzynski,R. Smart hybrid magnetic self-assembled micelles and hollow capsules. *Progress in Solid State Chemistry* **2006**, *34*, 171-179.

13) Gan,Z.; Jiang,J. Preparation of magnetic monodisperse nanoparticles and biopolymer assembly on magnetic carriers. *Huaxue Jinzhan* **2005**, *17*, 978-986.

14) Berret,J.F.; Cartier,R. Use of superparamagnetic nanoparticle/block copolymer electrostatic complexes as contrast agents in Magnetic Resonance Imaging. *Los Alamos National Laboratory, Preprint Archive, Condensed Matter* **2007**, 1-4, arXiv.

15) Taboada,E.; Rodriguez,E.; Roig,A.; Oro,J.; Roch,A.; Muller,R.N. Relaxometric and magnetic characterization of ultrasmall iron oxide nanoparticles with high magnetization. evaluation as potential t1 magnetic resonance imaging contrast agents for molecular imaging. *Langmuir* **2007**, *23*, 4583-4588.

16) Hiraga,K.; Ishikawa,K. Low temperature magnetic properties of austenitic iron-based alloys containing g' particles. *Nippon Kinzoku Gakkaishi* **1987**, *51*, 479-487.

17) Pankina,G.V.; Chernavskii,P.A.; Khodakov,A.Y.; Girardon,G.S.; Lunin,V.V. The influence of Ru and Re admixtures on the size of Co particles in Co/SiO_2 catalysts of the Fischer-Tropsch synthesis. *Russian Journal of Physical Chemistry* **2006**, *80*, 732-737.

18) Gill,C.S.; Jones,C.W. Recoverable acid functionalized, silica coated superparamagnetic nanoparticle catalysts for the polymerization of e-caprolactone. *Polymer Preprints (American Chemical Society, Division of Polymer Chemistry)* **2006**, *47*, 246

19) Batlle,X.; Labarta,A. Finite-size effects in fine particles. Magnetic and transport properties. *Journal of Physics D: Applied Physics* **2002**, *35*, R15-R42

20) Cheng,G.; Romero,D.; Fraser,G.T.; Walker,A.R.H. Magnetic-field-induced assemblies of cobalt nanoparticles. *Langmuir* **2005**, 21, 12055-12059

21) Gross,A.F.; Diehl,M.R.; Beverly,K.C.; Richman,E.K.; Tolbert,S.H. Controlling magnetic coupling between cobalt nanoparticles through nanoscale confinement in hexagonal mesoporous silica. *Journal of Physical Chemistry B* **2003**, *107*, 5475-5482.

22) Wan,J.; Tang,G.; Qian,Y. Room temperature synthesis of single-crystal Fe3O4 nanoparticles with superparamagnetic property. *Applied Physics A: Materials Science & Processing* **2007**, *86*, 261-264.

23) Liu,X.; Guan,Y.; Ma,Z.; Liu,H. Surface modification and characterization of magnetic polymer nanospheres prepared by miniemulsion polymerization. *Langmuir* **2004**, *20*, 10278-10282.

24) Sahoo,Y.; Pizem,H.; Fried,T.; Golodnitsky,D.; Burstein,L.; Sukenik,C.N.; Markovich,G. Alkyl phosphonate/phosphate coating on magnetite nanoparticles: a comparison with fatty acids. *Langmuir* **2001**, *17*, 7907-7911.

25) Kim,M.; Chen,Y.; Liu,Y.; Peng,X. Super-stable, high-quality Fe3O4 dendron-nanocrystals dispersible in both organic and aqueous solutions. *Advanced Materials (Weinheim, Germany)* **2005**, *17*, 1429-1432.

26) Lu,A.H.; Li,W.C.; Matoussevitch,N.; Spliethoff,B.; Boennemann,H.; Schueth,F. Highly stable carbon-protected cobalt nanoparticles and graphite shells. *Chemical Communications (Cambridge, United Kingdom)* **2005**, 98-100.

27) Kobayashi,Y.; Horie,M.; Konno,M.; Rodriguez-Gonzalez,B.; Liz-Marzan,L.M. Preparation and properties of silica-coated cobalt nanoparticles. *Journal of Physical Chemistry B* **2003**, *107*, 7420-7425.

28) Cho,S.J.; Idrobo,J.C.; Olamit,J.; Liu,K.; Browning,N.D.; Kauzlarich,S.M. Growth mechanisms and oxidation resistance of gold-coated iron nanoparticles. *Chemistry of Materials* **2005**, *17*, 3181-3186.

29) Wang,L.; Luo,J.; Maye,M.M.; Fan,Q.; Rendeng,Q.; Engelhard,M.H.; Wang,C.; Lin,Y.; Zhong,C.J. Iron oxide-gold core-shell nanoparticles and thin film assembly. *Journal of Materials Chemistry* **2005**, *15*, 1821-1832.

30) Caruntu,D.; Cushing,B.L.; Caruntu,G.; O'Connor,C.J. Attachment of Gold Nanograins onto Colloidal Magnetite Nanocrystals. *Chemistry of Materials* **2005**, *17*, 3398-3402.

31) Park,J.I.; Cheon,J. Synthesis of solid solution and core-shell type cobalt-platinum magnetic nanoparticles via transmetalation reactions. *Journal of the American Chemical Society* **2001**, *123*, 5743-5746.

32) Wan,M.; Li,J. Synthesis and electrical-magnetic properties of polyaniline composites. *Journal of Polymer Science, Part A: Polymer Chemistry* **1998**, *36*, 2799-2805.

33) Butterworth,M.D.; Bell,S.A.; Armes,S.P.; Simpson,A.W. Synthesis and characterization of polypyrrole-magnetite-silica particles. *Journal of Colloid and Interface Science* **1996**, *183*, 91-99.

34) Barratt,G. Colloidal drug carriers: Achievements and perspectives. *Cellular and Molecular Life Sciences* **2003**, *60*, 21-37.

35) Dresco,P.A.; Zaitsev,V.S.; Gambino,R.J.; Chu,B. Preparation and properties of magnetite and polymer magnetite nanoparticles. *Langmuir* **1999**, *15*, 1945-1951.

36) Mendenhall,G.D.; Geng,Y.; Hwang,J. Optimization of long-term stability of magnetic fluids from magnetite and synthetic polyelectrolytes. *Journal of Colloid and Interface Science* **1996**, *184*, 519-526.

37) Harris,L.A.; Goff,J.D.; Carmichael,A.Y.; Riffle,J.S.; Harburn,J.J.; St.Pierre,T.G.; Saunders,M. Magnetite nanoparticle dispersions stabilized with triblock copolymers. *Chemistry of Materials* **2003**, *15*, 1367-1377.

38) Boyen,H.G.; Kastle,G.; Zurn,K.; Herzog,T.; Weigl,F.; Ziemann,P.; Mayer,O.; Jerome,C.; Moller,M.; Spatz,J.P.; Garnier,M.G.; Oelhafen,P. A micellar route to ordered arrays of magnetic nanoparticles. From size-selected pure cobalt dots to cobalt-cobalt oxide core-shell systems. *Advanced Functional Materials* **2003**, *13*, 359-364.

39) Peng,D.L.; Sumiyama,K.; Hihara,T.; Yamamuro,S.; Konno,T.J. Magnetic properties of monodispersed Co/CoO clusters. *Physical Review B: Condensed Matter and Materials Physics* **2000**, *61*, 3103-3109.

40) Ohmori,M.; Matijevic,E. Preparation and properties of uniform coated colloidal particles. VII. Silica on hematite. *Journal of Colloid and Interface Science* **1992**, *150*, 594-598.

41) Correa-Duarte,M.A.; Giersig,M.; Kotov,N.A.; Liz-Marzan,L.M. Control of packing order of self-assembled monolayers of magnetite nanoparticles with and without sio2 coating by microwave irradiation. *Langmuir* **1998**, *14*, 6430-6435.

42) Yi,D.K.; Lee,S.S.; Papaefthymiou,G.C.; Ying,J.Y. Nanoparticle Architectures Templated By Sio2/Fe2O3 Nanocomposites. *Chemistry of Materials* **2006**, *18*, 614-619.

43) Ohmori,M.; Matijevic,E. Preparation and properties of uniform coated inorganic colloidal particles. 8. Silica on iron. *Journal of Colloid and Interface Science* **1993**, *160*, 288-292.

44) Lu,Y.; Yin,Y.; Mayers,B.T.; Xia,Y. Modifying the surface properties of superparamagnetic iron oxide nanoparticles through a sol-gel approach. *Nano Letters* **2002**, *2*, 183-186.

45) Tago,T.; Hatsuta,T.; Miyajima,K.; Kishida,M.; Tashiro,S.; Wakabayashi,K. Novel synthesis of silica-coated ferrite nanoparticles prepared using water-in-oil microemulsion. *Journal of the American Ceramic Society* **2002**, *85*, 2188-2194.

46) Graf,C.; Vossen,D.L.J.; Imhof,A.; van Blaaderen,A. A general method to coat colloidal particles with silica. *Langmuir* **2003**, *19*, 6693-6700.

47) Philipse,A.P.; van Bruggen,M.P.B.; Pathmamanoharan,C. Magnetic silica dispersions: preparation and stability of surface-modified silica particles with a magnetic core. *Langmuir* **1994**, *10*, 92-99.

48) Liz-Marzan,L.M.; Giersig,M.; Mulvaney,P. Synthesis of nanosized gold-silica core-shell particles. *Langmuir* **1996**, *12*, 4329-4335.

49) Ung,T.; Liz-Marzan,L.M.; Mulvaney,P. Controlled method for silica coating of silver colloids. influence of coating on the rate of chemical reactions. *langmuir* **1998**, *14*, 3740-3748.

50) Hyeon,T. Chemical synthesis of magnetic nanoparticles. *Chemical Communications (Cambridge, United Kingdom)* **2003**, 927-934.

51) Lu,A.H.; Salabas,E.L.; Schueth,F. Magnetic nanoparticles: synthesis, protection, functionalization, and application. *Angewandte Chemie, International Edition* **2007**, *46*, 1222-1244.

52) Dinega,D.P.; Bawendi,M.G. A solution-phase chemical approach to a new crystal structure of cobalt. *Angewandte Chemie, International Edition* **1999**, *38*, 1788-1791.

53) Park,J.; Lee,E.; Hwang,N.M.; Kang,M.; Kim,S.C.; Hwang,Y.; Park,J.G.; Noh,H.J.; Kim,J.Y.; Park,J.H.; Hyeon,T. One-nanometer-scale size-controlled synthesis of monodisperse magnetic Iron oxide nanoparticles. *Angewandte Chemie, International Edition* **2005**, *44*, 2872-2877.

54) Park,J.; An,K.; Hwang,Y.; Park,J.G.; Noh,H.J.; Kim,J.Y.; Park,J.H.; Hwang,N.M.; Hyeon,T. Ultra-large-scale syntheses of monodisperse nanocrystals. *Nature Materials* **2004**, *3*, 891-895.

55) Murray,C.B.; Sun,S.; Doyle,H.; Betley,T. Monodisperse 3d transition-metal (Co, Ni, Fe) nanoparticles and their assembly into nanoparticle superlattices. *MRS Bulletin* **2001**, *26*, 985-991.

56) Lin,X.M.; Samia,A.C.S. Synthesis, assembly and physical properties of magnetic nanoparticles. *Journal of Magnetism and Magnetic Materials* **2006**, *305*, 100-109.

57) Sibel Turksen. Synthesis and characterization of superparamagnetic silica-homopolypeptide composite particles. Ph.D Dissertation, LSU, 2005.

APPENDIX: PERMISSION LETTERS

07/05/2007 15:51 FAX 2027768112 LSU CHEMISTRY 001

ACS PUBLICATIONS DIVISION PAGE 02/02

JUL - 5 2007

COPYRIGHT OFFICE

PERMISSION REQUEST FORM

Date: 07/05/07

FROM:

For: Copyright Office
Publications Division
American Chemical Society
1155 Sixteenth Street, N.W.
Washington, DC 20036

FAX: 202-776-8112

TO:

From: Jianhong Qiu
Chemistry Department, LSU
Baton Rouge, LA, 70820

Your Phone No. 225-5783355
Your Fax No 225-5783458

I am preparing a paper entitled:

to appear in a **(circle one)** book, magazine, journal, proceedings, other Dissertation
entitled: Properties of Silica-Polypeptide Composite Particles

to be published by: Louisiana State University

I would appreciate your permission to use the following ACS material in print and other formats with the understanding that the required ACS copyright credit line will appear with each item and that this permission is for only the requested work listed above:

From ACS journals or magazines (for ACS magazines, also include issue no.):
ACS Publication Title Issue Date Vol. No. Page(s) Material to be used*

1) Langmuir, "Depletion-Induced Crystallization in Colloidal Rod-Sphere Mixtures" Year 1999, Vol., 15, No.,14, page 4694, figure1

2) Journal of Physical Chemistry B, "Controlling Magnetic Coupling between Cobalt Nanoparticles through Nanoscale Confinement in Hexagonal Mesoporous Silica." Year 2003, Vol., 107, No., 23 page 5479, figure 5

From ACS books: include ACS book title, ~~series name and number, year, page(s) book~~ editor=s name(s), chapter author's name(s), etc.*

PERMISSION TO REPRINT IS GRANTED BY THE AMERICAN CHEMICAL SOCIETY

ACS CREDIT LINE REQUIRED. Please follow this sample: Reprinted with permission from (reference citation). Copyright (year) American Chemical Society.

APPROVED BY: C. Arleen Courtney 7-5-07
ACS Copyright Office

☐ If box is checked, author permission is also required. See original article for address.

* If you use more than three figures/tables f will also be required.

Questions? Please call Arleen Courtney at (202) 872-4368 or use the FAX number above.

This space is reserved for ACS Copyright Office Use

NATURE PUBLISHING GROUP LICENSE
TERMS AND CONDITIONS

Jul 05, 2007

This is a License Agreement between Jianhong Qiu ("You") and Nature Publishing Group ("Nature Publishing Group"). The license consists of your order details, the terms and conditions provided by Nature Publishing Group, and the payment terms and conditions.

License Number	1742661073019
License date	Jul 05, 2007
Licensed content publisher	Nature Publishing Group
Licensed content publication	Nature
Licensed content title	Entropically driven microphase transitions in mixtures of colloidal rods and spheres
Licensed content author	Marie Adams , Zvonimir Dogic , Sarah L. Keller and Seth Fraden
Volume number	
Issue number	
Pages	
Year of publication	1998
Portion used	Figures
Number of figures	1
Requestor type	Student
Type of Use	Thesis / Dissertation
PO Number	
Total	$0.00
Terms and Conditions	

Terms and Conditions for Permissions

Nature Publishing Group hereby grants you a non-exclusive license to reproduce this material for this purpose, and for no other use, subject to the conditions below:

1. NPG warrants that it has, to the best of its knowledge, the rights to license reuse of this material. However, you should ensure that the material you are requesting is original to Nature Publishing Group and does not carry the copyright of another entity (as credited in the published version). If the credit line on any part of the material you have requested indicates that it was reprinted or adapted by NPG with permission from another source, then you should also seek permission from that source to reuse the material.

2. Permission granted free of charge for material in print is also usually granted for any electronic version of that work, provided that the material is incidental to the work as a whole and that the electronic version is essentially equivalent to, or substitutes for, the print version. Where print permission has been granted for a fee, separate

VITA

Jianhong Qiu, a native of the Peoples Republic of China, received her Bachelor of Engineering degree from department of Applied Chemistry, Tianjing University. Jianhong then started working as research assistant before she came to United States for her graduate school. In the United States, she earned the Master of Science degree in chemistry from Louisiana Tech University and currently she is a candidate for the degree of Doctor of Philosophy at Louisiana State University.